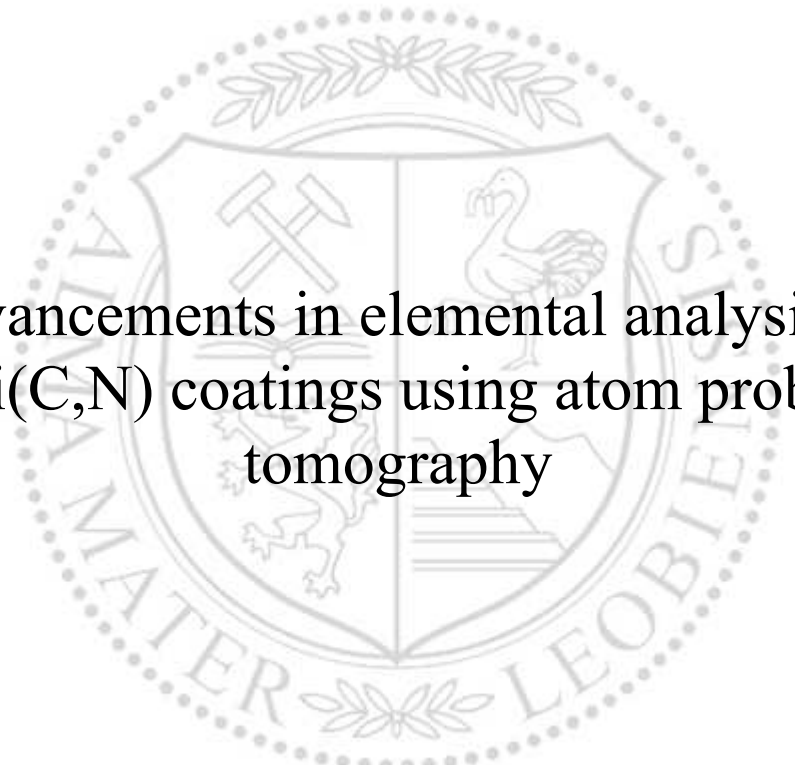




Chair of Functional Materials and Materials Systems

Master's Thesis



Advancements in elemental analysis of
Ti(C,N) coatings using atom probe
tomography

Maximilian Schiester, BSc

April 2024



EIDESSTÄTLICHE ERKLÄRUNG

Ich erkläre an Eides statt, dass ich diese Arbeit selbstständig verfasst, andere als die angegebenen Quellen und Hilfsmittel nicht benutzt, den Einsatz von generativen Methoden und Modellen der künstlichen Intelligenz vollständig und wahrheitsgetreu ausgewiesen habe, und mich auch sonst keiner unerlaubten Hilfsmittel bedient habe.

Ich erkläre, dass ich den Satzungsteil „Gute wissenschaftliche Praxis“ der Montanuniversität Leoben gelesen, verstanden und befolgt habe.

Weiters erkläre ich, dass die elektronische und gedruckte Version der eingereichten wissenschaftlichen Abschlussarbeit formal und inhaltlich identisch sind.

Datum 04.04.2024

Unterschrift Verfasser/in
Maximilian Schiester

The financial support by the Austrian Federal Ministry for Digital and Economic Affairs and the National Foundation for Research, Technology and Development and the Christian Doppler Research Association is gratefully acknowledged.

„Atoms, ja, atoms!“

Erwin W. Müller on October 11th, 1955.

The first person to ever observe individual atoms.

Acknowledgements

I am deeply grateful to Prof. Dr. Christian Mitterer, Head of the Department Materials Science, for giving me the opportunity to conduct this work at this department.

Very special thanks go to my supervisor Priv.-Doz. Dr. Nina Schalk, Head of the Christian Doppler Laboratory for Advanced Coated Cutting Tools. *Thank you, Nina, for your superb support and guidance on my academic journey since day one, I look forward to every further one.*

I could not have undertaken this journey without Dr. Michael Tkadletz, who is not only the best mentor one could imagine but also a really good friend. *Thank you, Mike, your passion and encouragement have had a decisive influence on my academic development and have made this work a great pleasure. I am excited what comes next.*

Special acknowledgement to Dr.-Ing. Marcus Hans, Group Leader Atom Probe Tomography at the Chair of Materials Chemistry at RWTH Aachen University, Germany, for his collaboration, brainstorming sessions and shared insights, which greatly enriched the research experience.

I want to express my gratitude to Dr. Katherine P. Rice, Applications Manager at CAMECA Instruments in Madison, United States, for her warm support, motivation and shared fascination for atom probe tomography.

Many thanks also to all my colleagues from the Chair of Functional Materials and Materials Systems. I especially want to emphasize Magdalena Kirchmair, BSc, Dr. Helene Waldl, Dr. Fabian Konstantiniuk, DI Daniel Rainer, DI Lukas Kölbl and Dr. Christian Saringer, who played a very special role for me during my studies. *Thank you all for your support and all the fun.*

I extend my heartfelt gratitude to Wolfgang Archer, BSc and Paul Uschan, BSc for being a constant source of encouragement, understanding and team spirit. *Your friendship has truly enriched my life.*

My sincere thanks to my whole family and all my friends who remain unnamed here for their heartfelt support and encouragement.

I want to express my deepest gratitude to my parents Karin and Manfred for their enduring support, guidance, belief in my abilities and the countless love since the beginning of my life. *I am proud of you!*

To my parents-in-law, Elisabeth and Heimo, I am grateful for the warmth and the support you have provided me during the last years. *Thank you!*

Last but not least, this thesis is a testament to the unwavering support and endless love of my wife, Julia. *Your sacrifices, encouragement and belief in my dreams have been the driving force that propelled me to reach this academic milestone. I am forever grateful, this achievement is as much yours as it is mine. I love you!*

Abstract

Atom probe tomography (APT) has emerged as a crucial tool in materials science, offering near-atomic resolution and enabling to investigate the three-dimensional distribution of elements. However, the accuracy of elemental composition observed via APT is significantly influenced by acquisition parameters, in particular the effective electric field and laser pulse energy (LPE). Within this study, the impact of these parameters on compositional biases is systematically investigated using a series of Ti(C,N) coatings, ranging from TiN to TiC. Advanced acquisition parameters, available in modern atom probes were utilized, revealing improved evaporation conditions and a higher specimen survival rate. For this purpose, measurements were carried out with active constant field control, auto pulse rate control and auto pulse energy control. The subsequent comparison with the results obtained with the conventional standard parameters made it possible to analyze the advantages of the advanced acquisition parameters. Customized software scripts were developed to enhance data analysis, including peak decomposition for accurate elemental composition determination.

The investigation illuminated various compositional biases dependent on the C/(C+N) ratio and LPE. At low LPEs, preferential retention of carbon and nitrogen was observed. Carbides exhibited tendencies to evaporate as adjacent groups or large molecules, with dissociation effects becoming pronounced at very high LPEs. These findings highlight the significance of optimized electric field strength for achieving a high elemental accuracy.

In conclusion, this work provides comprehensive insights into the evaporation behavior of nitrides and carbides in atom probe tomography, facilitating improved elemental analysis for future investigations. Utilization of advanced acquisition parameters is recommended for enhanced measurement efficiency and accuracy. By understanding and controlling acquisition parameters, researchers can mitigate compositional biases and advance the capabilities of atom probe tomography in materials science research.

Kurzfassung

Die Atomsondentomographie (APT) hat sich zu einem wichtigen Instrument in der Materialwissenschaft entwickelt, welches eine nahezu atomare Auflösung bietet und die Untersuchung der dreidimensionalen Verteilung von Elementen ermöglicht. Die Genauigkeit der mittels APT beobachteten Elementzusammensetzung wird jedoch erheblich von den Messparametern beeinflusst, insbesondere vom effektiven elektrischen Feld und der Laserpulsenergie (LPE). In dieser Studie werden die Auswirkungen dieser Parameter auf die Abweichungen in der Zusammensetzung anhand einer Reihe von Ti(C,N) Schichten, die von TiN bis TiC reichen, systematisch untersucht. Es wurden erweiterte Messparameter verwendet, die in modernen Atomsonden zur Verfügung stehen, was zu verbesserten Evaporationsbedingungen und einer höheren Überlebensrate der Proben führte. Zu diesem Zweck wurden die Messungen mit aktiver konstanter Feldsteuerung, automatischer Pulsratensteuerung und automatischer Pulsenergiesteuerung durchgeführt. Der anschließende Vergleich mit den Ergebnissen, die mit den herkömmlichen Standardparametern erzielt wurden, ermöglichte es, die Vorteile der erweiterten Messparameter zu analysieren. Zur Verbesserung der Datenanalyse wurden maßgeschneiderte Softwareskripts entwickelt, einschließlich der Zerlegung von Spektralpeaks zur genauen Bestimmung der Elementzusammensetzung.

Die Untersuchungen zeigten verschiedene Ursachen für Abweichungen in der Zusammensetzung, die vom C/(C+N)-Verhältnis und dem LPE abhängen. Bei niedrigen LPEs wurde eine bevorzugte Zurückhaltung von Kohlenstoff und Stickstoff beobachtet. Karbide zeigten die Tendenz, als benachbarte Gruppen oder große Moleküle zu evaporieren, wobei Dissoziationseffekte bei sehr hohen LPEs ausgeprägt waren. Diese Ergebnisse unterstreichen die Bedeutung einer optimierten elektrischen Feldstärke, um eine hohe Genauigkeit der bestimmten Elementzusammensetzung zu erreichen.

Zusammenfassend, liefert diese Arbeit umfassende Einblicke in das Evaporationsverhalten von Nitriden sowie Karbiden in der Atomsondentomographie und ermöglicht eine verbesserte Elementanalyse für zukünftige Untersuchungen. Die Verwendung erweiterter Messparameter wird empfohlen, um die Effizienz und Genauigkeit der Messungen zu verbessern. Durch das Verständnis und die Kontrolle der Erfassungsparameter können Abweichungen in der Zusammensetzung verringert und die Möglichkeiten der Atomsondentomographie in der materialwissenschaftlichen Forschung verbessert werden.

Contents

Abstract	V
Kurzfassung.....	VI
List of abbreviations	VIII
1. Introduction.....	1
2. Theoretical background	3
2.1. Atom probe tomography.....	3
2.2. From electric field strength to field evaporation	5
2.3. Post-ionization of field-evaporated ions	9
2.4. Ranging and peak decomposition	10
2.5. Ion pile-up phenomenon	17
2.6. Dissociation processes	19
2.7. Standard acquisition parameters.....	21
2.8. Advanced acquisition parameters.....	23
3. Methodology.....	28
3.1. Investigated materials	28
3.2. Determination of the reference elemental composition.....	29
3.3. Specimen preparation	30
3.4. Atom probe tomography measurements.....	33
3.5. Atom probe tomography data post-processing	35
4. Results and discussion	39
4.1. TiN.....	39
4.2. TiC _{0.25} N _{0.75}	46
4.3. TiC _{0.45} N _{0.55}	48
4.4. TiC _{0.61} N _{0.39}	51

4.5.	TiC _{0.78} N _{0.22}	55
4.6.	TiC	58
4.7.	Trends within the Ti(C,N) coating system	61
5.	Conclusions	67
6.	References	69
7.	Appendix.....	76

List of abbreviations

AAP	Advanced acquisition parameter
AER	Areal evaporation rate
APT	Atom probe tomography
CSR	Charge state ratio
CVD	Chemical vapor deposition
DR	Detection rate
ERDA	Elastic recoil detection analysis
LEAP	Local electrode atom probe
LPE	Laser pulse energy
m/n	Mass-to-charge-state
MRP	Mass resolving power ($m/\Delta m$)
PR	Pulse rate
RBS	Rutherford backscattering spectrometry
ROI	Region of interest
ToF	Time of flight
ZBEF	Zero barrier evaporation field

1. Introduction

Atom probe tomography (APT) has become an integral part of materials science in recent years. With almost atomic resolution, it provides a three-dimensional elemental reconstruction of the investigated specimen. In combination with the elemental information of each individual ion detected, APT allows unique insights into the structure of materials at the sub-microscopic level. In the field of functional materials and material systems in particular, new possibilities are emerging for investigating the structure of e.g. nanoscale materials, semiconductor devices and wear-resistant coatings [1,2]. Materials with low to no electrical conductivity can also be studied since the introduction of the laser-assisted measurement mode [3]. Recently, it has repeatedly been reported that the accuracy of the observed elemental composition by APT considerably depends on the employed acquisition parameters [4–17]. In particular, the effective electric field and the influence of the laser pulse energy (LPE) play an important role [18–24]. Awareness that each material to be examined has its own optimal parameter sets is thus essential. Different compositional biases are described in literature, including that the preferred evaporation of low-field components at low LPEs is responsible for an unequal probability for evaporation of different ion species, accompanied by selective loss due to the ion pile-up phenomenon during detector dead-time, a hardware limitation, which is particularly reported for carbides [25–27]. Also the formation of complex molecular ions is observed for excessively high LPEs. The characteristics of the detector hits, where a distinction is made between single and multiple detection events, can be helpful for analyses. A multiple detection event describes the detection of several ions within one detection window. However, this does not necessarily mean that several surface atoms were evaporated by the same pulse. The products of dissociation processes can also lead to an increased amount of multiple detection events. This has been observed for a wide variety of materials [11,20,24,28–30], with GaN being a prominent example [9,13,31]. Particularly neutral dissociated fragments, which are not re-ionized in the electric field and thus do not arrive at the detector, pose a problem here [32].

In the present work, a series of specimens ranging from TiN via $\text{TiC}_x\text{N}_{1-x}$, with $x = 0.25, 0.45, 0.61$ and 0.78 to TiC was systematically investigated for their elemental composition. Special emphasis was placed on the analysis of the electric fields as a function of the LPE, the resulting compositional biases and the detection of potential dissociation processes. Advanced acquisition parameters (AAP) which are available on newer generation atom probes, allow a different view on the evaporation process and were thus utilized within the course of this work to get a deeper insight into the investigated material. On the one hand, their use leads to significantly improved evaporation

conditions and a higher specimen survival rate, but on the other hand it also requires a higher level of knowledge about the material to be examined. It was exemplarily demonstrated on TiN how the different AAPs affect the measurement. The coatings for this study were synthesized using chemical vapor deposition (CVD). Prior to APT experiments, the reference elemental composition was determined using the two complementary ion beam analysis methods, time-of-flight elastic recoil detection analysis (ToF-ERDA) and Rutherford backscattering spectrometry (RBS). Several customized software scripts were developed within the course of this work, including scripts for the filtering of measurements according to the type of detection event, for estimating the effective electric field and for peak decomposition for TiCN specimens. The latter is necessary since three peaks of TiC^{2+} overlap with TiN^{2+} in the mass spectrum, thus an approach with two independent initial conditions was implemented and allows the correction of the obtained elemental composition via natural isotopic abundances.

2. Theoretical background

2.1. Atom probe tomography

APT, a cutting-edge atomic-level materials characterization technique, is the only method capable of identifying individual atoms of all elements in a three-dimensional structure. Over the past decades, significant improvements have advanced the atom probe to its current status as a prestigious characterization tool in materials science. As a prime example serves the state-of-the-art local electrode atom probe, commonly known as LEAP, from the manufacturer CAMECA Instruments, the LEAP 5000 XR at the Department Materials Science in Leoben, which is shown in Fig. 1. This modern instrument shows improvements in the speed of data acquisition, the volume of material that can be analyzed and the variety of materials that can be characterized. The term “tomography”, derived from the Greek words tomos (part) and graphein (to write), originally described the extraction of three-dimensional information from two-dimensional X-ray images. However, it has evolved and covers nowadays any method that produces three-dimensional images of the internal structures of a solid object. In APT, the data on atomic coordinates and the mass-to-charge-state (m/n) ratio are carefully collected atom by atom, resulting in three-dimensional representations of the original atomic distribution in the specimen [2,33–35].



Fig. 1: Atom probe LEAP 5000 XR manufactured by CAMECA Instruments at the Department Materials Science.

The LEAP works on the principle of time-of-flight (ToF) mass spectrometry. The design has been significantly improved over the last decades, including the integration of the local electrode, laser pulse-induced field evaporation and detectors with crossed delay lines. The main components of the LEAP, shown in Fig. 2, consist of a needle-shaped, cryogenically cooled specimen mounted on a nano-positioning stage in ultra-high vacuum, next to the counter electrode with a central circular aperture, the local electrode. By applying a high voltage, a controlled pulsed evaporation behavior can be achieved either by additional pulsing with voltage or laser irradiation [35]. A distinction is made between two flight path designs: the straight flight path and energy compensating reflectron-based instruments. For the latter, researchers developed so-called reflectrons that deflect the ion trajectory to such an extent that the ions are almost completely reversed. They act like electrostatic mirrors with progressively increasing electrostatic fields. Higher energy ions penetrate deeper into the reflectron prior to reflection, extending their ToF. This time-focusing mechanism minimizes the width of peaks in the mass spectrum, leading to a significant improvement in mass resolving power (i.e. mass-to-peak-width ratio, $m/\Delta m$) and consequently a to an improvement in signal-to-noise ratio [36,37]. When an ion reaches the position sensitive detector, its impact on the microchannel plate triggers a cloud of secondary electrons which are subsequently detected in the delay lines. The design with three crossed delay lines allows the position of the impact to be determined precisely [33].

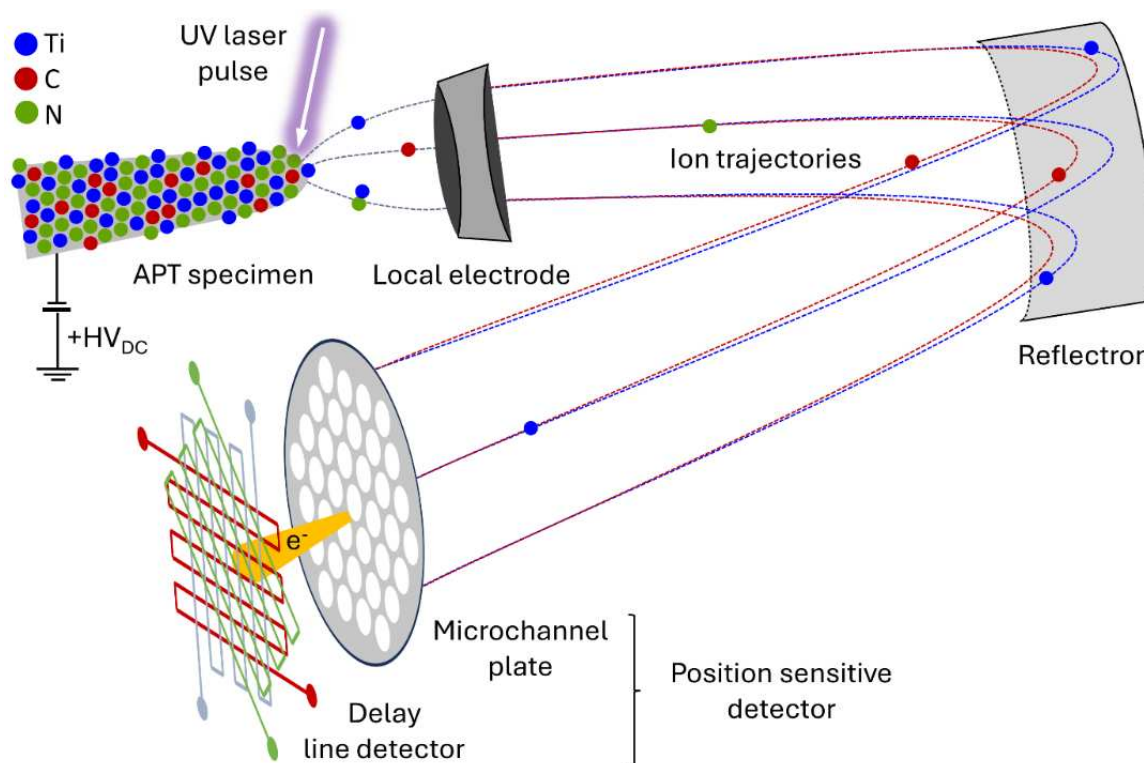


Fig. 2: The operating principle of a reflectron-based LEAP shown schematically.

2.2. From electric field strength to field evaporation

The electric field strength, often simply referred to as the electric field, is a fundamental physical principle that describes the force exerted by a charged particle in the presence of an electric field. This field is a crucial aspect of electromagnetism, which is one of the four fundamental interactions in physics. The electric field strength describes the spatial distribution as well as the strength and direction of this force for each point in space in the form of a vector field [38]. The magnitude of the vector quantity electric field strength E at a point in space is defined by the force F experienced by a positive test charge and its magnitude of charge q [39]:

$$E = \frac{F}{q} \quad \left[\frac{N}{C} = \frac{V}{m} \right] \quad (2.1)$$

In 1928, J. Robert Oppenheimer [40] as well as Ralph Howard Fowler together with Lothar Nordheim [41] independently described the emission of electrons and other charged particles by applying high electric field strengths ($\sim 5 \times 10^7 \text{ V/m}$) and thus, provided the explanation for field emission. Erwin W. Müller, who revolutionized the world of microscopy back in 1937 [42] with the invention of the field emission microscope, showed in 1956 that an electric field in the order of several 10^{10} V/m is sufficient to desorb metallicity bound atoms from the surface by repelling valence electrons and subsequent desorption of ionized atoms [43]. This process is known today as field evaporation and constitutes the basic principle of modern APT [44]. Only a few years later, Müller *et al.* presented the metrology, the atom probe field ion microscope, utilizing a high static electric field superimposed by voltage pulses in order to meet the requirements for a controlled field evaporation, also enabling the identification of evaporated species by ToF mass spectrometry [23,45].

For electric field strength considerations in APT, it is assumed in the easiest case that the electric field does not penetrate the specimen (strictly speaking, this only applies to metals). A potential difference V between a sphere surrounded by another sphere, as shown in Fig. 3a, provides the same relationship for the electric field strength E as a function of the distance r as it is known from a point charge:

$$E = \frac{V}{r} \quad (2.2)$$

However, the situation in APT requires an adaptation of the model as shown in Fig. 3b. The plate corresponds to the local electrode. The radius of the surrounding sphere is infinitely large. Also, due to the geometric expansion and the associated occurring shank angle, the electric field strength is diminished. This is considered by a dimensionless constant, the k factor, also known as the electric field factor, revealing the fundamental equation for the electric field used in APT [46]:

$$E = \frac{V}{k \cdot r} \quad (2.3)$$

Typical values for the k factor range between 2 and 5. Calculations, which demonstrated a strong dependence of the k factor on the diameter of the aperture of the local electrode, led to the current practice of employing a k factor of 3.3 when utilizing a standard local electrode from CAMECA Instruments with an aperture diameter of $\sim 40 \mu\text{m}$. It should be noted that this, strictly speaking, only applies to wire specimens with a 50 nm tip radius and a 10° shank angle [33,46]. Since the applied voltage is usually in the range between 2 and 10 kV, it can be deduced from the above equation that the required electric field at the apex of the specimen can only be achieved with tip radii less than 200 nm.

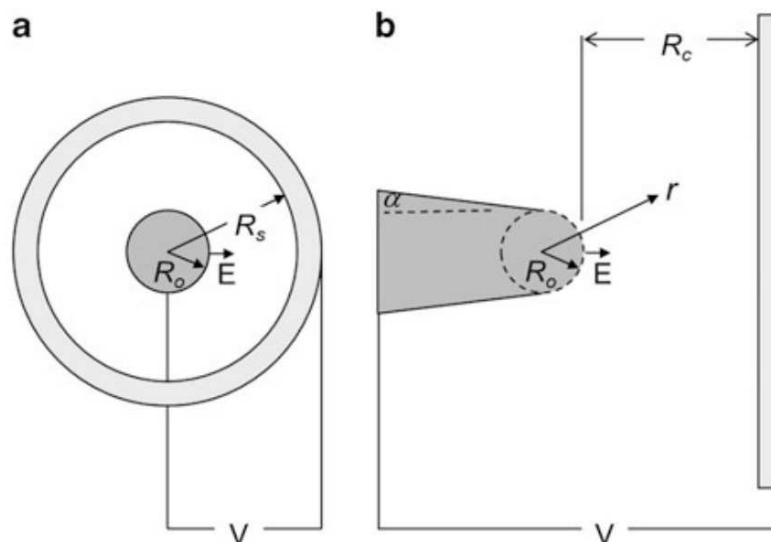


Fig. 3: Electric field strength considerations for (a) a metal sphere (Radius R_o) with no field penetration surrounded by a larger sphere (Radius R_s) and (b) a needle shaped specimen with a shank angle α and tip radius R_o facing a plate at distance R_c . In both cases a potential difference V occurs and the electric field E is expressed as a function of the distance r from the center of the sphere [33].

From a quantum mechanical point of view, the escape of an ion during field evaporation is triggered by thermal activation to overcome the potential energy barrier Q_n , the activation energy barrier for field evaporation of a n -fold charged ion [33,47–49]. As can be seen in Figs. 4a-c, the potential curve is severely deformed by the application of an electric field. Starting from the situation shown in Fig. 4a, where a deep zero-field barrier Q_0 occurs without the presence of an electric field. It can be observed that this barrier becomes smaller as the electric field increases, as shown in Fig. 4b, where the field strength is <10 V/nm. Of particular interest for atom probe operation is the electric field strength at which the barrier Q_n becomes zero (usually $E >10$ V/nm), the so-called zero-barrier evaporation field (ZBEF) [50], shown in Fig. 4c. The field sensitivity $\partial Q_n/\partial E$ close to the ZBEF is also of crucial importance. During acquisition, field strengths near below the ZBEF are aimed for and with the knowledge of how sensitively the energy barrier reacts to a change in the electrical field under certain conditions (i.e., at a distinct temperature), controlled pulsed evaporation can be achieved [47]. At this certain field strength, the evaporation of ions is very likely and thus it forms the operating point in APT. The effective operating flux R (ions/s) during field evaporation follows an Arrhenius approach and is given as:

$$R = n_{hr} A e^{\frac{-Q_n(E)}{k_B T}} \quad (2.4)$$

where

n_{hr} Number of surface atoms within the field of view

A Pre-factor, often equated with the surface atom vibration frequency

$Q_n(E)$ Activation energy barrier as a function of the applied electric field strength

k_B Boltzmann constant

T Temperature

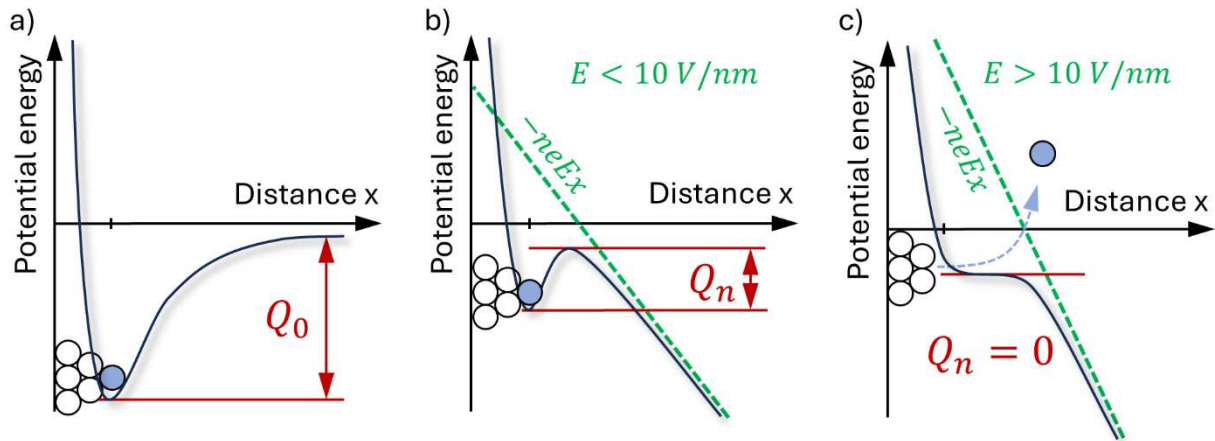


Fig. 4: Schematic potential energy curves for the potential energy of a surface atom where (a) no field is applied, (b) the energy barrier is lowered due to an applied electric field (E) and (c) an ion is evaporated due to the applied zero-barrier evaporation field. Q_0 is the zero-field activation energy and Q_n the activation energy barrier for field evaporation of a n -fold charged ion, which is dependent upon the electric field strength.

Inducing the evaporation by laser irradiation is nowadays commonly used in laser-assisted APT. Due to inelastic interactions of the particles heat is generated and the temperature increases. As a further consequence, in accordance with equation (2.4), the flux R will increase [51]. However, the temperature at the surface of the specimen is not well known, thus, the electric field cannot be calculated accurately [33]. It is therefore almost impossible to make reliable predictions about the charge states that occur when different laser pulse energies are used.

2.3. Post-ionization of field-evaporated ions

Using Brandon's criterion [52], which states that ions evaporate in the charge state that results in the lowest zero-barrier evaporation field, it can be predicted that most ions evaporate in single or double charge state. However, in APT commonly different and, in particular, higher charge states are detected. The theory of post-ionization, developed by David R. Kingham and Roger Haydock in 1980 [53,54], provides an explanation for the higher charge states that occur. It allows one or more further ionizations after the actual escape by quantum tunneling of electrons within the electric field. The prediction of charge states is subject to certain probabilities. Kingham calculated the composition of the charge states for all metals as a function of the evaporation field. The graphical solutions are also known as Kingham curves [55], the one used within this work for Ti is presented in Fig. 5.

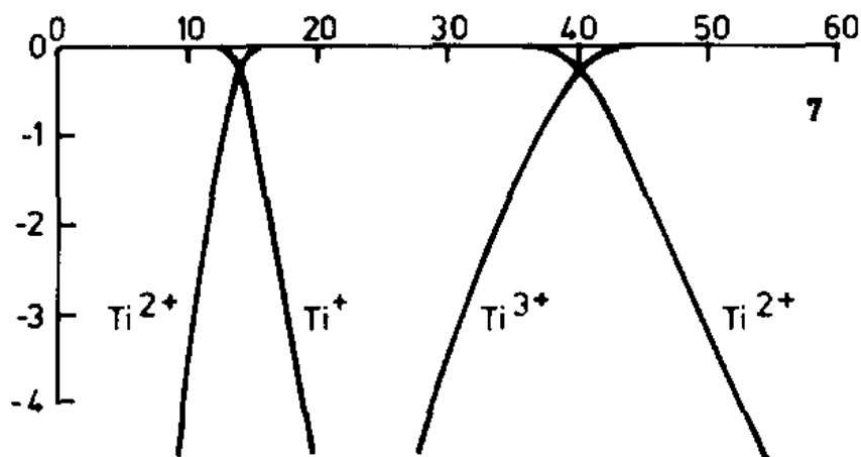


Fig. 5: Original Kingham curve for Ti, on the x-axis is the electric field in V/nm and on the y-axis the proportion in log10 of the respective charge states [55].

It can be seen from the curves, that the ions are post-ionized in two different charge states over a wide range. This circumstance is used to estimate the local electric field strength at the apex based on the observed charge state ratios (CSR, e.g. Ti³⁺/Ti²⁺).

2.4. Ranging and peak decomposition

The mass spectrum of an APT measurement consists of peaks and a certain background level, as shown schematically in Fig. 6. While the sharp peaks can be assigned to a specific ion species based on their m/n ratio, the background mostly originates from evaporation events that were not triggered by a pulse and therefore the ToF could not be clearly determined. The mass spectrum as a histogram is used to assign hits to the corresponding ion species, which is called ranging and constitutes the chemical identification [33]. Like in Fig. 6, the m/n lower (a) and upper limits (c) are defined and all hits within this range are assigned to the selected species. Two aspects are of particular importance:

- I) In terms of elemental composition, accuracy is crucial. When ranging, the background counts (B) are also included, so the actual signal (S) for the counting statistics can be determined using background correction. The local-range background model is an example of the various correction models. Here, the background level is estimated in a background estimate range (1) before each peak and used for statistical correction [56].
- II) Imaging precision is important for the three-dimensional reconstruction, since all ranged hits are displayed with the species assigned to them. A separation between signal and background cannot be made here, therefore a low background level is of interest. Peaks of low intensity or with overlaps are affected by a lack of precision, as there is no clear distinction possible [33,57].

Materials with poor thermal conductivity show so-called thermal tails in the mass spectrum, especially in laser-assisted mode. Their origin is attributed to delayed evaporation during the laser pulse. In contrast to a voltage pulse, the thermal energy introduced during a laser pulse cannot be dissipated instantaneously. To ensure high elemental accuracy, a consistent approach for the selection of range limits should be used when ranging mass spectra with different elements [58]. One that has become established is symmetrical ranging, where the lower m/n limit of a peak is defined by the first time the signal exceeds the background level (a). The center of the range is characterized by the m/n ratio at the maximum of the peak (b), from which the upper m/n limit of the range (c) results automatically.

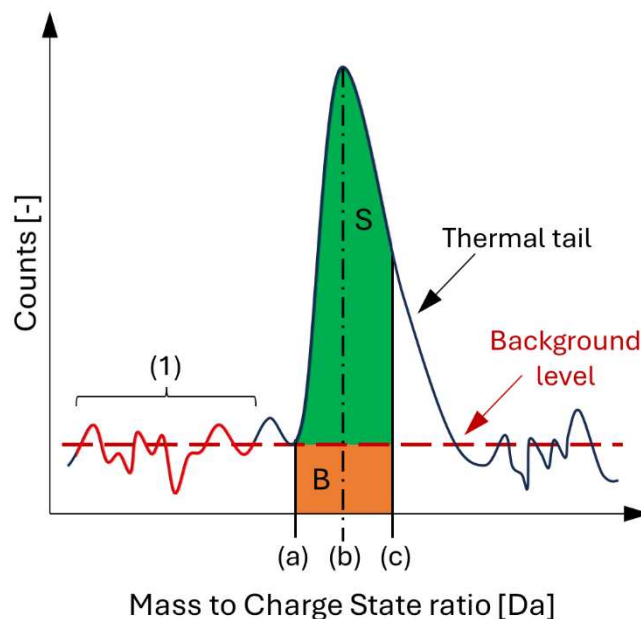


Fig. 6: Components of a peak, containing signal S and background B , in the mass spectrum shown schematically. The symmetrical peak range around the maximum at (b) extends from (a) to (c). Exceeding the background level (red dotted line) for the first time marks the onset of the peak range (a). (1) marks the background estimate range. A thermal tail shows that the peak is not symmetrical. Inspired by [33].

Occasionally two or more peaks overlap at a certain m/n ratio. The imaging precision of the overlapping species is lost as a result. Also the elemental accuracy is affected, as one species is always overestimated and the other underestimated. In order to overcome these inherent limitations, peak decomposition is applied. Due to the different natural abundances, the isotopes exhibit characteristic abundance patterns in the mass spectrum, the fingerprints of the elements. These patterns are usually used to quickly recognize whether and in what composition an overlap exists. Newer generations of atom probes have a remarkably high mass resolving power ($m/\Delta m$, MRP), m/n differences in the hundredths range are sufficient to see peaks with two maxima in the mass spectrum (e.g. $^{14}\text{N}^+$ and $^{28}\text{Si}^{2+}$). In the context of this work, however, the overlaps of the peaks of TiC^{2+} with TiN^{2+} do not allow a sole differentiation based on the MRP [33,59]. The first step is to define the goal of a peak decomposition, high elemental accuracy, or high image precision. The former aims for the correct fraction of an ion species from the total peak, which is known as collective differentiation and is limited to bulk considerations. The latter aims to determine the exact identity of each ion, which is referred to as discrete differentiation. This is possible to a limited extent for overlaps that can be sufficiently separated by very high MRP. The aim of this work is clearly focused on high elemental

accuracy [33]. Fig. 7 illustrates the situation that occurs in all TiCN specimens within this work. Through the five Ti isotopes, the characteristic abundance patterns of the Ti-containing molecules arise. C and N each have a dominant first (^{12}C , ^{14}N) and a weak second isotope (^{13}C , ^{15}N), resulting in severe peak overlaps of TiC^{2+} with TiN^{2+} at 30.0, 30.5 and 31.0 Da. Hereinafter, the procedure and the mathematical concept for the applied peak decomposition are explained.

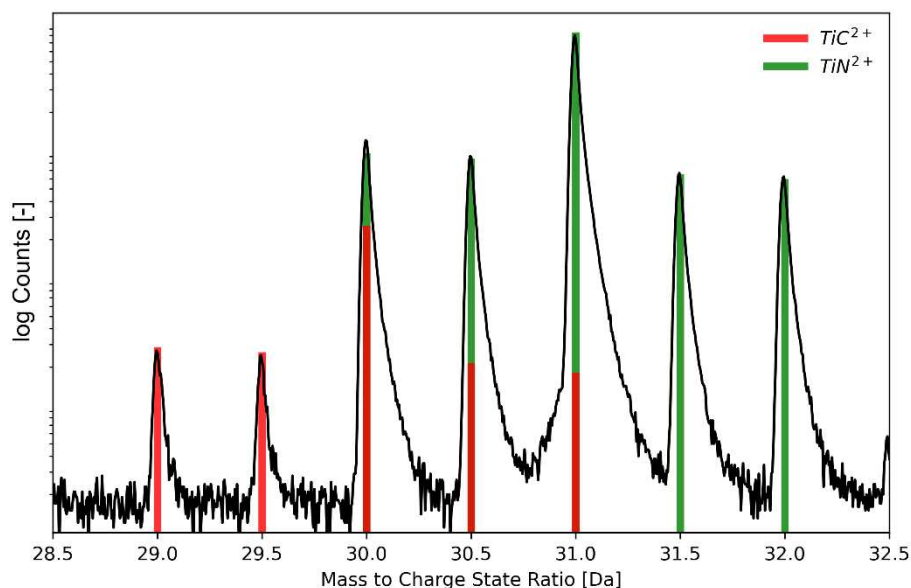


Fig. 7: Peak overlaps of TiC^{2+} and TiN^{2+} in the mass spectrum of $\text{TiC}_{0.25}\text{N}_{0.75}$ at 30, 30.5 and 31 Da.

Since this collective differentiation is based on the natural isotopic abundances, these must be determined in advance for the molecular ions TiC and TiN . The elemental isotopic abundances listed in Table 1 are used for this purpose [60].

Table 1: Atomic masses and their natural isotopic abundancies [60].

Isotope	Mass [amu]	Abundance [-]	Isotope	Mass [amu]	Abundance [-]
<i>Carbon</i>			<i>Titanium</i>		
^{12}C	12.000	0.9889	^{46}Ti	45.953	0.0825
^{13}C	13.003	0.0107	^{47}Ti	46.952	0.0744
<i>Nitrogen</i>			^{48}Ti	47.948	0.7372
^{14}N	14.003	0.9964	^{49}Ti	48.948	0.0541
^{15}N	15.000	0.0036	^{50}Ti	49.945	0.0518

All possible permutations are considered. The molecular mass is the sum of the atomic masses involved. The molecular isotopic abundance, in turn, is obtained by multiplying the atomic isotopic abundances of the isotopes involved. All TiC and TiN isotopes, their masses and abundancies are listed by ascending mass in the following Table 2. The isotopes of TiC and TiN with similar mass are grouped and highlighted in bold.

Table 2: Molecular masses and their natural isotopic abundance patterns.

Isotope	Mass [amu]	Abundance [-]	Isotope	Mass [amu]	Abundance [-]
<i>Titanium carbide</i>			<i>Titanium nitride</i>		
$^{46}\text{Ti } ^{12}\text{C}$	57.953	0.0816			
$^{47}\text{Ti } ^{12}\text{C}$	58.952	0.0736			
$^{46}\text{Ti } ^{13}\text{C}$	58.956	0.0009			
$^{48}\text{Ti } ^{12}\text{C}$	59.948	0.7290			
$^{47}\text{Ti } ^{13}\text{C}$	59.955	0.0008	$^{46}\text{Ti } ^{14}\text{N}$	59.956	0.0822
$^{49}\text{Ti } ^{12}\text{C}$	60.948	0.0535	$^{46}\text{Ti } ^{15}\text{N}$	60.953	0.0003
$^{48}\text{Ti } ^{13}\text{C}$	60.951	0.0079	$^{47}\text{Ti } ^{14}\text{N}$	60.955	0.0741
$^{50}\text{Ti } ^{12}\text{C}$	61.945	0.0512	$^{48}\text{Ti } ^{14}\text{N}$	61.951	0.7345
$^{49}\text{Ti } ^{13}\text{C}$	61.951	0.0006	$^{47}\text{Ti } ^{15}\text{N}$	61.952	0.0003
$^{50}\text{Ti } ^{13}\text{C}$	62.948	0.0006	$^{48}\text{Ti } ^{15}\text{N}$	62.948	0.0027
			$^{49}\text{Ti } ^{14}\text{N}$	62.951	0.0539
			$^{50}\text{Ti } ^{14}\text{N}$	63.948	0.0516
			$^{49}\text{Ti } ^{15}\text{N}$	63.948	0.0002
			$^{50}\text{Ti } ^{15}\text{N}$	64.945	0.0002

Some of the isotopes differ in their masses only by a few thousandths of atomic mass unit. In these cases, the MRP is not high enough to differentiate between them in the mass spectrum, especially as the abundances are partly very weak. For this reason, the abundances were merged appropriately and are presented in Table 3 together with the m/n ratio for the charge state 2+. The table shows the application-specific expected peaks and their abundance. The four overlapping peak positions are highlighted in bold. However, due to the low abundance of TiC^{2+} at 31.5 Da, peak decomposition is omitted for this position.

Table 3: Expected peaks and corresponding overlaps of TiC^{2+} and TiN^{2+} and associated natural abundancies.

m/n [Da]	Abundance [-]	
	TiC^{2+}	TiN^{2+}
29.0	0.0816	-
29.5	0.0745	-
30.0	0.7298	0.0822
30.5	0.0614	0.0744
31.0	0.0518	0.7348
31.5	0.0006	0.0566
32.0	-	0.0518
32.5	-	0.0002

The data listed above provide the basis for peak decomposition. The underlying mathematical concept is explained in more detail below. The counts of an ion species in a certain peak range can be defined in two ways: On the one hand, it is proportional to the total counts of the ion species according to the natural abundance and, on the other hand, it can be expressed by the fraction of the measured counts in the peak range [33]. The fundamental equation is as follows:

$$f_{ij}A_i = \alpha_{ij}M_j = c_{ij} \quad (4.1)$$

where

- i Ion species
- j Range [Da]
- f_{ij} Natural abundance of ion species i in range j
- A_i Total counts of ion species i (within the same charge state)
- α_{ij} Fraction of ion species i in range j
- M_j Measured counts in range j
- c_{ij} Counts of ion species i in range j

First of all, peaks with no overlap (i.e. $\alpha = 1$) are used to determine the total counts of the ion species within the same charge state A_i . For TiC^{2+} the $^{46}\text{Ti}^{12}\text{C}^{2+}$ peak at 29 Da is used, so one can write

$$\alpha_{\text{TiC},29} = 1 \text{ and } f_{\text{TiC},29} = 0.0816.$$

Similar for TiN^{2+} , the peak related to the more abundant $^{50}\text{Ti}^{14}\text{N}^{2+}$ as well as the $^{49}\text{Ti}^{15}\text{N}^{2+}$ isotope at 32 Da are used, following is

$$\alpha_{\text{TiN},32} = 1 \text{ and } f_{\text{TiN},32} = 0.0518.$$

The measured counts of a peak M_j are delimited by the corresponding range j and can thus be determined directly from the mass spectrum.

Equation (4.1) is used to determine the total counts of TiC^{2+} and TiN^{2+} :

$$A_{\text{TiC}} = \frac{\alpha_{\text{TiC},29} M_{29}}{f_{\text{TiC},29}}$$

and

$$A_{\text{TiN}} = \frac{\alpha_{\text{TiN},32} M_{32}}{f_{\text{TiN},32}}$$

For the peak decomposition at 30, 30.5 and 31 Da, the equation (4.1) is reformulated in

$$c_{\text{TiC},j} = f_{\text{TiC},j} A_{\text{TiC}}, \quad j \in \{30, 30.5, 31\} \quad (4.2)$$

and

$$c_{\text{TiN},j} = f_{\text{TiN},j} A_{\text{TiN}}, \quad j \in \{30, 30.5, 31\} \quad (4.3)$$

Since the results obtained by equations (4.2) and (4.3) are independent, they do not necessarily satisfy the condition that the sum of TiC and TiN counts of ions in the same range equals the measured counts. Thus, an additional constraint is introduced:

$$c_{\text{TiC},j} + c_{\text{TiN},j} = M_j, \quad j \in \{30, 30.5, 31\} \quad (4.4)$$

Transforming and substituting in equation (4.1) allows the calculation of TiC and TiN counts in the respective ranges:

$$c_{TiC,j} = M_j - (f_{TiN,j}A_{TiN}), \quad j \in \{30, 30.5, 31\} \quad (4.5)$$

and

$$c_{TiN,j} = M_j - (f_{TiC,j}A_{TiC}), \quad j \in \{30, 30.5, 31\} \quad (4.6)$$

Finally, for $c_{TiC,j}$ and $c_{TiN,j}$, mean values for the respective ranges are determined from equations (4.2) and (4.5) as well as (4.3) and (4.6). This allows on the one hand statements about the error and on the other hand, the condition from equation (4.4) is fulfilled under any circumstances.

A necessity for achieving high elemental accuracy is the correction of Co counts. Co is a single isotope element and diffuses from the WC-Co substrate into the coating during deposition at high temperatures. The $^{59}\text{Co}^{2+}$ peak overlaps with TiC at 29.5 Da, the Co counts are determined and the elemental composition is corrected using the following approach:

$$c_{Co,29.5} = M_{29.5} - (f_{TiC,29.5}A_{TiC}) \quad (4.7)$$

2.5. Ion pile-up phenomenon

A notable limitation of a position sensitive delay line detector is its ability to resolve signals of closely spaced and/or simultaneous arriving ions. The functional principle of the detector is shown schematically in Fig. 8. After the impinging ion has triggered a cloud of secondary electrons in the microchannel plate, this cloud hits the three meander-shaped delay lines. The electrons generate a total of six electrical signals which's propagation times are recorded at the ends of the delay lines. The x-y position can thus be determined from the three independent time differences ($\Delta t_{X,Y,W}$). The mean value of the time stamps \bar{t} is used as the ToF for the hit, which in turn is used to derive the m/n ratio. The third delay line W is added and rotated by 45° to improve the multi hit resolution [33].

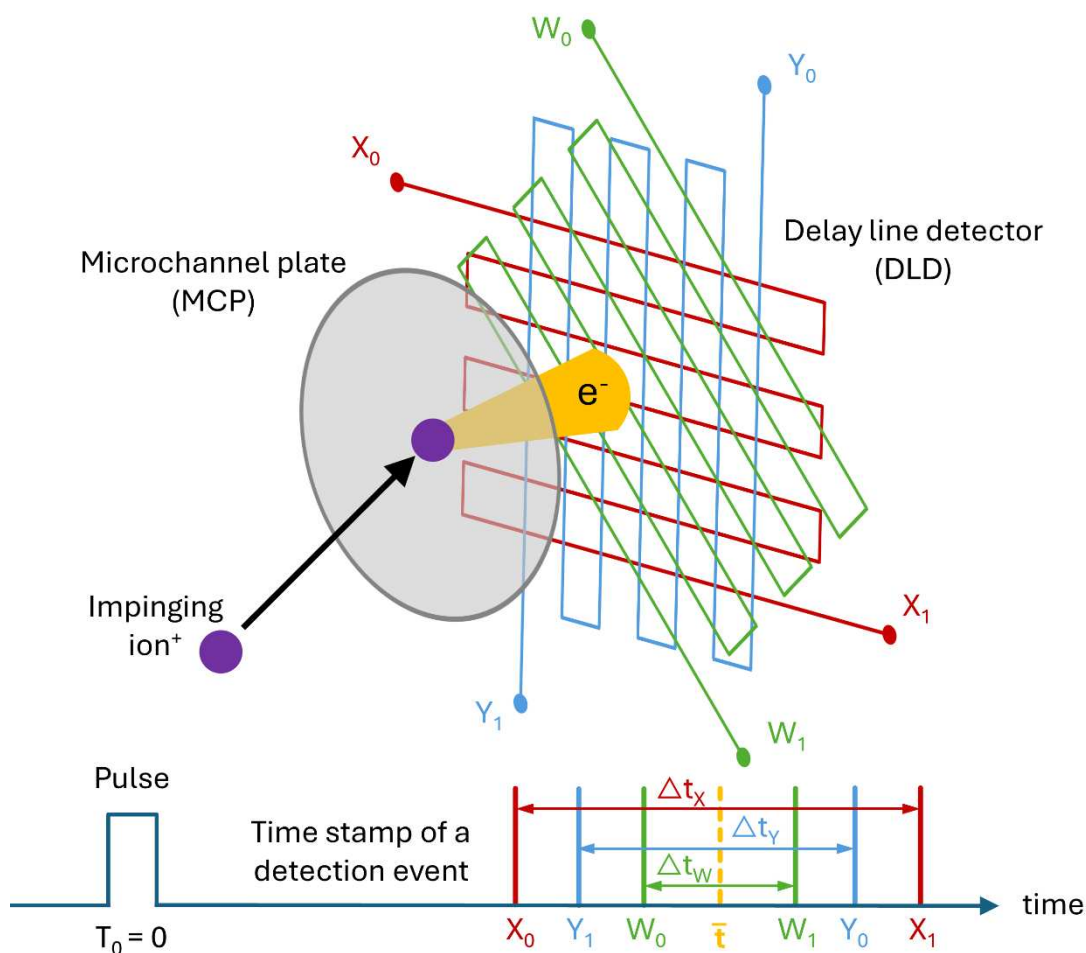


Fig. 8: Schematic diagram of the detector design, consisting of the microchannel plate and the three-anode delay line detector. An exemplary time stamp illustrates how time differences are recorded and ToF \bar{t} is derived.

The detection capabilities of an atom probe are hindered by the detector deadtime (usually reported to be ~ 3.5 ns [61]), which is a hardware limitation. The challenges arise with the processing of multiple detection events that occur within a short period of time and close spatial proximity. This phenomenon is illustrated in Fig. 9, where only one straight delay line is shown for better visualization. The first ion impinges and the secondary electrons cause two signals propagating towards the ends of the delay line. The unfortunate position and the short time difference between the arrival of the first and second ion causes a pile-up of signals that can no longer be resolved, not even by deconvolution using complex algorithms. This creates a dead zone and dead time at the detector, resulting in a loss of data. A qualitative assessment of whether a pile-up is present can be made by determining the apparent isotopic abundance ratios. Since the loss is proportional to the isotopic abundances, there is an apparent underestimation of the major isotope and an overestimation of the minor isotope(s). Although quantitative corrections have been reported in the literature [26,61,62], the uncertain detection efficiency and the unknown ion emission from the specimen make 100 % accuracy elusive [2].

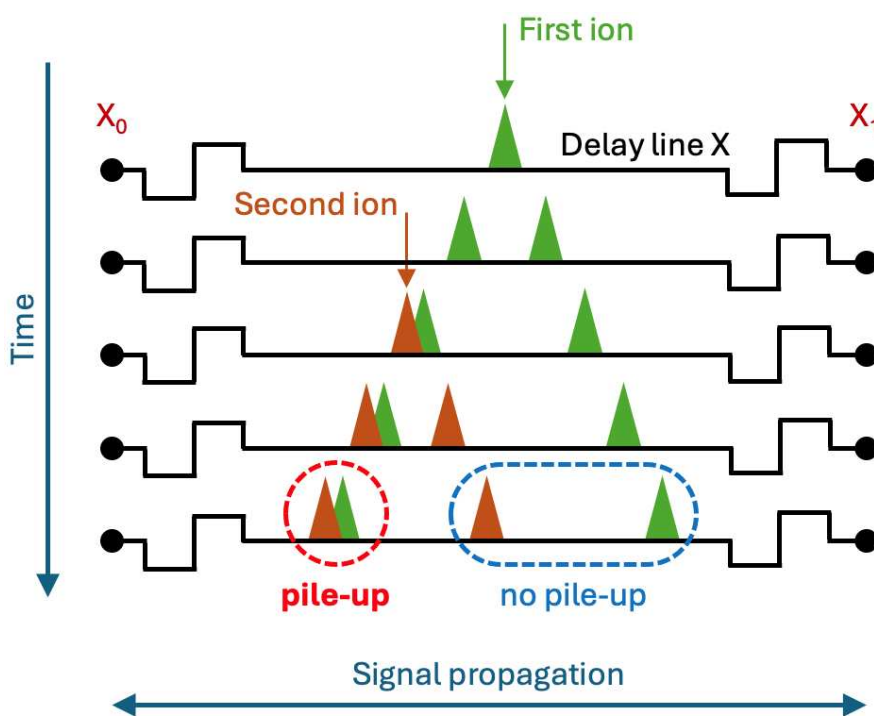


Fig. 9: Time propagation of the signals along a delay line of two ions that have arrived at the detector one after the other. The unfortunate position of the second ion causes a pile-up.

2.6. Dissociation processes

Molecular ions are particularly observed in the field evaporation of covalently and ionically bound materials. Although these are metastable, their lifetime is usually sufficient to reach the detector. In mass spectrometry, little attention has been paid to the effect of dissociation. However, with the effort to improve compositional accuracy, dissociation as a compositional bias became an important focus of investigation [23,63,64]. As long as the fragments of dissociation phenomena are not lost due to pile-ups, they can be detected accordingly and there is no loss of information. However, dissociation processes in which neutral fragments are formed pose a particular problem for the accuracy of the elemental composition. If it is not possible to re-ionize these, they are irretrievably lost. Consequently, it is necessary to investigate whether and to what extent dissociation phenomena are present during a measurement. Saxey [65] has developed an intuitive analysis approach with the ion correlation histogram, also referred to as Saxey plot. Thereby, all multiple detection events of a measurement are considered. In the simplest case, a multiple detection event consists of only two hits and their m/n ratios form the coordinates for the data point. For multiple detection events with three or more hits, all possible permutations are considered. As illustrated in Fig. 10, different tracks become visible, which can be attributed to correlating evaporation processes: Vertical and horizontal tracks (I) originate from an ion evaporated with the pulse, followed by a time-delayed co-evaporated ion. Tracks with a positive slope (II) originate from simultaneous, but delayed evaporation of both ions, for example in laser-assisted mode due to poor thermal conductivity. Delayed evaporation always leads to a longer ToF and thus to higher m/n ratios. However, of greatest interest in ion correlation histograms are the tracks with negative slope (III, red line), which are attributable to dissociation processes [28]. The field-evaporated parent molecule (mass m_p and charge state $n+$) dissociates in flight. The masses split up (m_1, m_2), along with the positive charges ($p+, q+$), but both are retained. The allocation of kinetic energy among the fragments is statistically distributed, resulting in different times-of-flight. However, due to the specific energy relationship, the distribution results in distinct dissociations tracks in the ion correlation histogram. To the best of our knowledge, there is currently no way to make quantitative statements about dissociation using ion correlation histograms. The same applies to the generation of potential neutrals. Nevertheless, it is possible to qualitatively classify which effects exist, providing a basis for changing the evaporation conditions, for example. Special effects are observed with reflectron-based instruments. Di Russo *et al.* [28] report on the various cases of dissociations, their partial compensation, and the inherent difficulties in interpreting tracks. Thus, at the intersections of the parent and daughter molecules, the tracks are compressed and the tracks deviate or are annihilated

under certain conditions. In another study, Peng *et al.* [30] showed that not all dissociation tracks can be visualized with reflectron-based instruments, therefore it is recommended to investigate dissociation using straight flight path instruments.

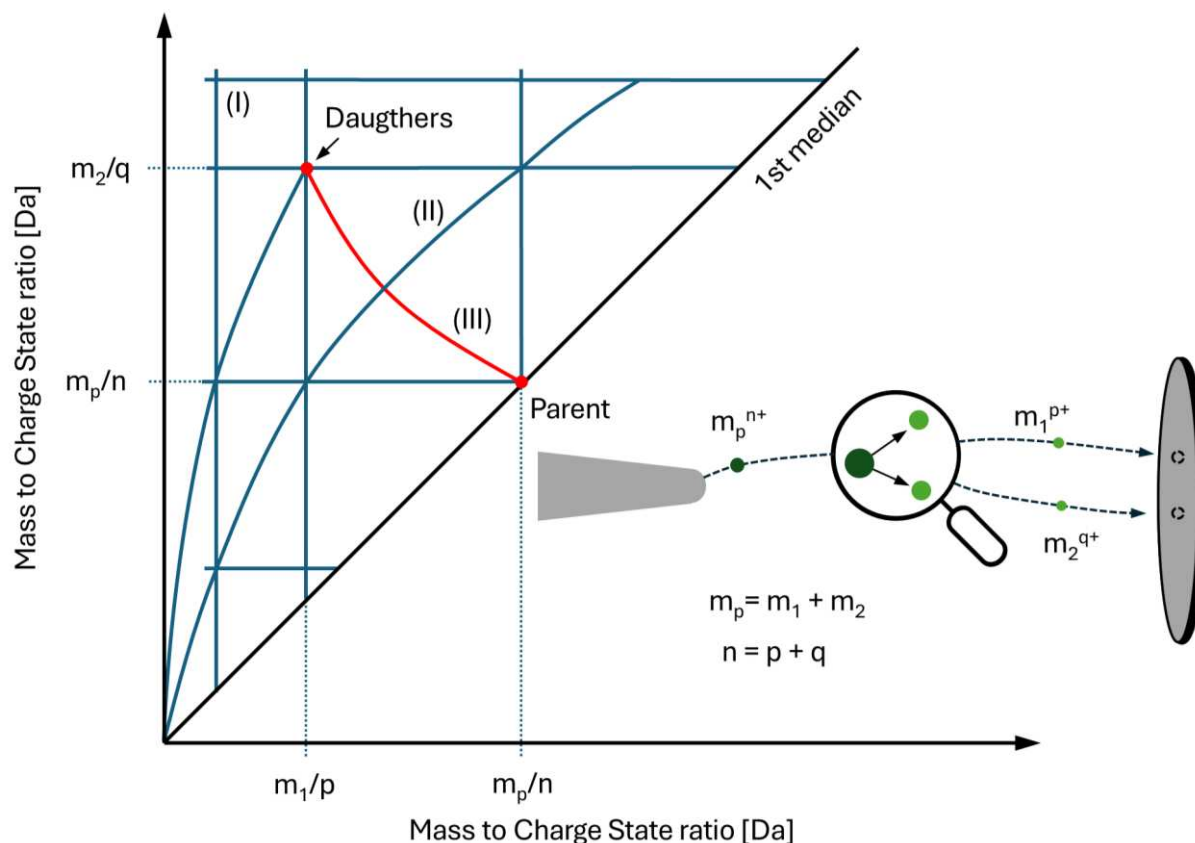


Fig. 10: Ion correlation histogram used for dissociation investigation. Different types of tracks are commonly observed: (I) horizontal and vertical tracks as well as (II) tracks with positive slope and (III) tracks with negative slope (red line), which indicate dissociation and link the parent molecule (m_p) to the daughter molecules (m_1 and m_2).

2.7. Standard acquisition parameters

2.7.1. Acquisition mode

The LEAP 5000 XR applied in this work can be used in three different acquisition modes. In addition to the two APT methods, voltage- and laser-assisted APT, the device is also equipped to perform field ion microscopy with different imaging gases. For the first two, the working principle is similar: A high standing voltage (2-10 kV) is applied to the specimen in order to achieve a controlled and pulsed field evaporation, either by voltage or laser pulsing, as illustrated in Fig. 11. While the electric field is increased by the additional voltage V_{Pulse} in voltage mode, the required field is reduced by the local temperature increase ΔT_{Laser} in laser-assisted mode. Thus, the evaporation limit is exceeded in both cases. As only the laser-assisted mode was used within this work, only the acquisition parameters used are discussed below.

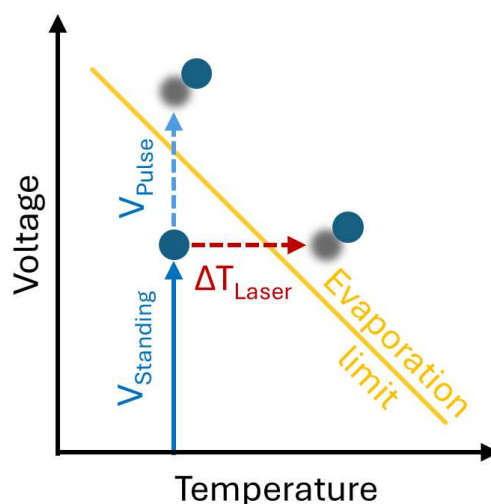


Fig. 11: Illustration of the two different trigger mechanisms, which are used to achieve controlled pulsed field evaporation.

2.7.2. Specimen Temperature (T) [K]

To reduce surface diffusion during acquisition the experiments are carried out at cryogenic temperatures. Measuring the true specimen temperature is not possible due to invincible difficulties (e.g. connection to the specimen or conductors in the electric field), therefore the base temperature is measured below the heater of the cryogenic system and corrected by the cryostat controller. Lowest possible base temperatures offer the highest data quality, since the heat flow from the apex of the specimen gets maximized. However, the analysis yield is limited at very low temperatures which increases with temperature, so it is important to find a balance [2,33].

2.7.3. Detection Rate (DR) [%]

The detection rate (DR), formerly also known as target evaporation rate, is the percentage of pulses that lead to an evaporation event and thus the direct target value for a controlled evaporation behavior. The actual DR serves as direct feedback from the detector to control the standing voltage in auto voltage control mode, which is activated with every APT measurement after successful turn on. Typical values for DR are in the range between 0.5 and 2 % [33].

2.7.4. Laser Pulse Energy (LPE) [pJ]

The energy transferred by phonons during a single pulse is referred to as laser pulse energy (LPE). It is of great importance for the specimen to be in the focal point, but the spot size, the alignment of the specimen and its geometry also have an influence on how the energy is absorbed. At low LPEs, out-of-synch evaporation or preferential retention occurs more frequently. Too high LPE, on the other hand, increases the probability of surface migration due to the high temperatures at the apex of the specimen. Similarly, the generation of complex molecular ions is possible due to insufficient electric field strength or non-uniform evaporation due to shadow effects. It is therefore important to find the best balance with the optimal LPE. A lower LPE is generally recommended for oxides and nitrides [33]. The LEAP 5000 XR is equipped with a UV laser with a wavelength of 355 nm and a pulse duration of <15 ps.

2.7.5. Pulse Rate (PR) [kHz]

The pulse rate (PR) is the repetition rate of pulses used to trigger evaporation. Typical values range between 50 and 350 kHz. The selection depends on the desired m/n range. As the detection window is indirectly determined by the PR, only light or highly charged ion species can be measured with a high PR at low voltages. In contrast, a PR that is too low leads to high and inefficient acquisition times [33].

2.8. Advanced acquisition parameters

2.8.1. Constant field control

Due to the fact that the radius at the apex of the specimen and thus the field of view (FOV) increases over the course of a measurement, the areal evaporation rate (AER, DR per μm^2), maintaining a constant DR, decreases steadily [66]. This correlation can be derived as follows.

Based on the equation for the electric field strength,

$$E = \frac{V}{k \cdot R} \quad (8.1)$$

where

E	Electric field strength [V/nm]
V	Potential (Standing voltage) [V]
k	Electric field (k-) factor [-]
R	Radius [nm]

the radius R can be expressed as a function of the standing voltage V by estimating the electric field strength using Kingham's post-ionization model and by assuming a constant k factor:

$$R_{(V)} = \frac{V}{k \cdot E} \quad (8.2)$$

The projected area A of the hemisphere is given by the equation for the circular area:

$$A_{(R)} = R^2 \pi \quad (8.3)$$

The AER is the normalization of the detection rate DR to this projected area, revealing a $1/R^2$ proportionality:

$$AER_{(R)} = \frac{DR}{A_{(R)}} = \frac{DR}{R^2 \pi} \quad (8.4)$$

where

AER	Areal evaporation rate [$\%/\mu\text{m}^2$]
DR	Detection rate [%]

From several points of view, maintaining a constant AER is preferable rather than keeping the DR constant. This is illustrated in Fig. 12, which compares the evolution of DR and AER during a measurement. Of particular interest here are the prevailing conditions at radius R_1 at the beginning, compared with that at radius R_2 towards the end of the measurement. At a constant DR, the AER is extremely high at the beginning of the measurement and thus, the tip of the specimen is exposed to high stress resulting in possible specimen failure. The AER decreases significantly towards the end so that the measurement is no longer efficient. The AAP constant field control is used to keep the AER constant during a measurement. A target value for the AER (e.g. 100 %/ μm^2) is selected and a field estimate (obtained by the post-ionization model from Kingham, see section 2.3) serves as a basis for the algorithm. The detection rate is made variable by reversing the relationship from equation (8.4).

$$DR_{(R)} = AER \cdot A_{(R)} = AER \cdot R^2\pi \quad (8.5)$$

As can be seen in Fig. 12, with constant AER, the DR is very low at the beginning to preserve the specimen and increases towards the end so that the data can be acquired efficiently.

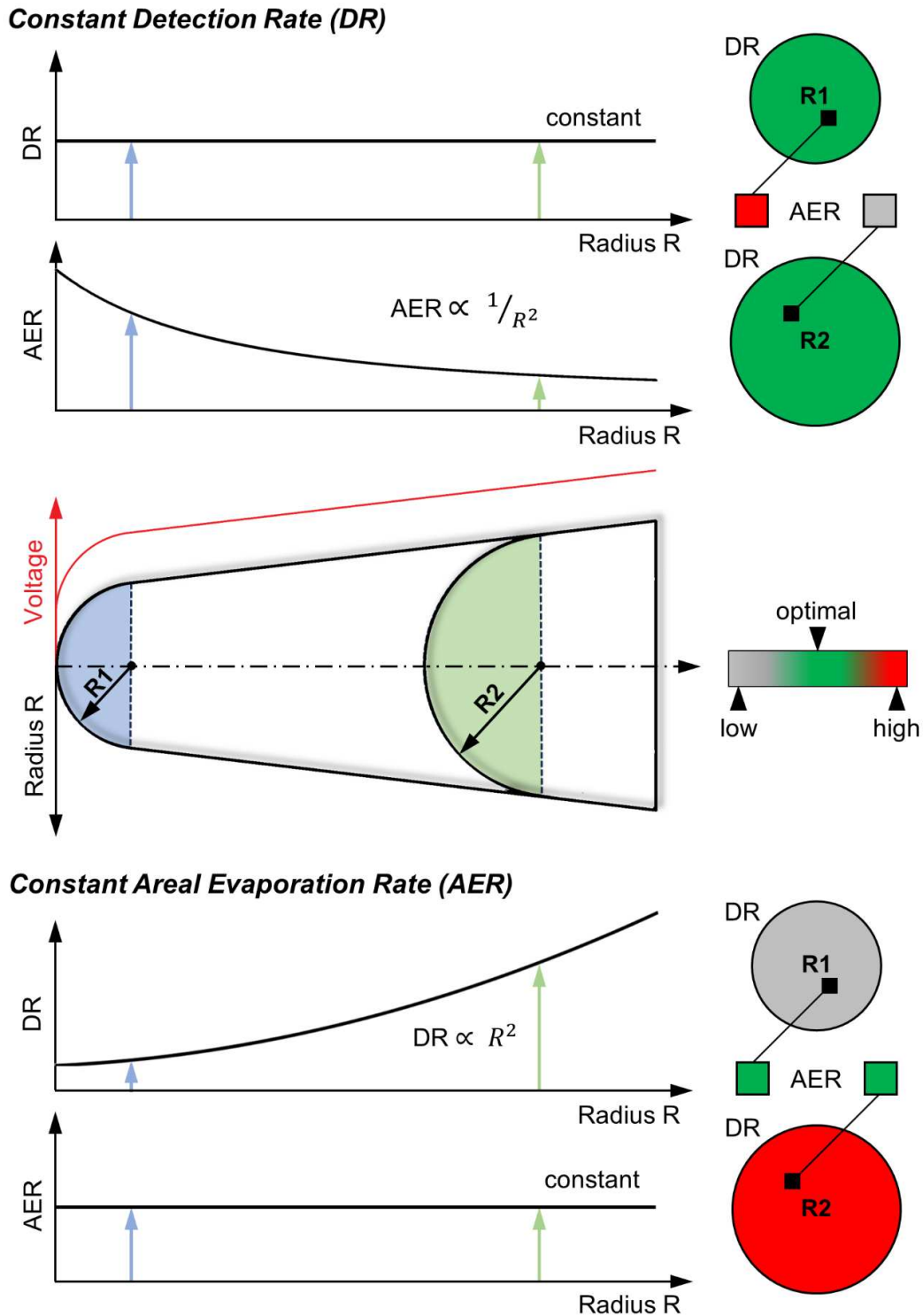


Fig. 12: Illustration of the development of detection rate and areal evaporation rate while maintaining either one of them constant. The prevailing conditions at the two different cross-sections at R1 and R2 are shown as examples and the target values are classified according to the color bar in their order of magnitude.

2.8.2. Auto pulse rate control

With ongoing measurement progress, the standing voltage increases, due to the increasing radius of the tip. However, this is also accompanied by an increasing potential energy which is converted into kinetic energy. Since mass spectrometry is based on ToF, increasing voltage allows higher m/n ratios to be measured while maintaining the same PR. This can lead to inefficient acquisition times, as the PR is chosen at the beginning so that all m/n ratios of interest can be captured within the detection window. This relation can be derived as follows:

The energy conservation approach:

$$E_{pot} = E_{kin} \quad (8.6)$$

Doubling the standing voltage is equivalent to quadrupling the ion velocity:

$$neV = \frac{1}{2}mv^2 = \frac{1}{2}m\left(\frac{L}{t}\right)^2 \quad (8.7)$$

where

E_{pot}	Potential energy	e	Electron charge	v	Ion velocity
E_{kin}	Kinetic energy	V	Voltage (HV _{DC})	L	Flight path length
n	Charge state	m	Ion mass	t	ToF

The basic equation of ToF mass spectrometry can now be derived from this:

$$\frac{m}{n} = \frac{2eVt^2}{L^2} \quad (8.8)$$

Rearranging the equation results in the following expression for the ToF, in which the $1/\sqrt{V}$ proportionality for a distinct m/n ratio becomes visible:

$$t = \sqrt{\left(\frac{m}{n}\right) \frac{L^2}{2eV}} \propto \frac{1}{\sqrt{V}} \quad (8.9)$$

Since the PR is the reciprocal of the detection window time and thus the maximum detectable ToF, the following relationship results:

$$PR \propto \sqrt{V} \quad (8.10)$$

The algorithm for the AAP auto pulse rate control is based on this relationship. The input value is the minimal m/n ratio that can always be detected, the instrument adjusts the PR accordingly to the voltage applied.

2.8.3. Auto pulse energy control

Auto pulse energy control allows the adjustment of specific peak ratios. To do this, a corresponding peak ratio (e.g. $^{48}\text{Ti}^{3+}/^{48}\text{Ti}^{2+}$) must be recorded during the measurement. In addition to the target value for the peak ratio, the input values are the minimum and maximum LPE. Within this range, the algorithm approaches the desired peak ratio by adjusting the LPE. This AAP is used to specifically adjust electric fields at the apex of the specimen and thus, for example, to avoid peak overlaps in the mass spectrum by utilizing the Kingham curves.

3. Methodology

3.1. Investigated materials

The synthesis of TiCN by CVD with the C feeding precursors methane (CH₄) or acetonitrile (CH₃CN) is standard practice [67]. However, while high and thus increasingly uneconomical temperatures of more than 950 °C are required with the first, the C/(C+N) ratio is limited to 50 – 70 % with the latter precursor [68–70]. In recent studies [69,71,72], ethane (C₂H₆) was found to be a convincing alternative C feeding precursor to overcome these issues. Cemented carbide inserts (76 wt.% WC, 12 wt.% mixed carbides and 12 wt.% Co binder) in SNUN geometry (ISO 1832) were used as substrates for the coatings investigated within this work. These have a square surface of 12.6 x 12.6 mm and a height of 4.8 mm. The deposition of the coatings was carried out in an industrial-scale thermal CVD plant of the type SCT600 TH from Sucotec (now Oerlikon Balzers). To prevent diffusion between the coating and the substrate, a TiN base layer with a thickness of ~0.3 μm was initially deposited on all TiCN and TiC specimens. A gas mixture of C₂H₆, TiCl₄, N₂, H₂ and Ar was used for the coating deposition. By varying the volume fraction of the C feeding precursor (0 to 1.52 vol.%), TiN and TiCN with different C/(C+N) ratios were synthesized. The deposition process was carried out at 920 °C and 160 mbar and resulted in coating thicknesses between 5.1 and 6.7 μm [69]. The TiC coating was deposited with a feed gas mixture consisting of C₂H₆, TiCl₄ and H₂ at 885 °C and 100 mbar [73]. The coatings investigated within this work all exhibit a face-centered cubic crystal structure (NaCl-type, space group *Fm* $\bar{3}$ *m*, number 225). Fig. 13 shows micrographs of the polished surfaces of the examined coatings, which reveal a color gradient. TiN is known for its golden color, as the C content increases, the color changes from a dark violet to a metallic grey.

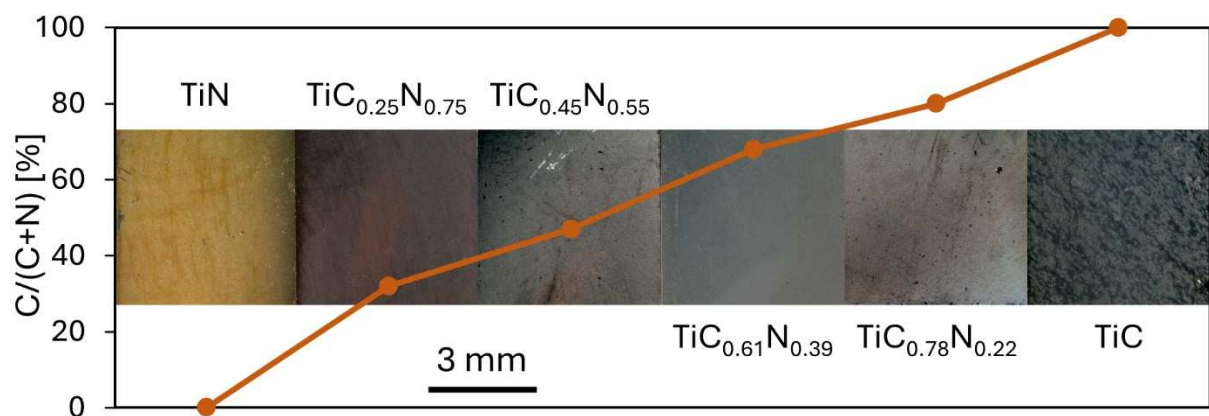


Fig. 13: Micrographs of the analyzed coated specimens shown with increasing C/(C+N) ratio.

3.2. Determination of the reference elemental composition

The 5 MV NEC Pelletron tandem accelerator at the Tandem Laboratory at Uppsala University, Sweden, was used to quantify the elemental compositions, used as reference for the comparisons with APT. 36 MeV I^{8+} ions are utilized in ToF-ERDA and 2 MeV He^+ primary ions are used for RBS. Further information about the experiment and on the uncertainties attributed to the combined metrology can be found in Refs. [74,75]. The following Table 4 shows the elemental compositions obtained by the ToF-ERDA/RBS measurements and the corresponding C/(C+N) ratios in percent. From this, it can also be seen that the Ti/(C+N) ratio is ~ 1 , which is attributed to the occupation of metallic Ti sites and non-metallic C and N sites in the ionic crystal lattice. From the results, TiN and TiC are considered to be stoichiometric.

Table 4: Elemental compositions and their uncertainties according to complementary ToF-ERDA/RBS.

Specimen	Ti [at.%]	C [at.%]	N [at.%]	C/(C+N) [%]
TiN	49.40 \pm 1.54	-	50.60 \pm 1.54	0
TiC_{0.25}N_{0.75}	49.34 \pm 1.79	12.78 \pm 0.67	37.88 \pm 1.16	25.2 \pm 1.6
TiC_{0.45}N_{0.55}	49.24 \pm 2.00	22.82 \pm 1.17	27.94 \pm 0.87	45.0 \pm 2.1
TiC_{0.61}N_{0.39}	51.09 \pm 2.11	29.72 \pm 1.52	19.19 \pm 0.66	60.8 \pm 2.1
TiC_{0.78}N_{0.22}	49.09 \pm 2.35	39.69 \pm 2.02	11.22 \pm 0.41	78.0 \pm 1.6
TiC	49.35 \pm 2.55	50.65 \pm 2.55	-	100

3.3. Specimen preparation

A novel approach for specimen preparation was employed within this work. The procedure is represented in Fig. 14 and involves three stages. First, the cutting insert was cut in half's using an Accutom 5R precision saw from Struers. One part was used for the ToF-ERDA/RBS measurements. The other part, the actual specimen, was thinned to ~ 400 μm on the coating side. In the second stage, a 3D-Micromac microPREP PRO FEMTO fs-laser system was used to first cut a 7×3 mm^2 coupon. Two rows with a total of 15 pre-thinned posts were then created by ablating ~ 130 μm of the top surface. These posts are 500 μm apart and reveal a tip diameter of ~ 35 μm . This ensured that no artifacts were introduced by the laser and thus the coating remained unaffected. This innovative approach was first described by Tkadletz *et al.* [76]. The laser parameters employed are summarized in Table 5. In the third and final stage, the microtip coupon was first mounted on a Cu clip, the specimen carrier provided by CAMECA. In Figs. 15a-b an overview of the coupon and a pre-sharpened post prior to further processing can be seen. The posts were then shaped by focused ion beam (FIB) milling in an FEI Versa dual beam SEM/FIB workstation using 30 nA, until they revealed a post diameter of 6.5 μm , as shown in Fig. 15c. Followed by several consecutive annular milling steps, according to the standard procedure described in Ref. [77], ready-to-run APT specimens were prepared. Fig. 15d shows the specimens after milling with an inner diameter of ~ 1 μm , revealing the microstructure of the substrate, the cemented carbide, and the interface to the coating. Figs. 15e-f show an overview of the post after preparation and the finished specimen in detail with a final tip radius < 50 nm.

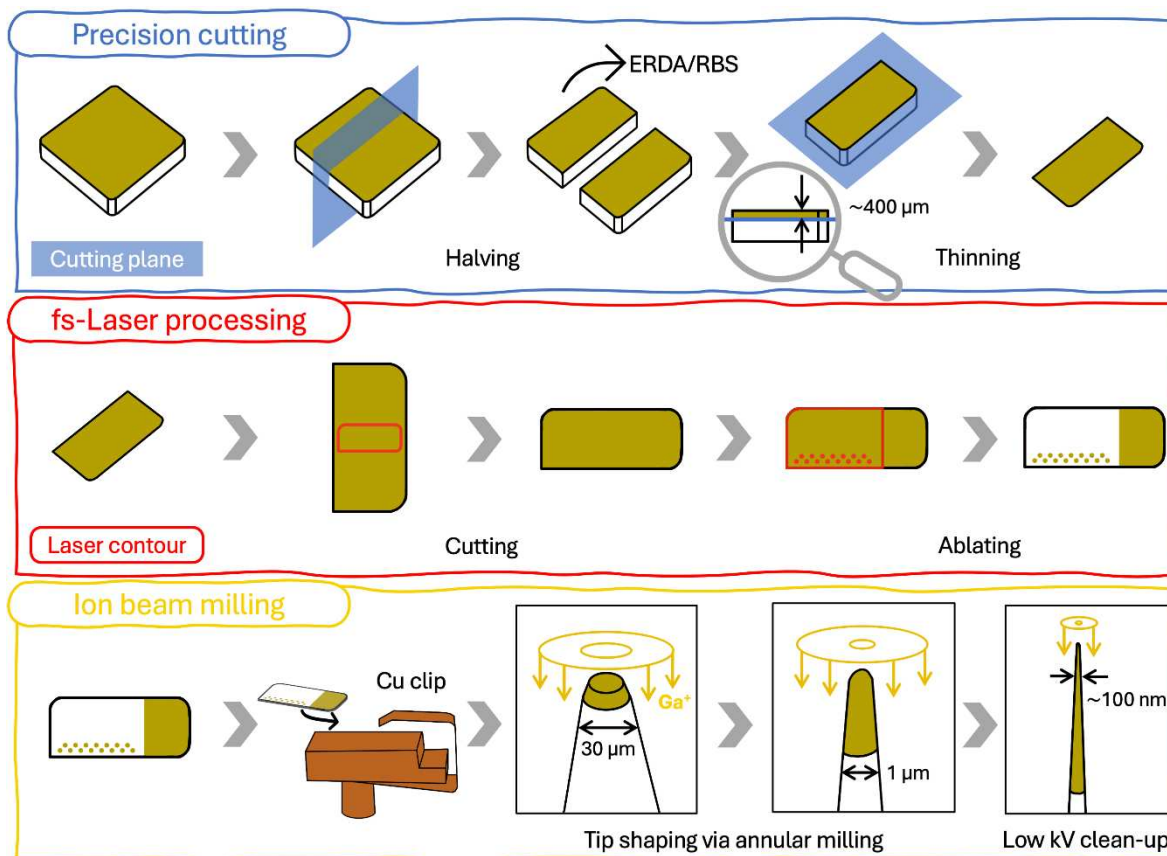


Fig. 14: Schematic illustration of the workflow in the three-stage preparation procedure using a precision saw, a fs-laser ablation system and a SEM/FIB workstation.

Table 5: Employed parameters in fs-laser processing.

Parameter	Procedure	
	Cutting	Ablating
Power [W]	1.00	0.05
Pulse frequency [kHz]	60	60
Number of repetitions [-]	920	375
Pulse and line distance [μm]	4.0	3.0
Scan regime	Rotated	Rotated
Work angle [°]	0	0
Focus shift	On	Off
Number of focus levels [-]	25	-
Processing depth [μm]	500	-

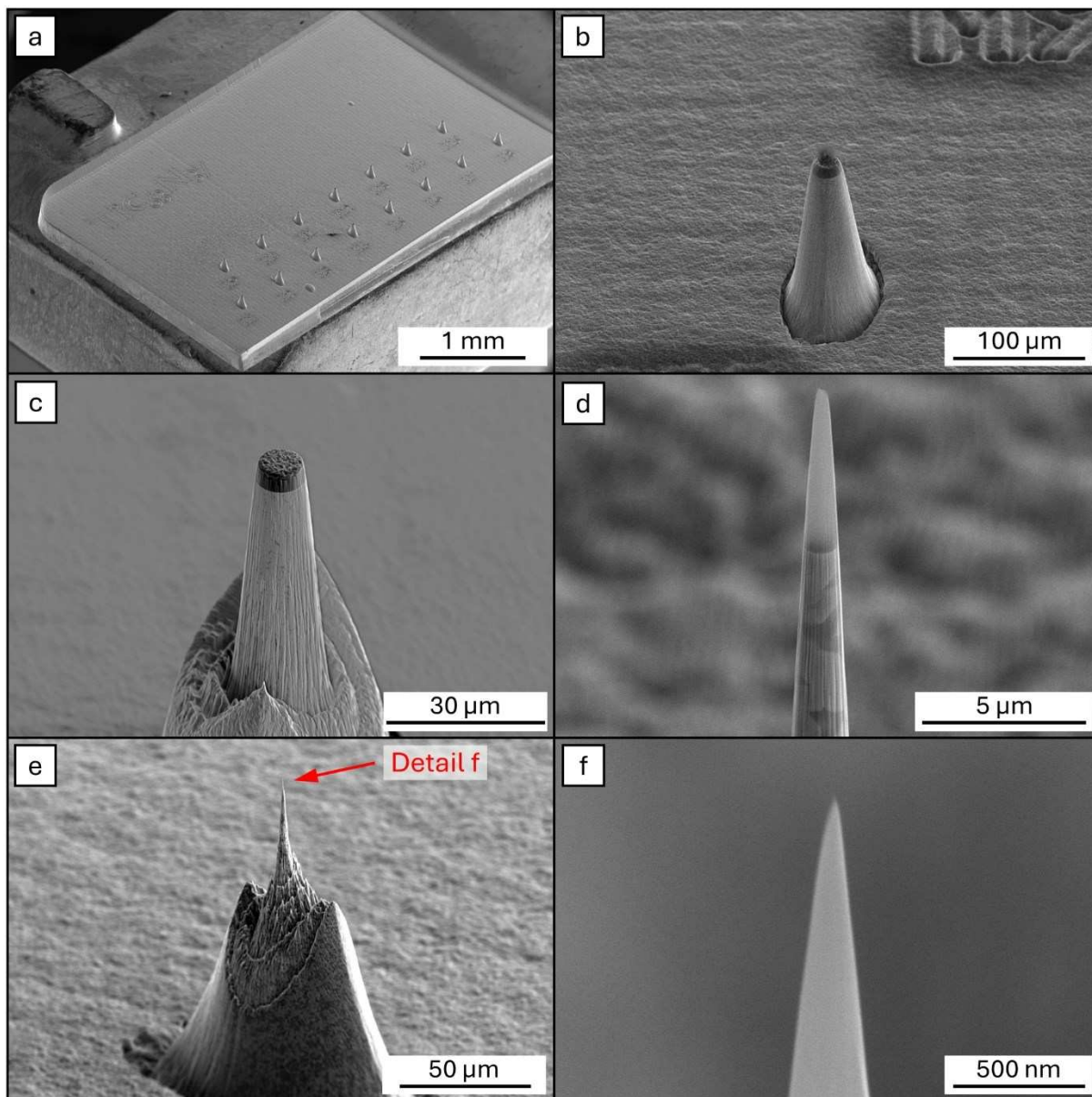


Fig. 15: SEM images of the sample preparation using FIB. (a) Overview image of the lasered microtip coupon with two rows of microtips. (b) Pre-thinned post with coating on the flat surface. (c) Exposed specimen, with a diameter of $\sim 10 \mu\text{m}$. (d) Apex of the specimen after annular milling with 0.5 nA FIB current, revealing the interface between the coating and the cemented carbide substrate. (e) Overview image of the microtip after milling, the red arrow indicates the final APT specimen shown in (f) after the low kV clean-up step with a tip radius of $\sim 30 \text{ nm}$ and a half shank angle of $\sim 7^\circ$.

3.4. Atom probe tomography measurements

3.4.1. Data acquisition

All performed measurements within the course of this work were conducted with a CAMECA LEAP 5000 XR atom probe (see Fig. 1). The experiments were all performed in laser-assisted mode at a base temperature of 50 K and the peak ratio $^{48}\text{Ti}^{3+}/^{48}\text{Ti}^{2+}$ was recorded. Before each measurement, a flat test was performed to ensure that no turn-on of the local electrode occurs in the relevant voltage range. For the standard measurement of each specimen with 30 pJ LPE, 250 kHz PR and 1 % DR, 20 million hits were recorded. For the LPE variations, 5 million hits were measured for 2, 5, 10, 30, 50, 100, 150 and 200 pJ LPE each, for PR and DR again 250 kHz and 1 % were selected. For the ion correlation histograms, 20 million total hits were targeted at 200 pJ LPE to achieve sufficient statistics. The AAPs were examined using TiN as the example material. For the measurements with constant field control, a target value of 200 and 300 %/ μm^2 was selected in addition to 30 pJ LPE, 250 kHz PR and 1 % DR. The estimated electric field of the standard measurement of TiN with 39.5 V/nm served as the field estimate. For the measurement with activated auto pulse rate control, the same parameters as for the standard measurement were used and a minimum m/n ratio of 70 Da was selected, as the Ga^+ peak at 69 Da represents the highest occurring peak. To study the auto pulse energy control, the CSRs for $\text{Ti}^{3+}/\text{Ti}^{2+}$ for a target electric field of 38, 39 and 40 V/nm, respectively, were determined using the Kingham curves. The setpoints for the peak ratio $^{48}\text{Ti}^{3+}/^{48}\text{Ti}^{2+}$ were 0.939, 0.434 and 0.217, the range for the LPE was limited to 0.2 to 380 pJ, PR and DR were again 250 kHz and 1 %.

3.4.2. Reconstruction

The reconstruction of the data sets was performed with the “Integrated Visualization and Analysis Software” IVAS within APSuite 6.3 provided by CAMECA Instruments. The reconstruction procedure was conducted in the same manner for all measurements, starting with the analysis of the standing voltage evolution. Care was taken to ensure that the run-in phase at the beginning, which is characterized by a steeply rising standing voltage, was not included in the analysis, as it can be assumed that stable evaporation behavior did not occur there. In addition, the peak ratio history for $^{48}\text{Ti}^{3+}/^{48}\text{Ti}^{2+}$ was exported for subsequent estimation of the electric field (see Section 3.5.3). Followed by the selection of the lateral region of interest (ROI), in which the influence of different aperture geometries of different local electrodes is considered. In the next step, a voltage and bowl correction were applied in several iterations to increase the quality of the mass spectrum and to correct the deviations caused by the fact that the detector is a 2D projection of a 3D hemisphere. The final correction was performed by linear stretching of

the mass spectrum towards known peaks, also known as mass calibration. Where visible in the mass spectra, the peaks at 6 Da - $^{12}\text{C}^{2+}$, 14 Da - $^{14}\text{N}^+$, 24 Da - $^{48}\text{Ti}^{2+}$ and 69 Da - $^{69}\text{Ga}^+$ were used for this purpose. In the next step, the peaks were assigned to the respective ion species. As described in Section 2.4, symmetrical ranging was applied to ensure comparability despite different thermal conductivities of the specimens. All ion species, which were identified and assigned in the mass spectra within this work, the observed charge states as well as the corresponding peak positions can be found in Table 7 in the appendix. As preparation for the peak decomposition, the overlapping peaks of TiC^{2+} with TiN^{2+} at 30.0, 30.5 and 31.0 Da were ranged as the latter in the mass spectra of all TiCN samples. The peaks at 14 and 15 Da were assigned to N^+ and not to N_2^{2+} due to the missing $(^{14}\text{N}^{15}\text{N})^{2+}$ peak at 14.5 Da and the observed field strengths <60 V/nm which are necessary to double ionize N_2 [23]. The peak at 24 Da was fully attributed to $^{48}\text{Ti}^{2+}$. At this position an overlap with C_2^+ cannot be ruled out, but based on isotopic ratios, the contribution of the latter seems negligible. Also C_4^{2+} potentially overlaps with $^{48}\text{Ti}^{2+}$, but due to the reported metastability of C_n^{2+} molecules (for $n = 2, 4, 6\dots$) it is considered to be unlikely [29]. In the last step, the parameters for the reconstruction were set. The detection efficiency of a LEAP 5000 XR is specified as 52 %, the image compression factor and k factor were set to 1.65 and 3.3, respectively. The prevailing electric field was estimated for each reconstruction from the peak ratio history for $^{48}\text{Ti}^{3+}/^{48}\text{Ti}^{2+}$ using the Kingham curves. The radius evolution is based on the voltage evolution. Together with the electric field and the k factor, the initial tip radius is defined via the initial voltage. The corresponding EPOS (i.e. extended position) files of all reconstructions were also exported for data post-processing purposes.

3.5. Atom probe tomography data post-processing

3.5.1. Peak decomposition and composition correction

For all reconstructions of TiCN specimens, peak decomposition was performed as described in Section 2.4. A customized Python (3.9) script was developed for this purpose, which made it possible to automatically correct the bulk composition based on the mass spectrum. As can be seen in Fig. 16, the peaks for TiC^{2+} , TiN^{2+} and overlaps of those were ranged first. The overlaps were decomposed accordingly, using two independent calculation approaches based on the natural isotopic ratios. The results were reviewed and, if necessary, refined by iterating with an adjusted range. The elemental compositions obtained by the reconstructions were imported and accordingly corrected. Since the overlapped peaks were previously ranged as TiN^{2+} during reconstruction, only decomposed TiC^{2+} counts had to be added and the TiN^{2+} counts of the respective peaks had to be subtracted from the preliminary elemental composition. In addition, the overlap of TiC^{2+} with the single isotope element Co at 29.5 Da was corrected.

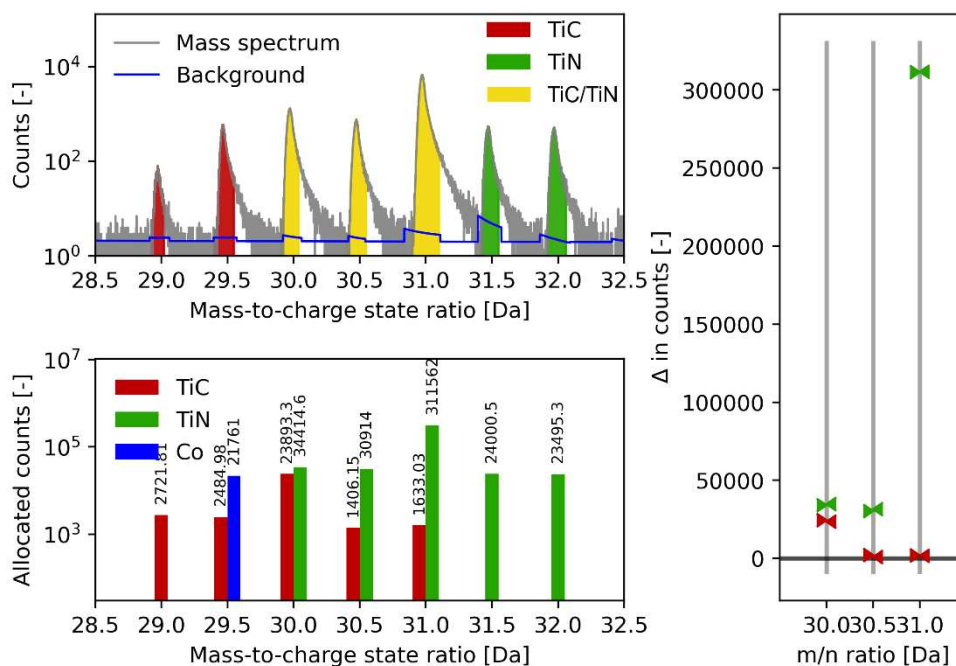


Fig. 16: Exemplary visualization of the peak decomposition for $\text{TiC}_{0.61}\text{N}_{0.39}$ (30 pJ LPE). At the top left, the section of the mass spectrum with the peaks of TiC (red) and TiN (green) as well as those that overlap (yellow) is shown. At the bottom left, the outcome of the decomposition including the correction of Co counts (blue) and on the right a comparison of the results from the two independent calculation approaches based on TiC (arrows on the left) and TiN (arrows on the right) are shown.

3.5.2. Ion pile-up analysis

Customized software was developed to investigate the occurrence of ion pile-up for different ion species. The abundance patterns for Ti^{3+} , Ti^{2+} , C^+ , C_3^{2+} , N^+ and N_2^+ have been investigated. For this purpose, the counts of all occurring isotopes of an ion species of the same charge in the mass spectrum were summed and the apparent isotopic abundances were calculated. Of particular interest here is the deviation from the natural isotopic ratios presented in the evaluations, exemplarily shown for $\text{TiC}_{0.61}\text{N}_{0.39}$ measured with 2 pJ LPE in Fig. 17. The natural isotopic abundances for Ti, C and N can be found in Table 1 (Section 2.4) and for C_3 and N_2 in the following Table 6. The evaluation of C-containing ion species was omitted for TiN. Due to the peak overlap in the mass spectrum of molecular N_2 , consisting of ^{14}N and ^{15}N with $^{46}\text{Ti}^{12}\text{C}$ at 29.0 Da, no meaningful statements can be made about the deviation of the isotope ratios of N_2 in the C-containing specimens. A further peak overlap can be observed in all mass spectra, $^{50}\text{Ti}^{2+}$ overlaps with $^{48}\text{Ti}^{1}\text{H}_2^{2+}$ at 25.0 Da. Since ^{50}Ti is a minor isotope, a correction by peak decomposition was not performed, therefore an incorrect elevated abundance was observed in all evaluations. It should be explicitly mentioned at this point, that this study only qualitatively investigated the occurrence of ion pile-ups and did not include a statistical correction thereof.

Table 6: Natural isotope pattern of C_3^{2+} and N_2^+ , based on the natural isotopic abundance of carbon and nitrogen.

Isotope	Mass [amu]	Abundance [-]	m/n [Da]
C_3^{2+} ($n=2$)			
$(^{12}\text{C}^{12}\text{C}^{12}\text{C})^{2+}$	36.000	0.9671	18.000
$(^{12}\text{C}^{12}\text{C}^{13}\text{C})^{2+}$	37.003	0.0314	18.502
$(^{12}\text{C}^{13}\text{C}^{13}\text{C})^{2+}$	38.006	0.0003	19.003
$(^{13}\text{C}^{13}\text{C}^{13}\text{C})^{2+}$	39.009	< 0.0001	19.505
N_2^+ ($n=1$)			
$(^{14}\text{N}^{14}\text{N})^+$	28.006	0.9927	28.006
$(^{14}\text{N}^{15}\text{N})^+$	29.003	0.0073	29.003
$(^{15}\text{N}^{15}\text{N})^+$	30.000	< 0.0001	30.000

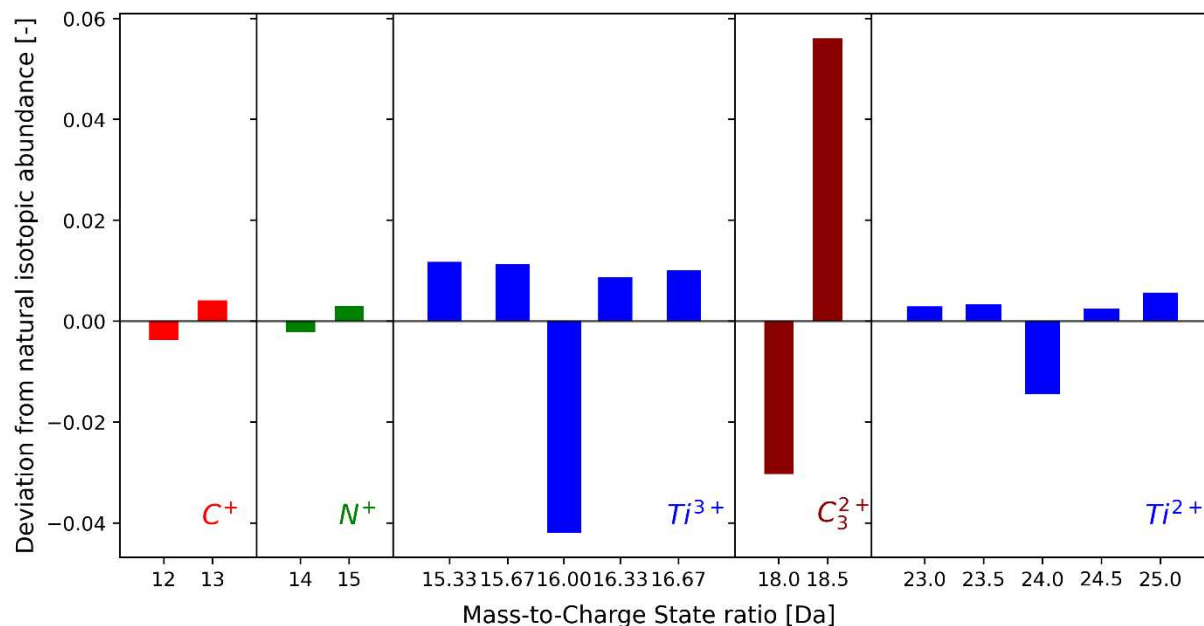


Fig. 17: Deviations from the natural isotope abundances using $TiC_{0.61}N_{0.39}$ (2 pJ LPE) as an example. In all investigated isotopic patterns, the major isotope is underestimated, an indication for the occurrence of ion-pile up.

3.5.3. Electric field strength estimation

For the electric field estimation, the original Kingham curves (Fig. 6) were digitized using the WebPlotDigitizer (4.6) software [78]. Fig. 18 shows them in linear representation. Particularly for shares of charge states close to 100 %, the de-logarithmization resulted in large deviations, which were corrected by the smaller values of the complementary charge state using the condition that the percentages must always add up to 100 %.

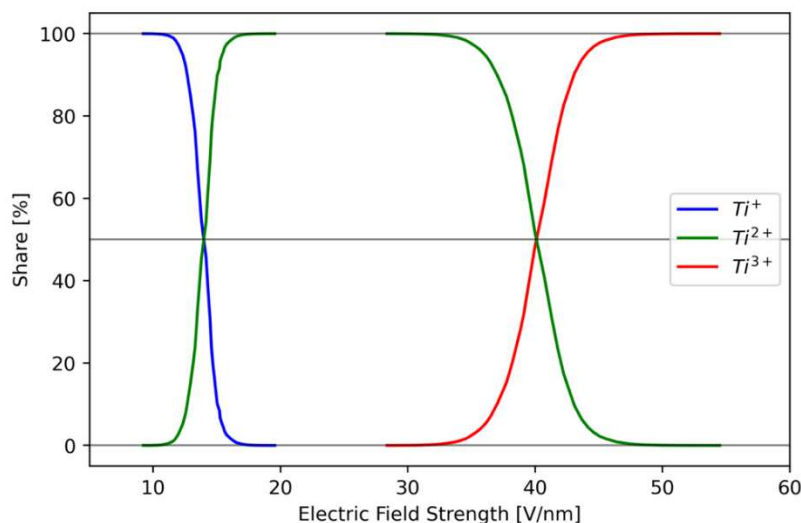


Fig. 18: The linearized and corrected Kingham curves for Ti.

Two different approaches based on the Kingham curves were used for the electric field estimation: On the one hand, the mean values of the peak ratio $^{48}\text{Ti}^{3+}/^{48}\text{Ti}^{2+}$, which were recorded during the measurements, were used. On the other hand, global considerations of the entire reconstructions were conducted, as shown exemplarily in Fig. 19 to determine the total counts of the different Ti charge states and thus, the $\text{Ti}^{3+}/\text{Ti}^{2+}$ CSRs. With this information, the effective electric field strengths at the apex of the specimens were estimated for all reconstructions analyzed. In addition, the spatial distributions of the $\text{Ti}^{3+}/\text{Ti}^{2+}$ CSR across the apex in x-y plane were evaluated for low (2 pJ), moderate (30 pJ) as well as high (200 pJ) LPE each. For this purpose, the datasets were sliced into voxels with a cross-sectional size of $1 \times 1 \text{ mm}^2$ in the x-y detector plane.

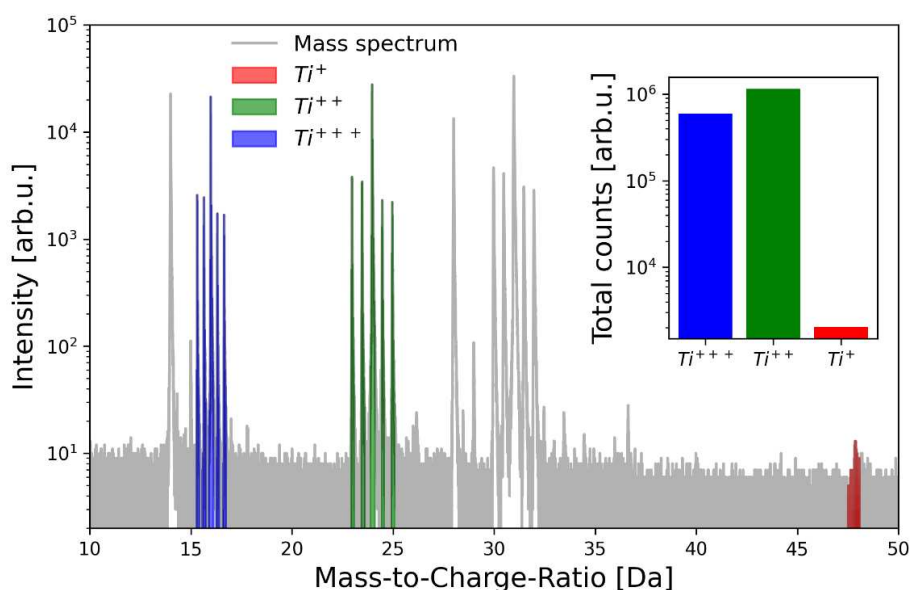


Fig. 19: Mass spectrum of TiN (30 pJ LPE), the Ti peaks are marked with different colors. The bar chart shows the total counts of the three Ti charge states used for the field estimation.

3.5.4. Detection event filtering

A further Python (3.9) script was developed and used to determine the proportion of multiple detection events in each reconstruction. The information was taken from the corresponding EPOS files, which contain the number of hits per pulse. A primary distinction is made between single detection events (one hit) and multiple detection events (at least two hits). So-called partial hits, hits that do not meet all quality requirements (i.e. more than one time stamp is missing), cannot be identified based on the EPOS file. In a further step, the multiple detection events with two or three hits were used to obtain ion correlation histograms. All possible permutations for ion pairs were considered and plotted in the histograms, which also results in the mirroring of the data points around the first median.

4. Results and discussion

4.1. TiN

The standard measurement for TiN with ~20 million evaluated hits resulted in an elemental composition of 51.7 at.% Ti and 48.3 at.% N. The contribution of all impurities was <0.1 at.%. In addition to Ga from the preparation, Cl could also be detected, which is commonly observed in CVD coatings stemming from the utilized precursors [79]. Compared to the ToF-ERDA/RBS measurements, this indicates a lack of compositional accuracy in the form of an N underestimation of 2.3 at.%. With 59.0 %, the proportion of multiple detection events is high. The electric field averaged 39.3 V/nm, which is in good agreement with a recently published work [24] for TiN, taking the conversion factor of ~10 into account for the LPE of a 532 nm – green laser of a LEAP 3000X HR atom probe [7]. Predominant compositional biases are analyzed within the following LPE variation, the results for the elemental composition as a function of LPE are shown in Fig. 20. The N deviation from the ToF-ERDA/RBS measurement increases from 1.6 at.% (2 pJ) up to 3.5 at.% (200 pJ), whereby the elemental composition hardly changes at low LPEs. It can therefore be assumed that at least two compositional biases occur, which explain both, the constant deviations at low LPEs and the increasing deviation with increasing LPE. These will be illuminated in the following by comprehensive analysis.

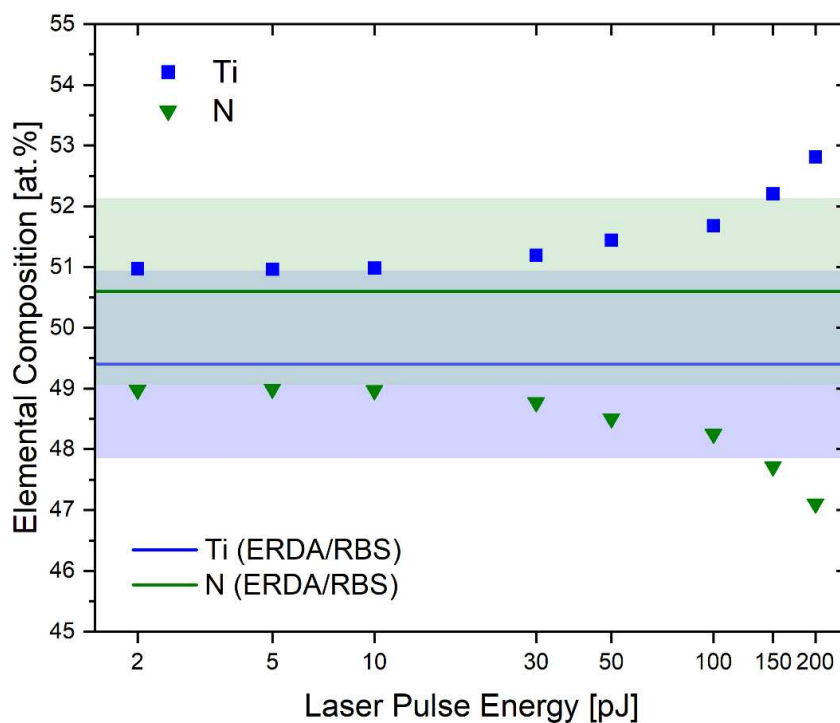


Fig. 20: Results for the elemental composition of TiN as a function of the LPE. The ToF-ERDA/RBS measurement provides the reference composition, the shaded areas mark the corresponding uncertainties thereof.

The ion pile-up analysis for TiN, shown graphically in Fig. 21a, clearly indicates that Ti ions in particular are affected by pile-ups, since the major isotopes apparently exhibit a lower isotopic abundance. As the LPE increases, the deviation of the apparent isotopic abundance from the natural abundance decreases. This can be attributed to the lower evaporation field of Ti. The standing voltage is higher at low LPEs and very close to the evaporation limit, which means that preferred evaporation or even DC evaporation is likely to occur. In this case a loss of N ions appears due to preferential retention, thus causing the underestimation of N at low LPEs. A further indicator that supports a lack of information due to ion pile-ups is the evolution of multiple detection events, shown in Fig. 21b. In particular at low LPEs, their proportion is very high, decreasing significantly from 69.5 (2 pJ) to 45 % (200 pJ) with increasing LPE. The electric field strength estimates, shown in Fig. 21c, reveal a reduction from 39.5 V/nm (2 pJ) to 38.7 V/nm (200 pJ) with increasing LPE. Thus, the UV laser has a significantly lower influence on the reduction of the electric field compared to a green laser [24].

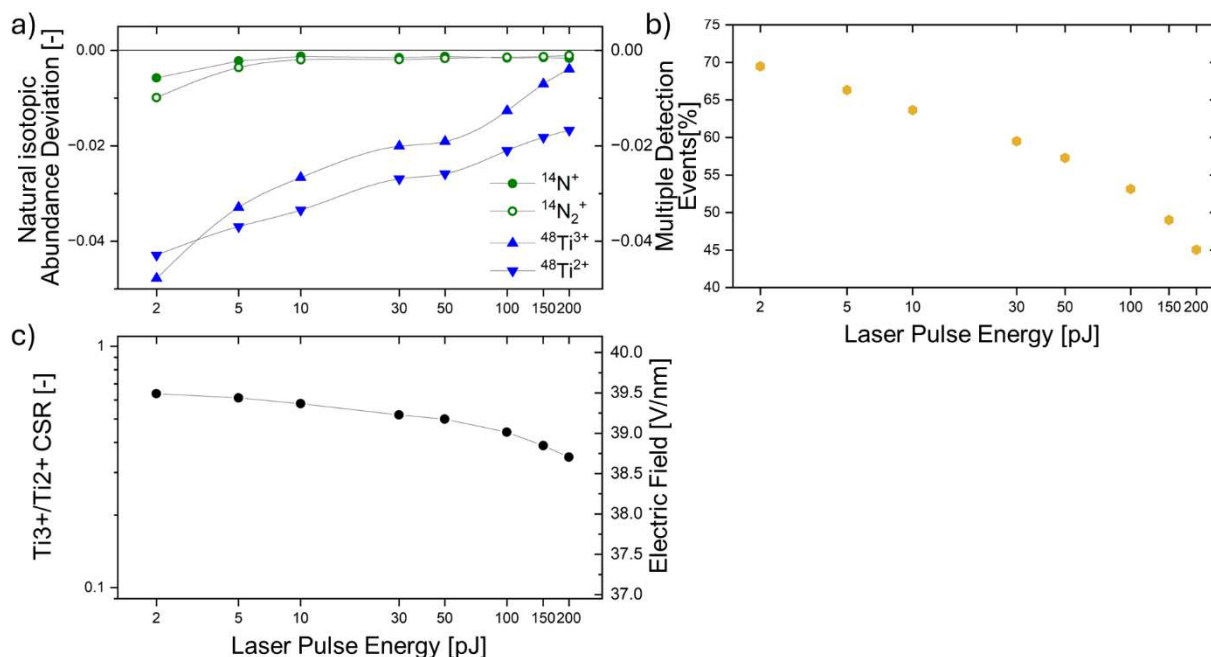


Fig. 21: (a) Ion pile-up analysis for the major isotopes, (b) proportion of multiple detection events and (c) electric field strength estimations as a function of LPE for TiN.

Nevertheless, the laser incidence has an influence on the local distribution of the electric field, as the evaluations in Fig. 22a-c show. A higher Ti^{3+}/Ti^{2+} CSR corresponds to a higher electric field. For the low LPE (2 pJ, Fig. 22a), a high and uniformly distributed field can be observed. For the moderate LPE (30 pJ, Fig. 22b), it is especially the crystallographic information that can be extracted, since elevated electric fields (a CSR of ~ 0.8 corresponds to 39.8 V/nm) are observed for the poles and zone axes. A shadow effect occurs applying a high LPE (200 pJ). As can be seen in Fig. 22c, the electric field is significantly reduced on the side of the laser irradiation compared to the opposite side, thus revealing an asymmetrical field strength distribution. The low Ti^{3+}/Ti^{2+} CSR of ~ 0.2 on the side irradiated by the laser corresponds to an electric field of only 37.9 V/nm.

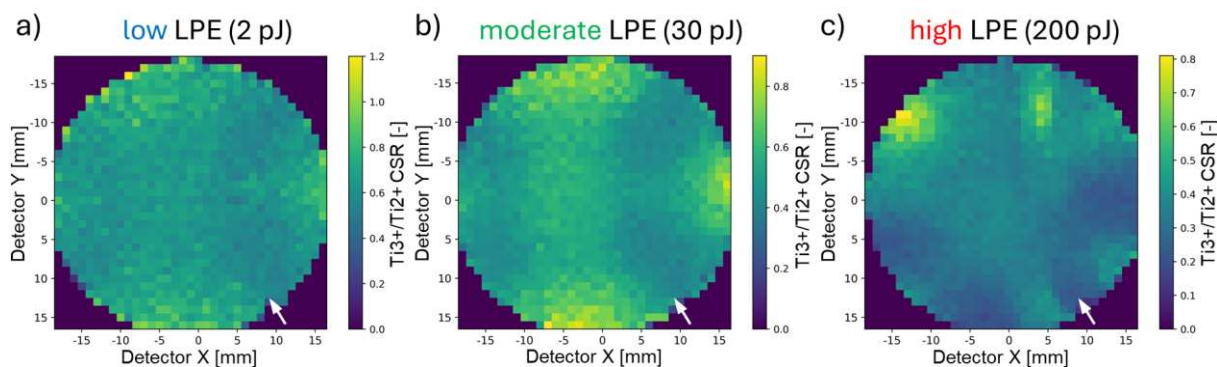


Fig. 22: Spatial distribution of the Ti^{3+}/Ti^{2+} CSR across the apex surface applying a (a) low, (b) moderate and (c) high LPE in the measurements of TiN. The surface area of the evaluated voxels is $1 \times 1 \text{ mm}^2$ in the x-y detector plane. The white arrows mark the direction of the laser.

In the mass spectra for the reconstructions with 50 pJ LPE and higher, the occurrence of the complex molecular ion Ti_2N^{3+} was observed. Due to extreme LPE, the generation of complex molecular ions is favored [33]. The higher the LPE, the more pronounced and intense the peaks became, which is attributed to insufficient electric field strengths. From the elemental accuracy point of view, the increasing occurrence of Ti_2N is unfavorable as it results in further underestimation of the N content. It can therefore be assumed, that the generation of Ti_2N is responsible for the rapidly increasing discrepancy between the observed and reference composition starting at 50 pJ LPE (see Fig. 21). The appearance of complex molecular ions can also be an indication of dissociation phenomena. Therefore, an ion correlation histogram was prepared from the multiple detection events of a measurement with 200 pJ and ~ 20 million hits. This is shown in Fig.

23 and features one track with a negative slope. The intersection with the first median at 36.7 Da corresponds to the parent molecule Ti_2N^{3+} , the tracks go in the direction of the intersections {24, 62} Da and {62, 24} Da, the daughters Ti^{2+} and TiN^+ . This allowed the dissociation of $\text{Ti}_2\text{N}^{3+} \rightarrow \text{Ti}^{2+} + \text{TiN}^+$ to be visualized and verified. Due to the reflectron, the tracks end well before the intersection point, small deviations in the kinetic energy are compensated and result in condensed intersection points [28]. $\text{Ti}_2\text{N}_2^{2+}$, another complex molecular ion, was observed in the mass spectra of the measurements with 150 and 200 pJ LPE. It is likely that dissociation also enables the generation of undetectable neutrals, which represents another compositional bias.

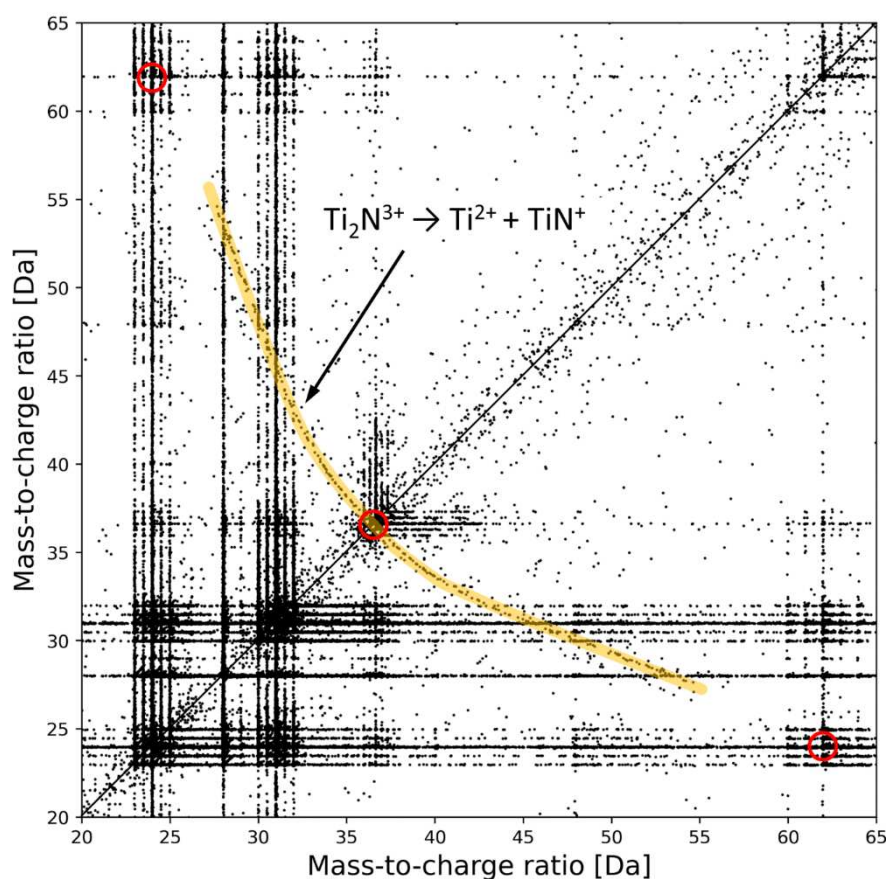


Fig. 23: Ion correlation histogram for TiN (200 pJ), where the dissociation track is highlighted in orange and intersections of parent and daughter molecules are marked with red circles.

A main focus of this thesis is the investigation of AAP and their effects on the measurement and compositional accuracy. Figs. 24a-d show the evaluations for the following analyses of the AAP constant field control. As explained in detail in section 2.8.1, the stress on the specimen is very high, especially at the beginning of the measurement due to the small tip radius. The key metric here is the AER, which normalizes the DR to the surface. The AER can be calculated as a function of the apparent tip radius, using the standing voltage and the k factor. The k factor used in the calculations was assumed to be 5.3, which corresponds to a remote electrode [33]. For the reference measurement with a constant DR of 1 %, an AER of $\sim 750 \text{ \%}/\mu\text{m}^2$ is observed at the beginning of the measurement (Fig. 24a), such high values might in the worst case be responsible for specimen failure. The $1/R^2$ proportionality of the AER is clearly recognizable. Fig. 24b shows fluctuations in the elemental composition within the measurement, comparing the entire data set with the first and last five million hits. The discrepancy to the composition of the standard measurement is maximal at the beginning of the measurement and decreases towards the end. As the evaluations of the two measurements with constant field control at 200 and 300 $\text{ \%}/\mu\text{m}^2$ in Figs. 24c-d show, the DR can be significantly reduced during the run-in phase of the measurement. The target DR varied between 0.15 and 0.75 % and 0.5 and 1.3 %, respectively and exhibited its R^2 proportionality. The compositional accuracy achieved with 200 $\text{ \%}/\mu\text{m}^2$ hardly differs from that of the standard measurement, which can most probably be related to the low DR at the beginning, which led to an increased background level ($\sim 40 \text{ ppm/ns}$). However, the increasing DR with ongoing measurement ensures improved efficiency, in particular for 300 $\text{ \%}/\mu\text{m}^2$, by reducing the acquisition time and simultaneously improving compositional accuracy.

As the standing voltage increases, the ToF of the ions becomes shorter, due to their higher velocities, as explained in detail in section 2.8.2. This fact is used in AAP auto pulse rate control to increase efficiency by shortening the acquisition time. It is known from the standard measurement that the Ga^+ peak at 69 Da is the highest occurring m/n ratio in the mass spectrum. Based on this, a measurement was conducted with enabled auto pulse rate control and a target value of 70 Da. The PR ranged between 250 and 357 kHz. The acquisition time for 20 million hits was 1:51 h. The obtained elemental composition of 51.7 at.% Ti and 48.3 at.% N is identical with that of the reference measurement. However, the standard measurement required 2:31 h, 40 minutes longer, for the same amount of 20 million hits. Due to the non-linear relationship, a considerable time saving potential for the acquisition time can be expected, especially for longer measurements, while maintaining the same data quality.

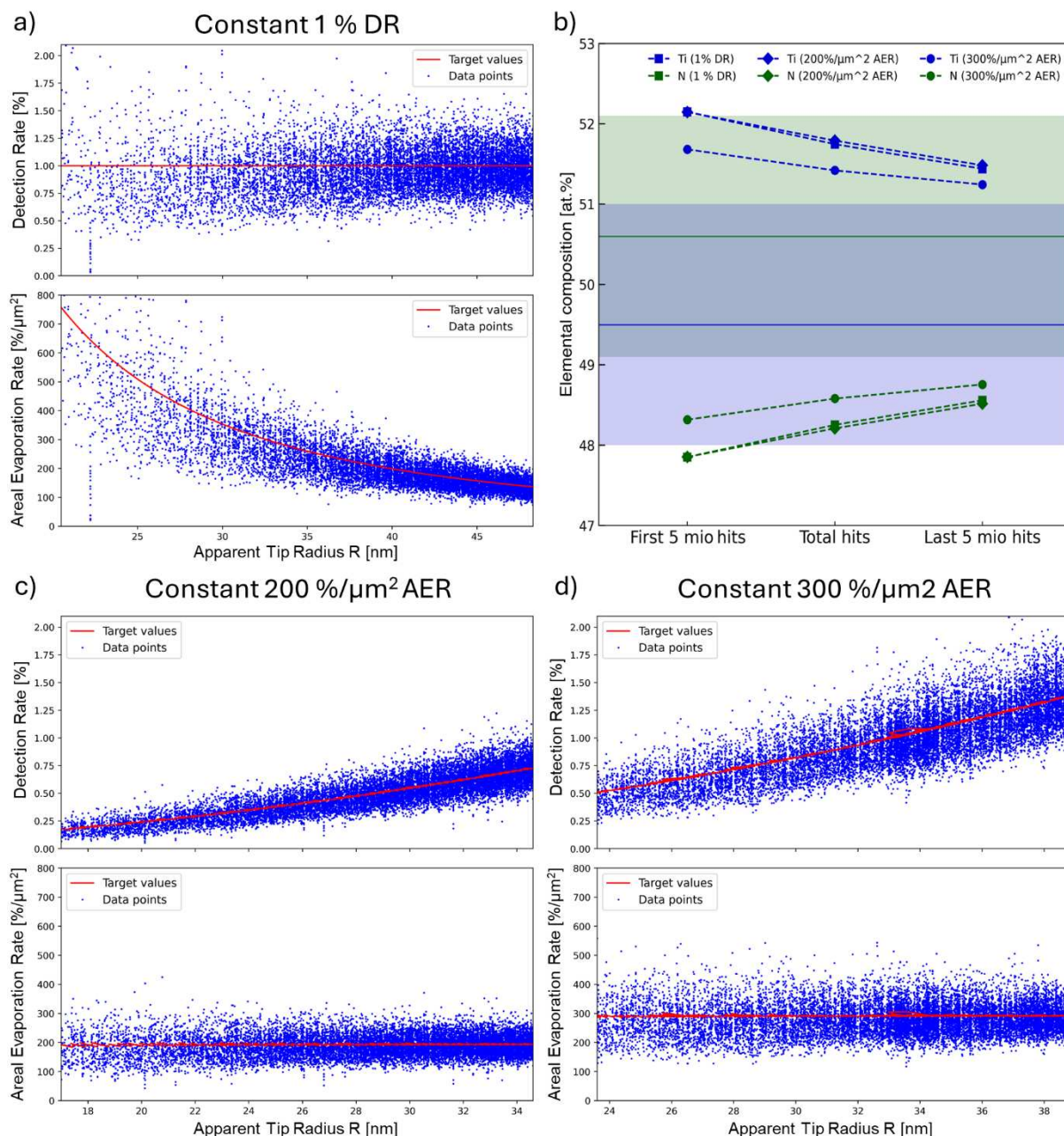


Fig. 24: AER analysis maintaining a (a) constant DR of 1%. (b) Comparison of the elemental composition of all hits with the first and last five million hits of the datasets. Analysis of the AAP constant field control for (a) 200 and (b) 300 %/μm².

With the help of the AAP auto pulse energy control, the optimal LPE for TiN should be found automatically by the instrument. The aim is to find the optimum between too low LPE, accompanied by a high background level and too high LPE, resulting in the generation of complex molecular Ti_2N . However, the attempt to set the peak ratio of Ti_2N to the background level to one failed, most likely because of insufficient statistics due to a lack of counts of the latter. Instead, the ability to specifically set an electric field strength during the measurement was studied. Based on the results of the LPE variation, 38, 39 and 40 V/nm were set via the peak ratios, as described in detail in Section 3.4.1. The evaporation behavior at 38 V/nm was stable, the observed peak ratio $^{48}Ti^{3+}/^{48}Ti^{2+}$ ranged between 0.2 and 0.26, the background level was very low (~ 8 ppm/ns) and the proportion of multiple detection events was relatively modest at 34.0 %. However, it should be noted that the LPE varied between 354 and 368 pJ, which is extremely high and accompanied by excessive Ti_2N peaks in the mass spectrum. For 39 V/nm, the instrument targeted significantly milder values for LPE between 98.5 and 102 pJ. The peak ratio was stable between 0.41 and 0.45, the background level was ~ 10 ppm/ns and the proportion of multiple detection events increased to 55.3 %. This coincides well with the results for 100 pJ from the LPE variation. To achieve 40 V/nm, the LPE had to be reduced to very low values between 0.25 and 0.4 pJ. Stable evaporation behavior could not be achieved as a result. A high background level of >250 ppm/ns and 80.4 % multiple detection events indicate out-of-synch or even dc evaporation. The analyses show that the AAP auto pulse energy control can be used to set specific electric field strengths over a range of several V/nm. This offers great advantages during the data acquisition, such as preventing or at least reducing peak overlaps through targeted setting of expected charge states and thus avoiding elaborate data post-processing.

4.2. $\text{TiC}_{0.25}\text{N}_{0.75}$

The standard measurement for the TiCN specimen with the lowest C content yielded 51.9 at.% Ti, 11.3 at.% C and 36.8 at.% N after peak decomposition, which corresponds to a C/(C+N) ratio of 23.5 %. The overestimation of the Ti content of 2.6 at.% compared to the ToF-ERDA/RBS measurement is reflected in an underestimation of the C and N content of 1.5 and 1.1 at.%, respectively. The proportion of multiple detection events accounted for 43.0 % of all hits, the electric field amounted to 39.4 V/nm. The LPE variation performed is again intended to shed light on compositional biases that are attributable to the prevailing electric field. Fig. 25 shows the elemental composition in comparison with the reference composition and its uncertainty. Similar to TiN, it can be observed that the inaccuracy of the elemental composition hardly changes for low LPEs. Starting from 50 pJ, a strong increase of the deviation can be observed with increasing LPE. The Ti content increases up to 57.9 at.% (200 pJ) which corresponds to a discrepancy of 8.6 at.%. Whereas the C and N content decreases to 9.2 and 32.9 at.%, respectively.

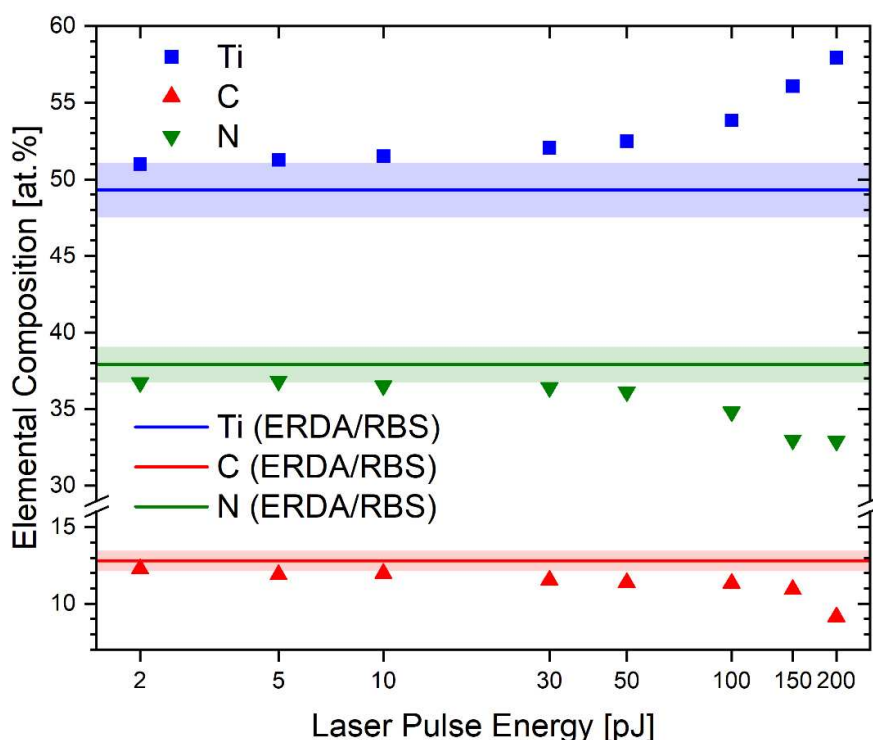


Fig 25: Results for the elemental composition of $\text{TiC}_{0.25}\text{N}_{0.75}$ as a function of the LPE. The ToF-ERDA/RBS measurement provides the reference composition, the shaded areas mark the corresponding uncertainties thereof.

More extensive analyses of the LPE variation show in Fig. 26a that the $C/(C+N)$ ratio hardly changes (25.1 - 24.0 %). C is continuously underestimated even more than N. For 200 pJ, however, it is only 21.8 %, due to the very low C content of only 9.2 at.%. The studies on the presence of ion pile-ups, presented in Fig. 26b, clearly show that molecular C_3^{2+} is affected at any LPE, but most pronounced for 2 pJ and at very high LPEs such as 150 and 200 pJ. This is in very good agreement with the results reported by Thuvander *et al.* in their study for carbides [15], explained by the correlative (co)-evaporation of C-containing ions in groups and the associated selective loss of C due to hardware limitations of the detector. The pile-up of Ti as observed for TiN can also be seen. The results presented in Fig. 26c support this explanation: At 2 pJ the proportion of multiple detection events is 72 %, while by changing the evaporation conditions, this proportion can be reduced to 34.2 % (200 pJ). Nevertheless, the elemental accuracy decreases and indicates ion-pile ups for C^+ and C_3^{2+} for higher LPEs, suggesting that dissociation processes are present in which undetectable neutral fragments are generated or hits are lost as a result of pile-ups. Based on the estimates for the electric field, which are presented in Fig. 26d, the electric field decreases from 40.3 (2 pJ) to 37.8 V/nm (200 pJ) and thus also the probability for re-ionization of neutral fragments decreases.

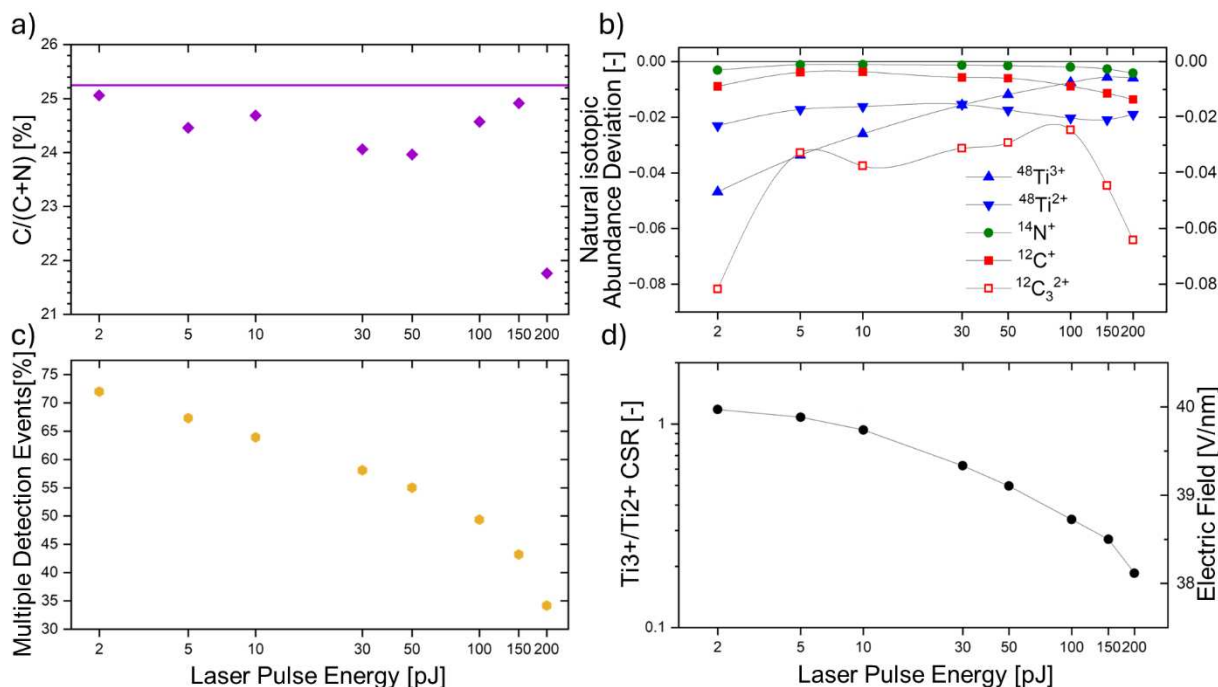


Fig. 26: Apparent $C/(C+N)$ ratio compared to the reference ratio obtained by ToF-ERDA/RBS, (b) Ion pile-up analysis for the major isotopes, (c) proportion of multiple detection events and (d) electric field strength estimations as a function of LPE for $TiC_{0.25}N_{0.75}$.

The spatially resolved distributions of the electric field, shown in Fig. 27a-c, reveal features which are presumably related to crystallographic effects. The field strengths are significantly increased in the vicinity of the pole. However, while the surrounding area exhibits a CSR of ~ 0.75 (39.7 V/nm) at 2 pJ, this declines to ~ 0.10 (36.8 V/nm) at 200 pJ and shows an asymmetrical distribution there.

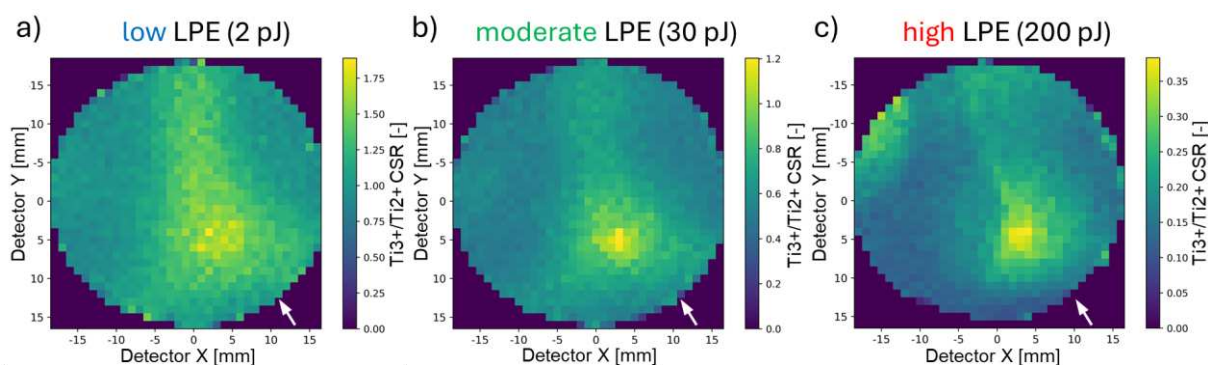


Fig 27: Spatial distribution of the Ti^{3+}/Ti^{2+} CSR across the apex surface applying a (a) low, (b) moderate and (c) high LPE in the measurements of $TiC_{0.25}N_{0.75}$. The surface area of the evaluated voxels is $1 \times 1 \text{ mm}^2$ in the x-y detector plane. The white arrows mark the direction of the laser.

4.3. $TiC_{0.45}N_{0.55}$

The elemental composition of the standard measurement corrected by peak decomposition yielded 54.0 at.% Ti, 18.9 at.% C and 27.1 at.%. This corresponds to an overestimation of Ti of 4.8 at.% and a resulting underestimation for C and N of 3.9 and 0.8 at.%, respectively, based on the ToF-ERDA/RBS results. The imbalance results in a $C/(C+N)$ ratio of 41.1 %. From the 20 million hits evaluated, 60.7 % were multiple detection events. The global consideration of the Ti^{3+}/Ti^{2+} CSR yielded an average electric field of 39.5 V/nm. The results of the LPE variation presented in Fig. 28 show that the elemental accuracy decreases considerably with increasing LPE. The C content in particular deviates from the reference composition as the LPE increases, while an underestimation of N is only observed for higher LPEs. This fact is also reflected in the evolution of the apparent $C/(C+N)$ ratio, as shown in Fig. 29a, which continuously decreases from 45.8 (2 pJ) to 38.0 % (150 pJ), followed by a slight increase to 38.7 % (200 pJ), as the N content is significantly more underestimated.

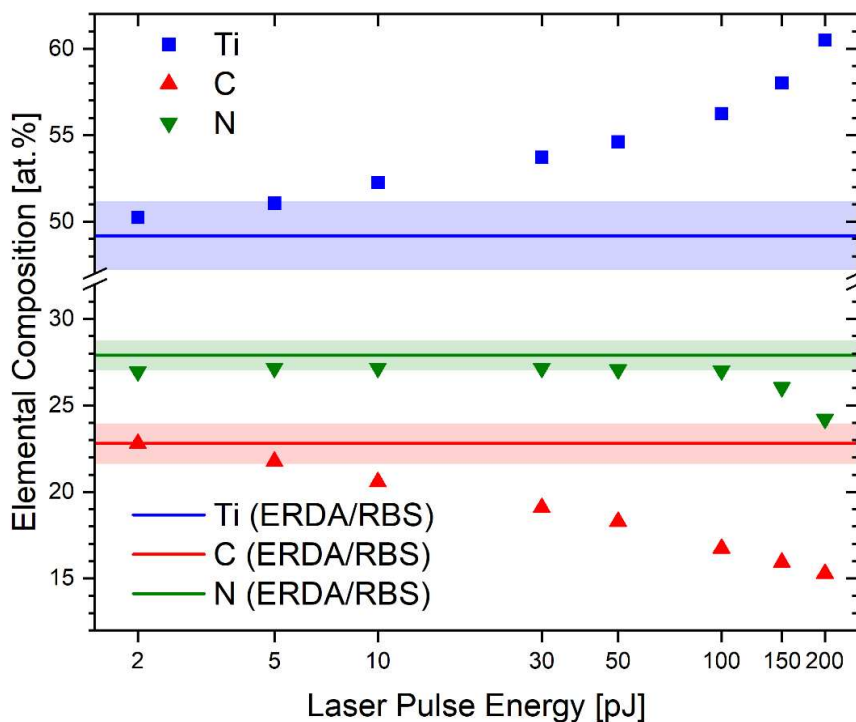


Fig 28: Results for the elemental composition of $TiC_{0.45}N_{0.55}$ as a function of the LPE. The ToF-ERDA/RBS measurement provides the reference composition, the shaded areas mark the corresponding uncertainties thereof.

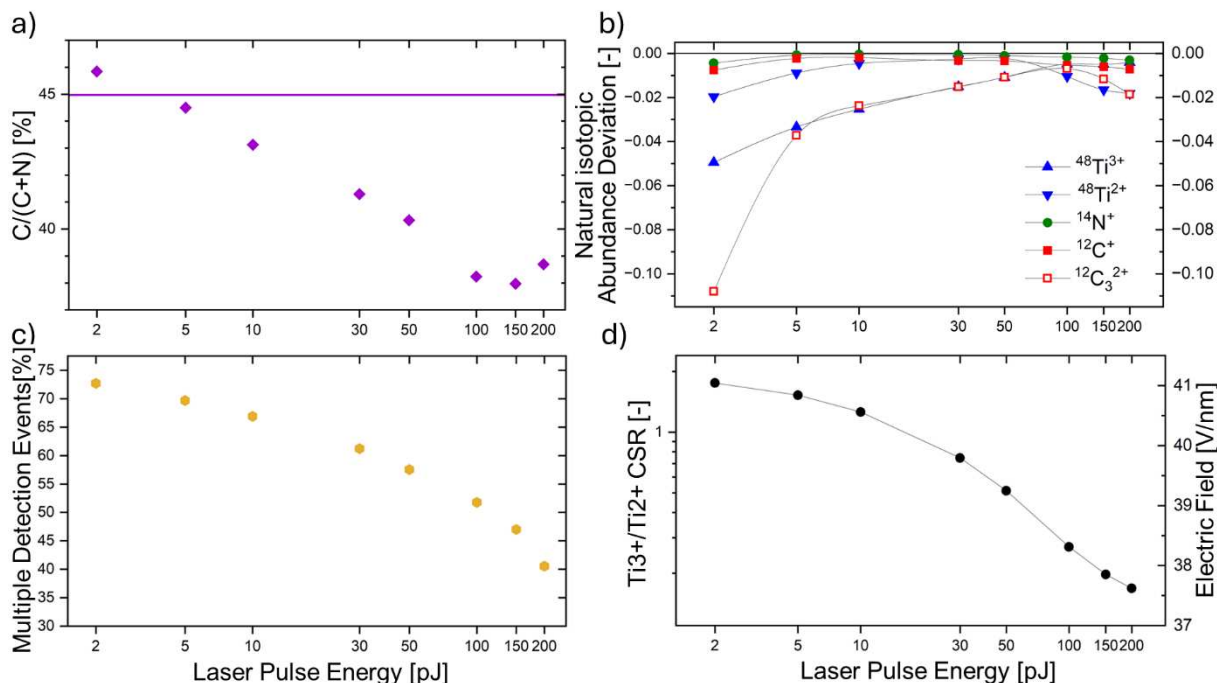


Fig 29: Apparent $C/(C+N)$ ratio compared to the reference ratio obtained by ToF-ERDA/RBS, (b) Ion pile-up analysis for the major isotopes, (c) proportion of multiple detection events and (d) electric field strength estimations as a function of LPE for $TiC_{0.45}N_{0.55}$.

The molecular C_3^{2+} at low LPEs is severely affected by ion pile-up, but also the analyses for the two different Ti charge states reveal a data loss due to the detector limitation, as shown in Fig. 29b. The proportion of multiple detection events decreased again with increasing LPE and ranged between 72.7 and 40.5 %, as depicted in Fig. 29c. The electric field was again considered globally and estimated using Kingham curves, and the corresponding results, presented in Fig. 29d, range from 41 V/nm for 2 pJ down to 37.6 V/nm applying 200 pJ. The spatially resolved field strength distributions for moderate, low and high LPE, presented in Fig. 30a-c, exhibit features most likely related to crystallographic effects (i.e. higher field strengths in poles and zone axes) and indicate the occurrence of a grain boundary in the lower half. The latter is manifested by a lower electric field which is represented by the Ti ions from and around the grain boundary and this therefore appears darker. The electric field strength was significantly lowered, in the area of the pole: at 2 pJ it was still 41.6 V/nm (corresponding to a Ti^{3+}/Ti^{2+} CSR of 3.5), at 30 pJ it was reduced to 40.8 V/nm (1.75) and reached a minimum at 200 pJ of 37.9 V/nm (0.16). The occurrence of complex molecular ions such as C_2N , C_2N_2 or even C_3N , which emerge with decreasing electric field, suggests that phenomena around insufficient field strengths, such as dissociation, cause biases in compositional accuracy.

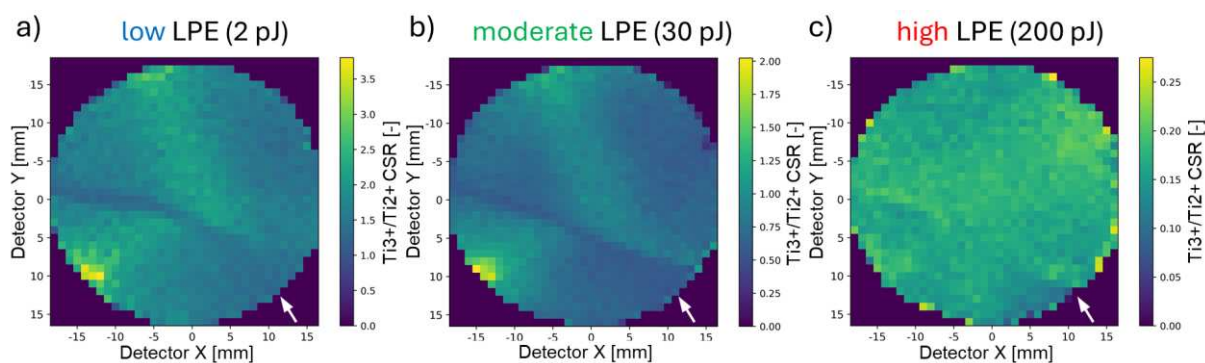


Fig 30: Spatial distribution of the Ti^{3+}/Ti^{2+} CSR across the apex surface, applying a (a) low, (b) moderate and (c) high LPE in the measurements of $TiC_{0.45}N_{0.55}$. The surface area of the evaluated voxels is $1 \times 1 \text{ mm}^2$ in the x-y detector plane. The white arrows mark the direction of the laser.

4.4. $\text{TiC}_{0.61}\text{N}_{0.39}$

In the standard measurement of $\text{TiC}_{0.61}\text{N}_{0.39}$ at 30 pJ, the 20 million hits yielded an elemental composition of 56.2 at.% Ti, 23.3 at.% C and 20.5 at.% N, which corresponds to an apparent C/(C+N) ratio of 53.3 %. This is a severe underestimation of the C content of 6.4 at.%, resulting in an overestimation of Ti and N of 5.1 and 1.3 at.%, respectively. This suggests that the loss of C, caused by compositional biases is significantly more pronounced than that of N, which is also evident from the results of the LPE variation, which are presented in Fig. 31. The lowest discrepancy in C content is 3.2 at.% and was measured at 5 pJ. With increasing LPE, the discrepancy increases continuously and reaches 10.8 at.% at 200 pJ (corresponds to 18.9 at.% C). The N content is robust with an average of 20.3 at.% up to 100 pJ, then N is also underestimated and is only 17.9 at.% at 200 pJ.

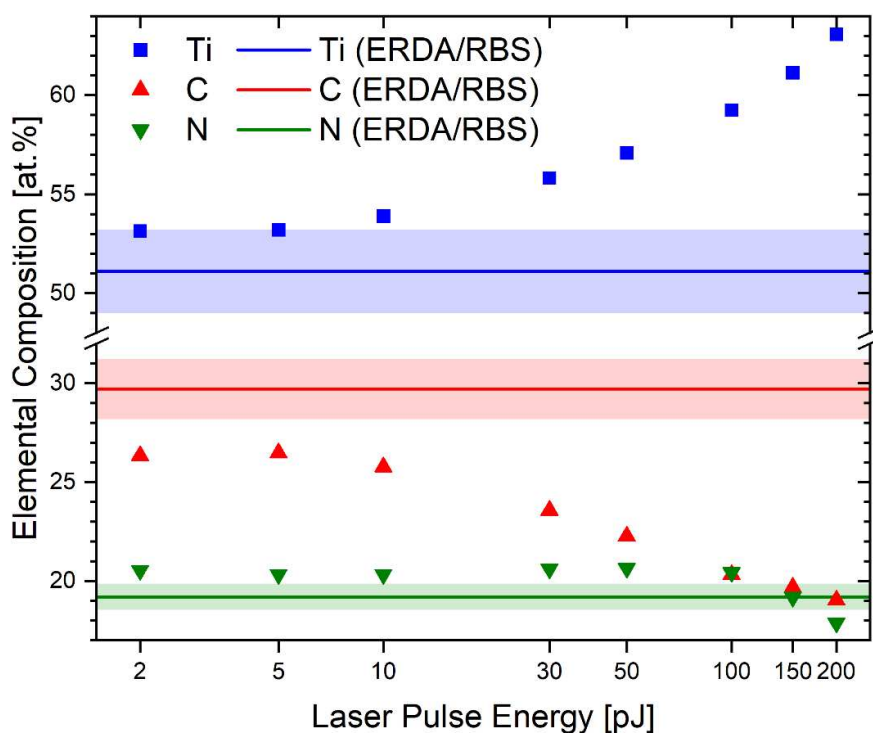


Fig 31: Results for the elemental composition of $\text{TiC}_{0.61}\text{N}_{0.39}$ as a function of the LPE. The ToF-ERDA/RBS measurement provides the reference composition, the shaded areas mark the corresponding uncertainties thereof.

The evolution of the observed $C/(C+N)$ ratio is shown in Fig. 32a. The underestimation of C is significantly stronger and only increases again due to the retarded underestimation of the N content starting at 100 pJ. The analysis of the ion pile-up in Fig. 32b shows that both, Ti CSRs and the molecular C_3^{2+} are primarily affected. However, the loss of information seems to be limited mainly to the latter. An overestimation of the natural abundance from the major isotope of Ti^{2+} can also be observed, although not very pronounced and probably negligible, this can be explained by an overlap of Ti^{2+} with C_2^+ at 24 Da. Although not confirmed within this work, C_2^+ is a possible dissociation product of C_3^{2+} , as shown by Peng *et al.* [30] using a straight flight path instrument. Fig. 32c shows that, as observed for all specimens studied so far, the proportion of multiple detection events decreases progressively with increasing LPE, from 73.9 % (2 pJ) to 35.6 % (200 pJ). The electric field is significantly lowered by the increasing LPE, as Fig. 32d shows. While field strengths above 40 V/nm could be observed for LPEs below 30 pJ, this decreased considerably and amounted to only 36.9 V/nm at the maximum LPE of 200 pJ.

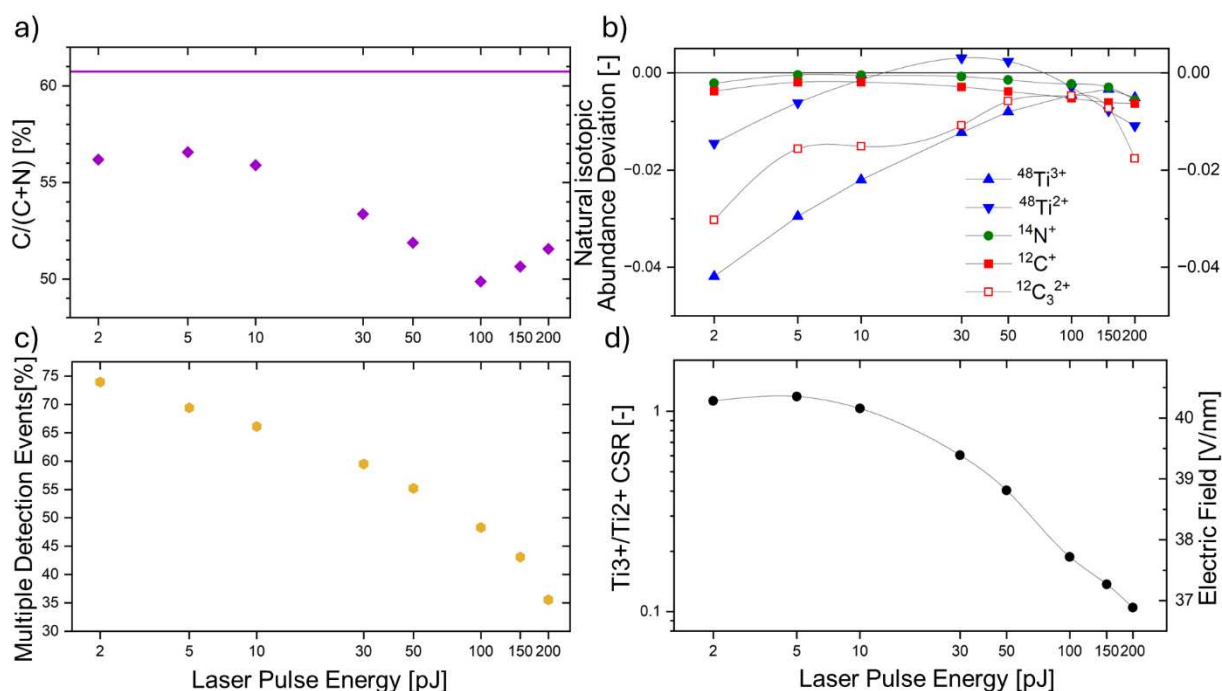


Fig 32: Apparent $C/(C+N)$ ratio compared to the reference ratio obtained by ToF-ERDA/RBS, (b) Ion pile-up analysis for the major isotopes, (c) proportion of multiple detection events and (d) electric field strength estimations as a function of LPE for $TiC_{0.61}N_{0.39}$.

Several features can be observed in the spatially resolved distributions of the Ti^{3+}/Ti^{2+} CSR, which is directly proportional to the electric field, as shown in Fig. 33a-c. In addition to the crystallographic information, which is characterized by increased field strengths in the poles, it appears as if a grain boundary triple junction is visible in which the electric field is diminished. Due to the columnar growth of the coating and the preparation from top, this can be observed starting from the lowest to the highest LPE in the upper third of the detector ROI. Dihedral angles of $\sim 120^\circ$ can be observed in the reconstructions as well as excessive TiC concentrations in the grain boundaries. This can be explained either by the electric field strength or by the segregation of solutes. Zschiesche *et al.* [80] presented a method to quantify the segregation of solutes by APT in order to discuss the influence of segregation at triple junctions on the properties of the entire thin film. A major influence of the laser can be observed particularly at the maximum LPE of 200 pJ. In the incidence area, the Ti^{3+}/Ti^{2+} is approximately 0.03, which corresponds to a field strength of 35.2 V/nm.

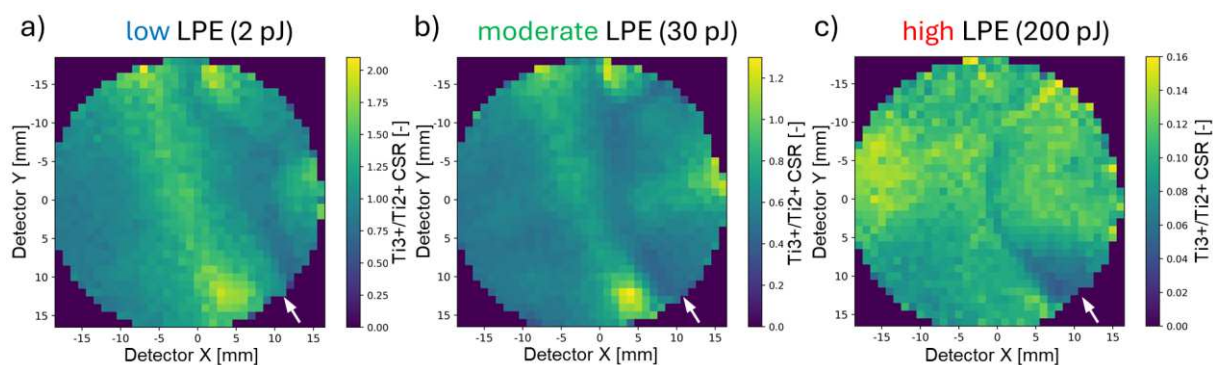


Fig 33: Spatial distribution of the Ti^{3+}/Ti^{2+} CSR across the apex surface applying a (a) low, (b) moderate and (c) high LPE in the measurements of $TiC_{0.61}N_{0.39}$. The surface area of the evaluated voxels is $1 \times 1 \text{ mm}^2$ in the x - y detector plane. The white arrows mark the direction of the laser.

Due to these significantly reduced observed field strengths and the increased occurrence of C-containing complex molecular ions, 20 million hits at 200 pJ were recorded in a further measurement. The multiple detection events of this data set form the basis for the ion correlation histogram shown in Fig. 34a and b. The dissociation tracks for $TiC_3N^{3+} \rightarrow TiC_2N^{2+} + C^+$ (i.e. $\{32.7|32.7\} \text{ Da} \rightarrow \{43|12\} \text{ Da}$) and $TiC_2N^{3+} \rightarrow TiCN^{2+} + C^+$ (i.e. $\{28.7|28.7\} \text{ Da} \rightarrow \{37|12\} \text{ Da}$) are clearly recognizable and suggest that the metastable TiC_3N dissociates stepwise via TiC_2N to $TiCN$, creating single ion C^+ in the process. The most dominant dissociation track is $Ti_2N^{3+} \rightarrow Ti^{2+} + TiN^+$, which is known from the TiN specimen. As shown

in previous studies, C in the form of molecules (e.g. C_2 , C_3 and C_4) tends to dissociate, but cannot be detected with the LEAP 5000 XR due to the reflectron [29,30]. The dissociation of e.g. $C_2^{2+} \rightarrow C^+ + C^+$, is not visible as a track because the intersection of the parent molecule with that of the daughter ions coincides at {12|12} Da. During dissociation, the electrostatic repulsion of the daughter ions results in a kinetic energy release, which is visible in the form of abnormal shoulders before the actual peak in the mass spectrum [30]. However, these small energy differences are also compensated by the reflectron, and are therefore not visible which makes verification of C_2^{2+} dissociation impossible. It can thus be assumed that many more dissociation processes have remained unrecognized and that the resulting fragments may be lost in ion pile-ups or even form neutrals.

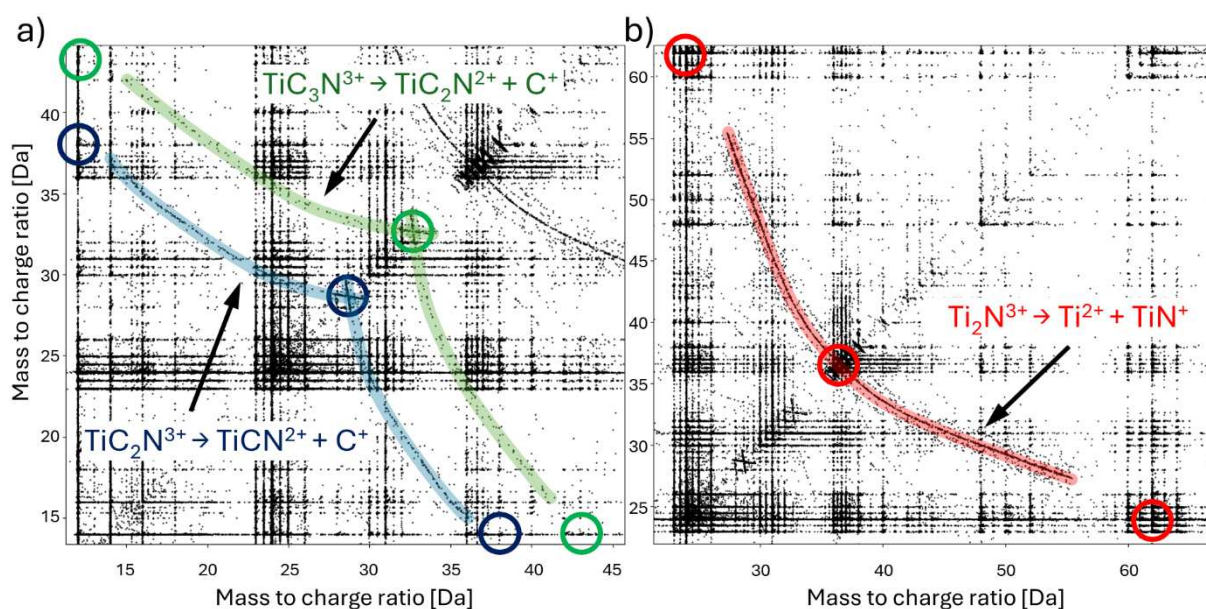


Fig 34: Details of the ion correlation histogram for $TiC_{0.61}N_{0.39}$, where (a) two dissociation tracks with C contribution and (b) the from TiN known dissociation are highlighted in color. Corresponding intersections of parent and daughter molecules are marked with circles.

4.5. $\text{TiC}_{0.78}\text{N}_{0.22}$

For the TiCN specimen with the highest C content, an elemental composition of 57.7 at.% Ti, 29.6 at.% C and 12.7 at.% N was determined in the standard measurement and corresponds to a C/(C+N) ratio of 69.9 %. This composition represents an overestimation of the Ti and N content of 8.6 and 1.5 at.%, respectively, and an underestimation of 10.1 at.% of the C content compared to ToF-ERDA/RBS. The proportion of multiple detection events was 57.0 %, the average electric field 39.2 V/nm. The results of the LPE variation, which can be seen in Fig. 35, show that the highest elemental accuracy was achieved with an LPE of 5 pJ. The Ti content was overestimated by 4.1 at.% and the C and N content were underestimated by 3.9 and 0.2 at.%, respectively. With increasing LPE, the elemental accuracy decreases and the discrepancy to the ToF-ERDA/RBS reference value increases further. Ti and C contents balance each other, since N content is relatively stable between 11.0 and 12.6 at.%. At 200 pJ LPE, the deviation from the reference measurement is most pronounced with 63.9 at.% Ti, 25.0 at.% C and 11.2 at.% N.

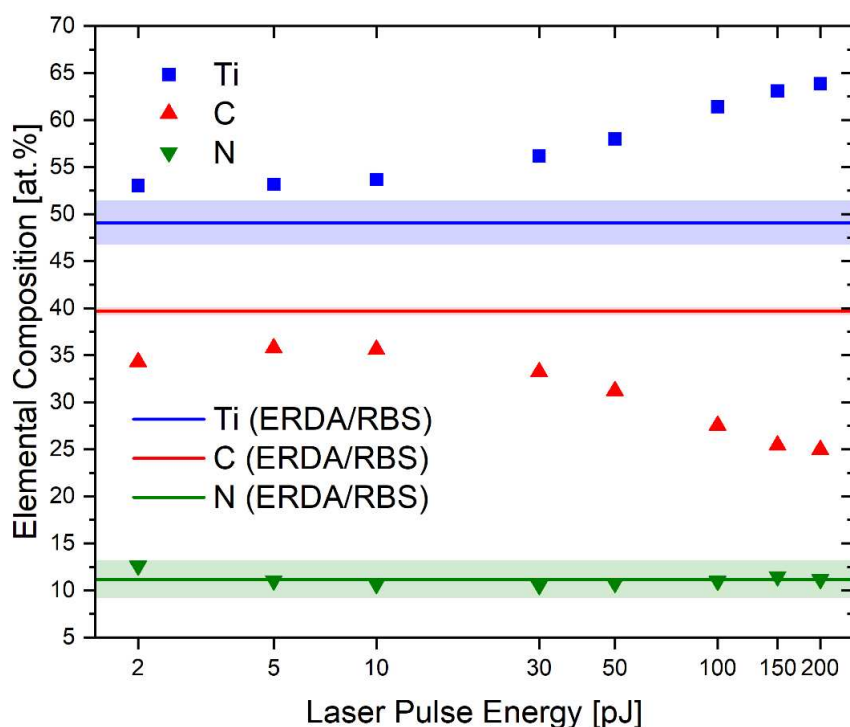


Fig. 35: Results for the elemental composition of $\text{TiC}_{0.78}\text{N}_{0.22}$ as a function of the LPE. The ToF-ERDA/RBS measurement provides the reference composition, the shaded areas mark the corresponding uncertainties thereof.

At 10 pJ, a C/(C+N) ratio of 77.0 % was achieved, which corresponds to a deviation of only 1 % from that of the reference composition. For lower and higher LPEs, the ratio deviates significantly more, due to the lower observed C content, as can be seen in Fig. 36a. At 2 pJ, all ion species investigated are affected by ion pile-ups, in particular C_3^{2+} and the two Ti charge states Ti^{2+} and Ti^{3+} , as illustrated in detail in Fig. 36b. The higher the LPE, the lower the deviation of the major isotopes from their natural abundance and thus the possible loss of data. The major isotope of Ti^{2+} achieves positive deviations at LPEs >30 pJ, traceable to the increased occurrence of $(^{12}C^{12}C)^+$ and its overlap with $^{48}Ti^{2+}$. For $^{12}C^+$ no significant deviation occurs that requires an elaborate correction, as often described in the literature [25,26]. As can be seen in Fig. 36c, the proportion of multiple detection events decreases continuously with increasing LPE from 71.1 to 37.3 %. The same applies for the electric field strength, presented in Fig. 36d. The evaluated Ti^{3+}/Ti^{2+} ratios report a relatively high field strength of 40.2 V/nm for 2 and 5 pJ, followed by a strong reduction down to 36.5 V/nm at 200 pJ.

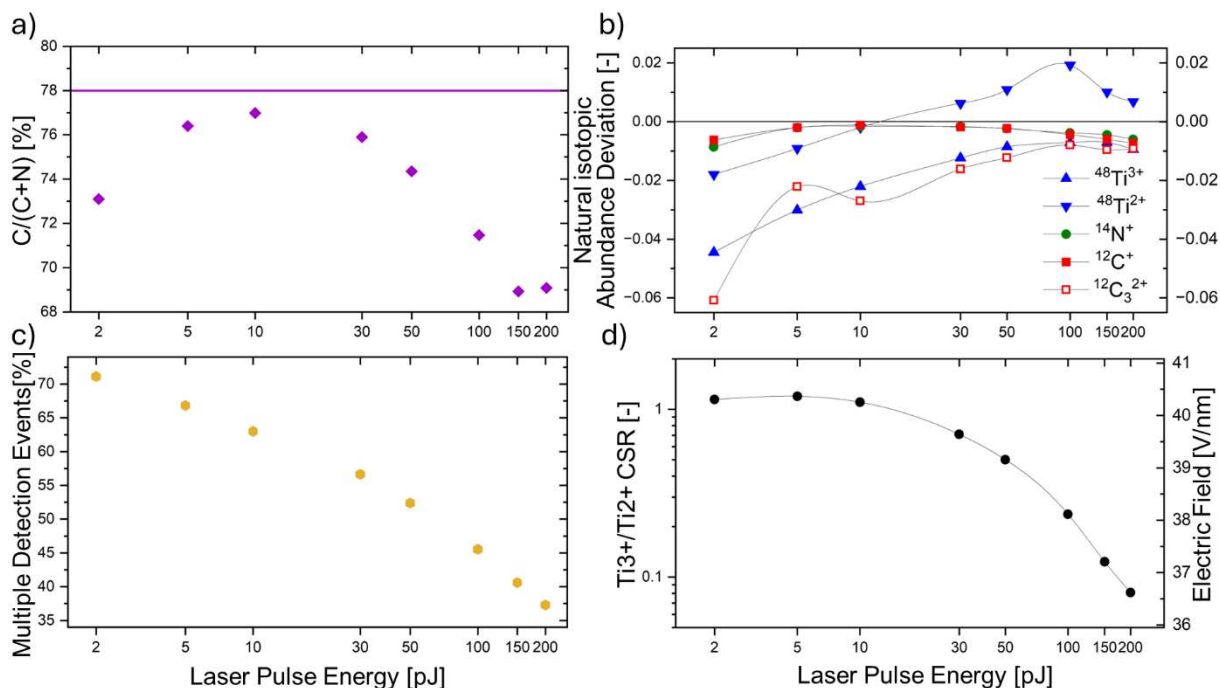


Fig. 36: Apparent C/(C+N) ratio compared to the reference ratio obtained by ToF-ERDA/RBS, (b) Ion pile-up analysis for the major isotopes, (c) proportion of multiple detection events and (d) electric field strength estimations as a function of LPE for $TiC_{0.78}N_{0.22}$.

The analysis of the spatially resolved distribution of the electric field strength, as shown in Fig. 37a-c for the measurements with 2, 30 and 200 pJ LPE, reveals special features. Contrary to previous analyses, no pronounced shadow effects due to the laser could be observed, thus the electric field is uniformly reduced with increasing LPE. While the evaluation of the low 2 pJ does not provide any conclusive correlations, the distribution at moderate 30 pJ reveals exceptional insights into the crystallographic structure of the specimen. Several poles and zone axes can be observed, especially one pole stands out with a high electric field of ~ 41.1 V/nm ($\text{Ti}^{3+}/\text{Ti}^{2+}$ CSR ~ 2.1). The sixfold symmetry of the weaker poles around the main pole suggests an $\langle 111 \rangle$ orientation of the investigated $\text{TiC}_{0.78}\text{N}_{0.22}$ specimen. The analysis of the measurement with 200 pJ shows only the main pole, due to the severely reduced field and possible surface migration due to thermal input, most of the crystallographic information seems to have been lost here.

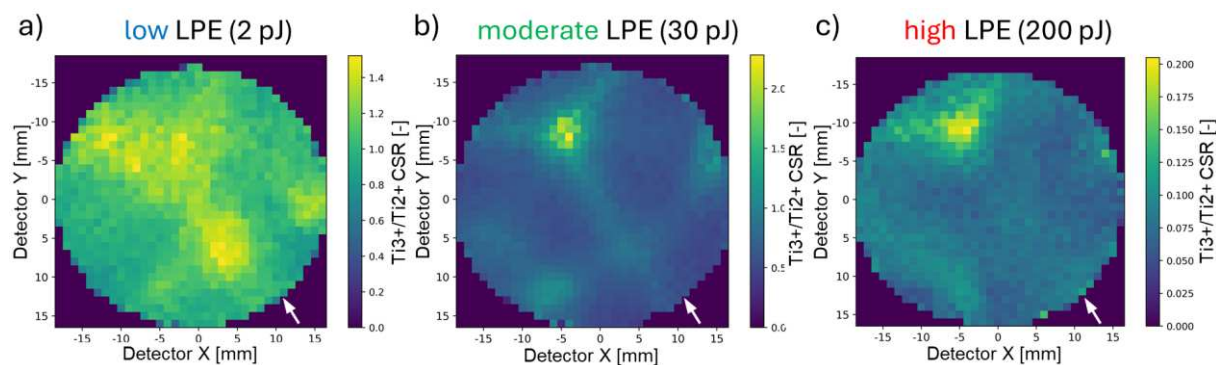


Fig. 37: Spatial distribution of the $\text{Ti}^{3+}/\text{Ti}^{2+}$ CSR across the apex surface applying a (a) low, (b) moderate and (c) high LPE in the measurements of $\text{TiC}_{0.78}\text{N}_{0.22}$. The surface area of the evaluated voxels is $1 \times 1 \text{ mm}^2$ in the x-y detector plane. The white arrows mark the direction of the laser.

4.6. TiC

For the binary TiC, the standard measurement yielded an elemental composition of 60.9 at.% Ti and 39.1 at.% C. This means that the Ti content is overestimated by 11.5 at.% and the N content is correspondingly underestimated. The ToF-ERDA/RBS measurement confirmed an increased Cl content (~ 0.6 at.%) in the specimen observed by APT. This is most likely due to the different deposition parameters and feed gas mixture for the synthesis of TiC. For improved comparability with the other specimens examined within this study, only the Ti and C content was therefore used. The measurements for the LPE variation at 2, 5 and 10 pJ could not be carried out as the specimens always fractured at this low LPEs. The results in Fig. 38 show, that the highest elemental accuracy was achieved applying 30 pJ LPE. The composition of 69.7 at.% Ti and 30.3 at.% C achieved with the maximum LPE of 200 pJ, peaks at a deviation from the reference composition of 20.3 at.%.

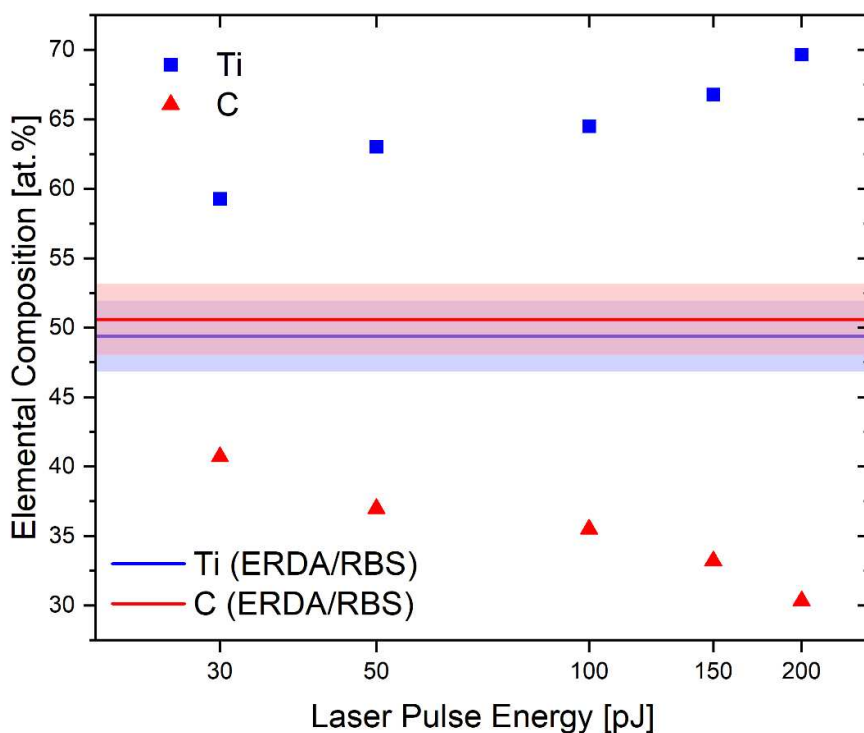


Fig. 38: Results for the elemental composition of TiC as a function of the LPE. The ToF-ERDA/RBS measurement provides the reference composition, the shaded areas mark the corresponding uncertainties thereof.

As can be seen from Fig. 39a, C_3^{2+} and Ti^{3+} are affected by ion pile-ups with increasing LPE, which is probably due to dissociation processes. The abundance of the major isotope of Ti^{2+} is always overestimated, which can be explained by the occurrence of C_2^+ and the overlap of the $(^{12}C^{12}C)^+$ peak with that of $^{48}Ti^{2+}$ at 24 Da. The proportion of multiple detection events decreases from 52.4 % (30 pJ) to 30.7 % (200 pJ) when the LPE is increased, as shown in Fig. 39b. An increase in the LPE also results in a strong reduction in the electric field, which averages 39.6 V/nm at 30 pJ, while it is reduced to 34.1 V/nm when 200 pJ are applied, as illustrated in Fig. 39c.

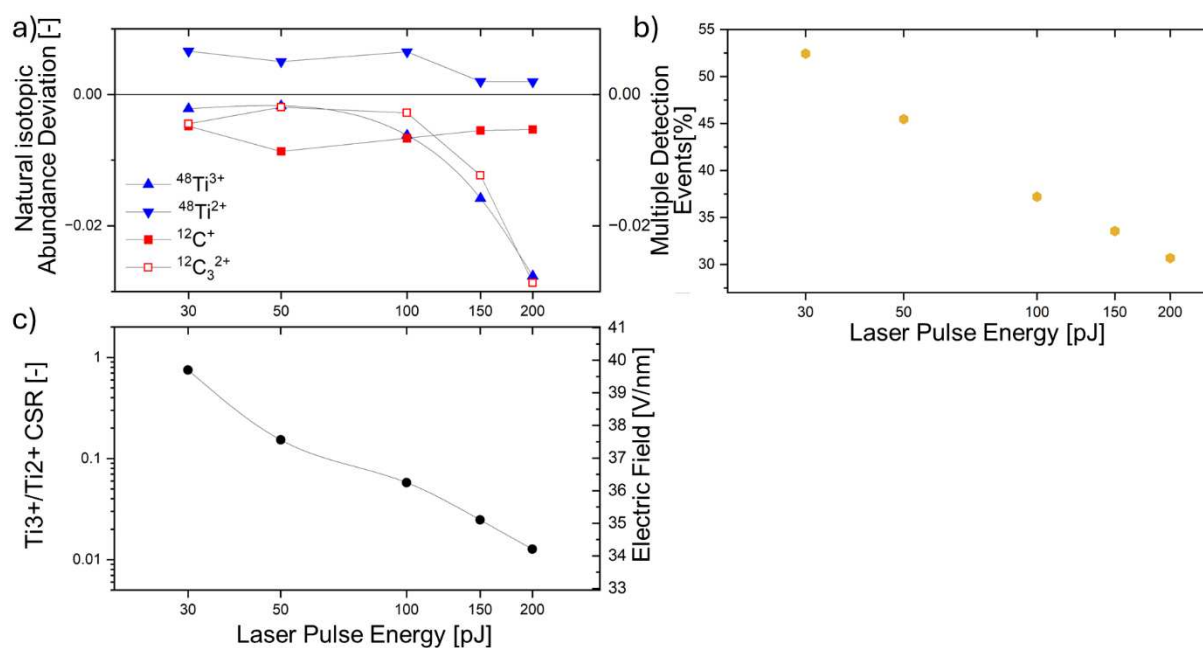


Fig. 39: (a) Ion pile-up analysis for the major isotopes, (b) proportion of multiple detection events and (c) electric field strength estimations as a function of LPE for TiC.

Fig. 40a and c show the spatially resolved distributions of the electric field strength for 30 and 200 pJ. In the former, the crystallographic information of the specimen can be analyzed. The fourfold symmetry around the pole in the center, which is characterized by a relatively high field of 39.6 V/nm (corresponds to Ti^{3+}/Ti^{2+} CSR = 0.7), suggests a $\langle 100 \rangle$ orientation. This is also evident from the 2D concentration map of TiC in Fig. 40b, which exhibits symmetric features. At 200 pJ, the electric field is considerably reduced, the main pole is still recognizable, but the distribution exhibits no further features.

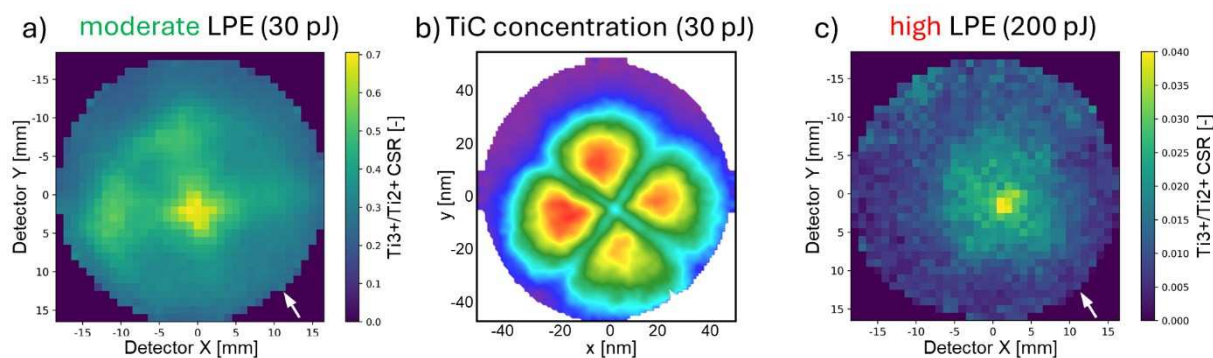


Fig. 40: Spatial distribution of the Ti^{3+}/Ti^{2+} CSR across the apex surface applying a (a) moderate and (c) high LPE in the measurements of TiC. The surface area of the evaluated voxels is $1 \times 1 \text{ mm}^2$ in the x - y detector plane. The white arrows mark the direction of the laser. (b) The 2D concentration map of molecular TiC along the z axis from the measurement with moderate LPE.

Due to the limitations of the reflectron, which were extensively discussed in the evaluation of $TiC_{0.61}N_{0.39}$ (see section 4.4.), an ion correlation histogram for TiC was omitted. Instead, similar to the work of Meisenkothen *et al.* [61], an analysis of the detector dead zone and dead time was carried out. For this purpose, all multiple detection events consisting of two and three hits from the measurement with 200 pJ were used. The relative positions of ion pairs in all possible permutations within a multiple detection event (i.e. 3-multiple detection event: 1-2, 2-3, 3-1) with a ToF difference $< 2.5 \text{ ns}$ were considered. As can be seen in Fig. 41a, this results in a detector dead zone in which no information is available due to ion pile-ups with more than one missing time stamp per hit. In comparison with the study carried out on a LEAP 4000X Si straight flight path instrument [61], the multi hit detection algorithm is significantly improved. Nevertheless, the dead zones along the delay lines of the detector can also be recognized in this work. The increased density in the center of Fig. 41a is clearly visible, which is synonymous for small distances between hits within the multiple detection events. It can be assumed that this is due to co-evaporation of groups from adjacent sites or caused by dissociation processes of molecular ions during the flight, which is in good agreement with the findings described by Thuvander *et al.* [25]. More detailed insights are provided by the corresponding mass spectrum in Fig. 41b, where all observed peaks can be seen in the range between 1 and 25 Da. The peaks at 6 and 12 Da are C^{2+} and C^+ , respectively. Peaks caused by the ^{13}C isotope are not visible, due to the low probability of an ion pile-up caused by two ions from the same isotope with very low abundance (^{13}C : 1.07 %). The peak family between 23 and 25 Da indicates Ti^{2+} due to the characteristic peak ratios. An overlap at 24 Da with C^{2+} cannot be ruled out, but could not be confirmed by isotopic

abundance due to a lack of statistics. Based on the results, it cannot be determined whether the pile-ups are stemming from co-evaporation or dissociation. At 200 pJ, the electric field was very low at 34.1 V/nm and the mass spectrum nonetheless shows no peaks of complex molecular ions. Hence, it can be concluded that primarily products of dissociation processes lead to a loss of information due to ion pile-ups.

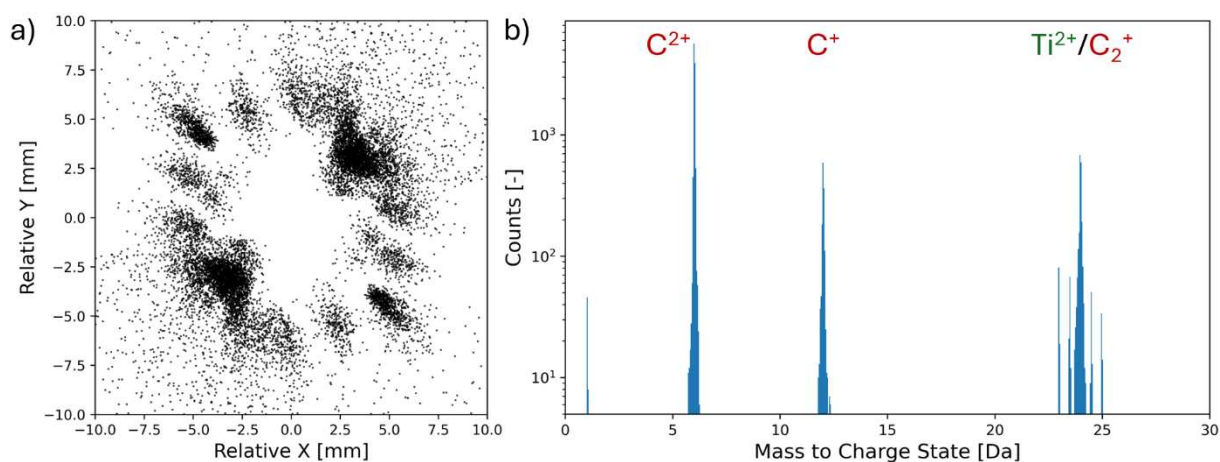


Fig. 41: (a) Detector dead zone visualized by plotting relative positions of 2- and 3-multiple detection events with a ToF difference <2.5 ns. (b) The mass spectrum of the hits shown in (a).

4.7. Trends within the Ti(C,N) coating system

Hereinafter, the gained insights of all investigated specimens are compared and prevailing trends within the Ti(C,N) coating system are discussed. Representative for the elemental accuracy, the deviations of the observed Ti contents from the ToF-ERDA/RBS reference composition are compared and shown in Fig. 42, as the Ti content is independent of the C/N ratio at ~50 at.% in all specimens. Two trends can be seen here: (I) The steady deviation at low LPEs increases with increasing C content, which is mainly attributed to the tendency of carbides to evaporate in groups from adjacent sites, resulting in ion pile-ups. And (II), the rapidly increasing discrepancy that occurs at higher LPEs. This seems to be more pronounced and to start at lower LPEs, the higher the C content is. This is probably due to dissociation, which mainly involves C-containing molecules which's fragments are associated with ion pile-ups.

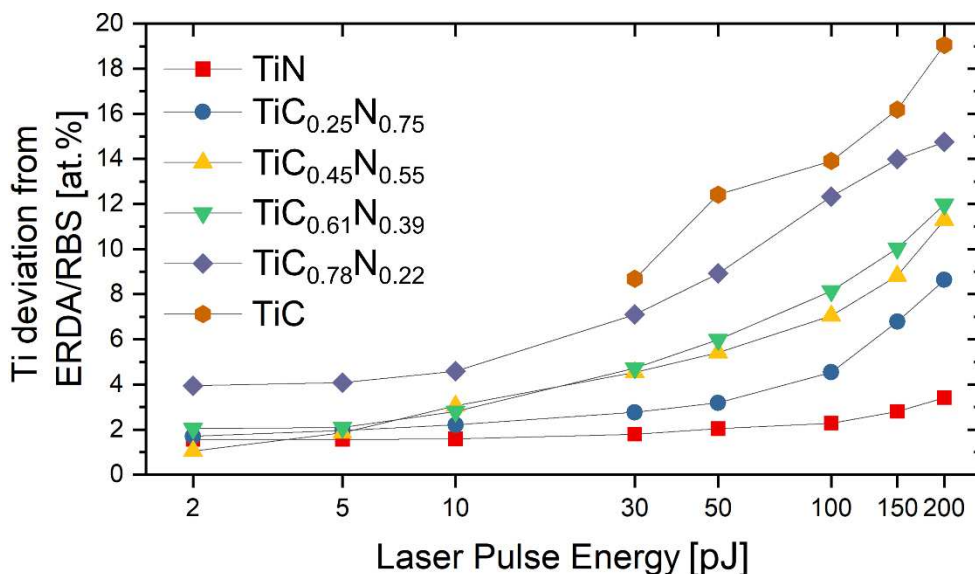


Fig 42: Deviations of the Ti content from the ToF-ERDA/RBS reference across the Ti(C,N) coating system as a function of the applied LPE.

The composition of the non-metallic components can be described with the C/(C+N) ratio. In Fig. 43, the discrepancy to the respective C/(C+N) ratio, which is determined by the mean values of the ToF-ERDA/RBS reference composition, is shown for all TiCN specimens as a function of the LPE. This clearly shows that the higher the C content in the specimen, the higher the underestimation of the ratio. The same applies to an increase in LPE, which is more critical for the C content than for the N content. From the results for the Ti content and for the C/(C+N) ratio, the smallest deviations from the ToF-ERDA/RBS results can be observed for LPEs between 5 and 10 pJ. In order to achieve the highest possible elemental accuracy when measuring Ti(C,N), an LPE in this order of magnitude is thus recommended.

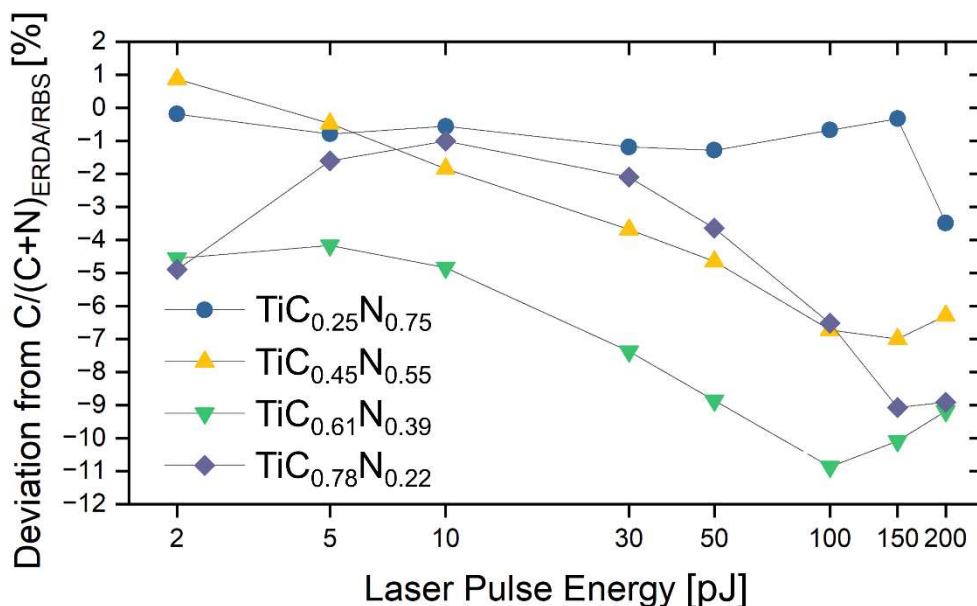


Fig. 43: Deviations of the observed $C/(C+N)$ ratios from the ToF-ERDA/RBS reference as a function of the applied LPE of the TiCN specimens investigated within this work.

To explain the observed discrepancies in elemental composition, comprehensive analyses were carried out for each specimen. In particular, the loss of information due to ion pile-up phenomena was investigated by determining the deviations of the major isotope from its natural isotopic abundance of different ion species. A higher loss is characterized by a stronger underestimation, but again it should be noted that the evaluation only allows qualitative statements and no corrections were made in the course of this work. Fig. 44 shows ion pile-up trends across the Ti(C,N) coating system as a function of LPE in the form of heatmaps for the ion species (a) Ti^{3+} , (b) N^+ , (c) C^+ and (d) C_3^+ . TiC is not part of the comparison, due to the incomplete LPE variation. The analysis for Ti^{3+} shows that pile-ups occur at low LPEs, which is mainly due to the lower evaporation field of Ti. The considerably higher standing voltage at lower LPEs significantly increases the probability of co-evaporation. The analyses of N^+ , C^+ and C_3^+ also indicate ion pile-ups at low LPEs, with the latter being the most affected, which is attributed to the tendency for co-evaporation in groups of C. However, there is also a loss of information with increasing LPE, especially if the proportion of the respective species in the specimen is low. A trend that is probably due to the fact that stable evaporation behavior is ensured by the main components and the conditions are therefore not optimal for the element with the lowest content. The wavelength of the laser is likely to have a considerable influence on the nature of the ion pile-ups, since measurements with a green ($\lambda = 532$ nm) laser made a correction of the number of $^{12}C^+$ ions mandatory (^{13}C

correction) [25,26]. In this work, the $^{12}\text{C}^+$ species shows the smallest deviations from the natural isotopic abundance using a UV ($\lambda = 355 \text{ nm}$) laser, hence no correction was performed. From the results it can be concluded that the respective optimal LPE depends not only on the ion species but also on the composition of the specimen.

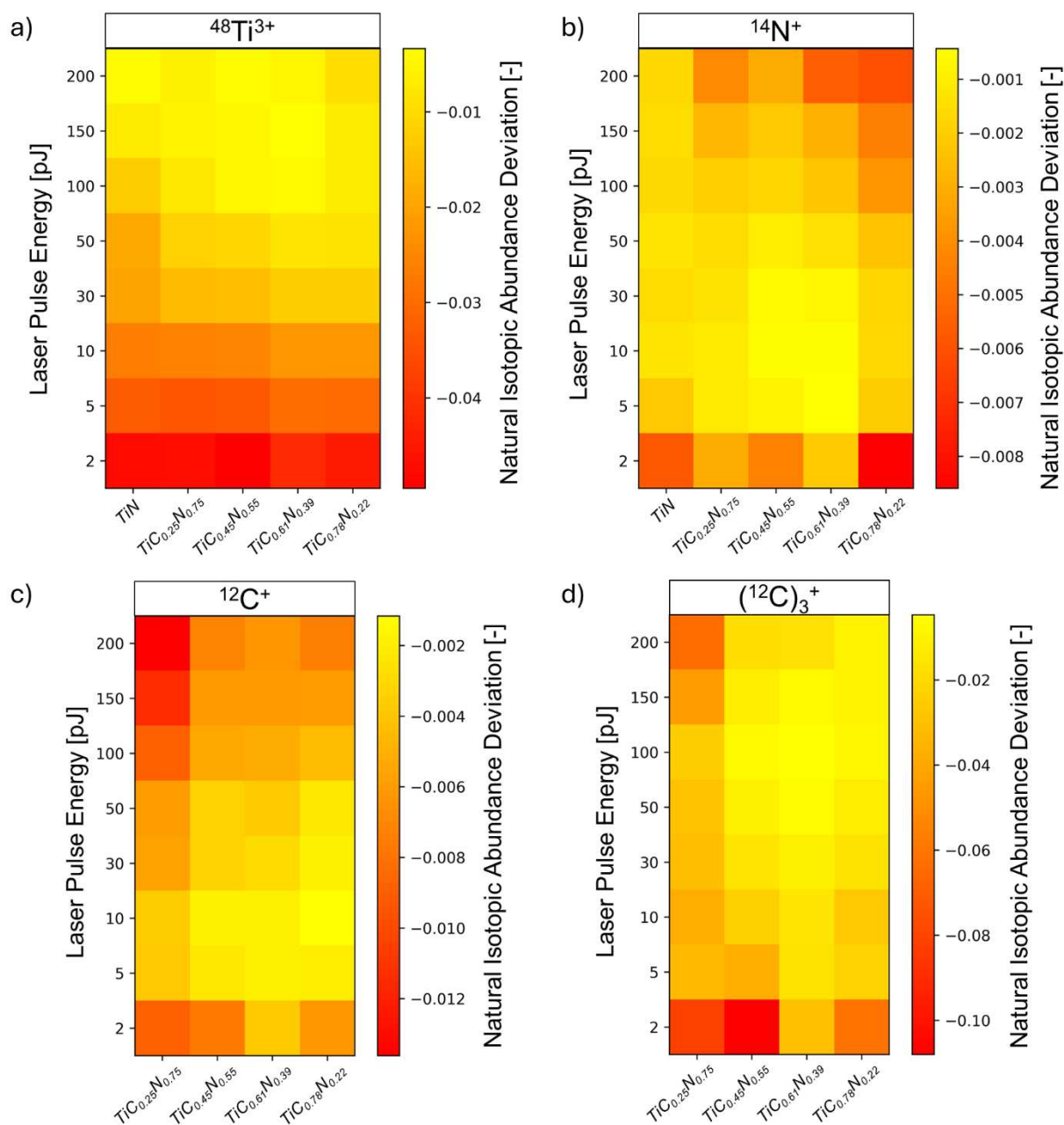


Fig 44: Ion pile-up trends across the Ti(C,N) coating system, revealed by analyzing the deviation from the natural isotopic abundance of the respective major isotopes (a) $^{48}\text{Ti}^{3+}$, (b) $^{14}\text{N}^+$, (c) $^{12}\text{C}^+$ and (d) $(^{12}\text{C})_3^+$.

Fig. 45 shows the evolution of the proportion of multiple detection events in the LPE variations of the various specimens. This clearly shows that the hit characteristics within the Ti(C,N) coating system are similar. At 2 pJ, around 70 % of the hits of all specimens arrive at the detector together with other ions. This proportion decreases as the LPE is increased. A further trend appears to emerge: the higher the C content, the lower the proportion of multiple detection events. The difference between the specimens increases with increasing LPE. For example, TiN at 200 pJ exhibits about 45 % and TiC only 30.7 % multiple detection events. However, together with the results of the ion pile-up analyses, this can probably be attributed to the fact that the increased loss of C-containing ions in multiple detection events causes them to be identified as single detection events. Although dissociation processes that occur at higher LPEs generate daughter ions from singly evaporated molecular ions, which are usually registered as multiple detection events, the similar flight times and close proximity are prone to loss by ion pile-up.

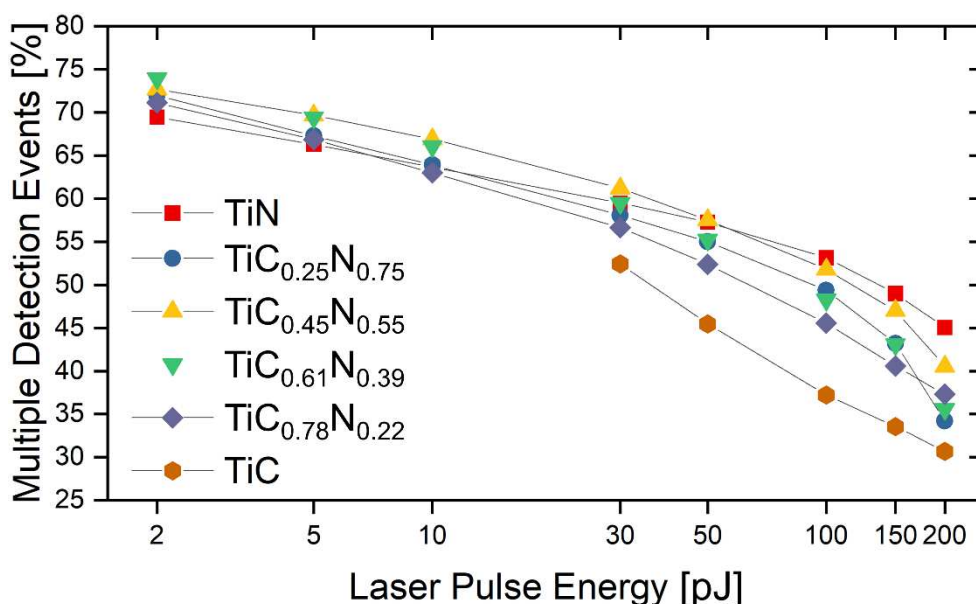


Fig 45: Comparison of the proportions of multiple detection events of the different specimens observed in the LPE variations.

The electric field strengths observed for the LPE variations are compared in Fig. 46. As expected, the electric field decreases with increasing LPE for all specimens, as the local temperature increase at the apex of the specimen is higher due to the higher energy input. The electric field of TiN is very robust in comparison and is subjected to a relatively small reduction at very high LPEs. All the C-containing specimens exhibit a higher electric field than TiN at low LPEs. At 50 pJ LPE it is around 39 V/nm for all specimens, except TiC. A

further increase in the LPE is accompanied by a strong reduction in the electric field, which is more pronounced the higher the C content in the specimen. The incomplete LPE variation for TiC allows the analysis of the electric field starting from 30 pJ, where it agrees very well with the other observed values. When the LPE is increased, the field decreases significantly compared to the other specimens down to 34.1 V/nm (200 pJ) and thus TiC exhibits the highest dependence on the LPE. The trend of more pronounced electric field reduction with increasing C content can be attributed to two factors: I) The required electric field of TiC is lower than that of TiN in order to achieve a stable evaporation behavior. II) The electric field is severely temperature dependent and decreases with increasing apex temperature. Since the energy input is constant at the same LPE, this can only be attributed to thermal conductivity properties. In fact, the Ti(C,N) specimens investigated within this work show a reduction in thermal conductivity with increasing C content from 45 ± 5 W/mK (TiN) to 32 ± 3 W/mK (TiC), as reported by Kainz *et al.* [72]. This may also explain the absence of shadow effects in the spatially resolved distribution of the electric field in specimens with a higher C content, since the entire surface is subjected to an increase in temperature and thus revealing a uniform electric field reduction.

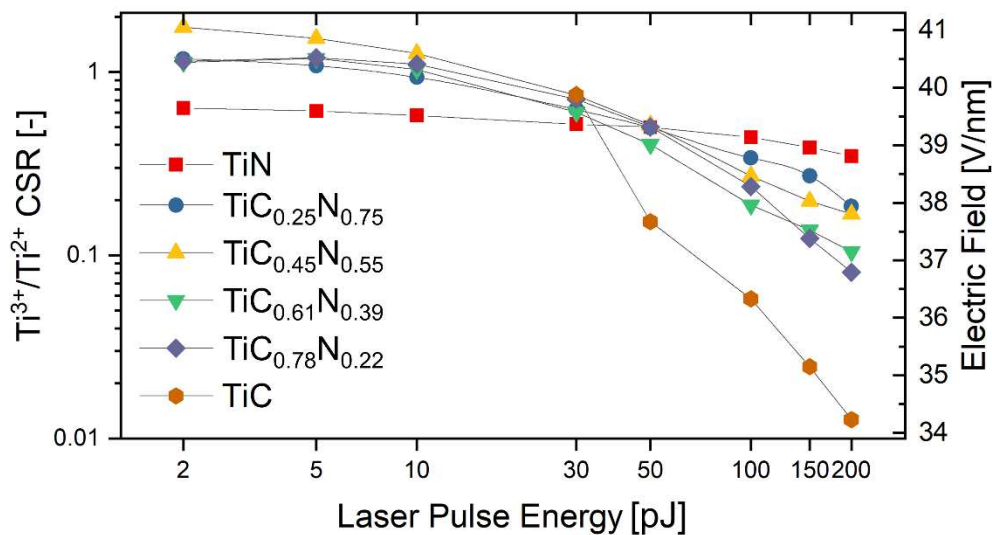


Fig. 46: Observed Ti^{3+}/Ti^{2+} CSRs and corresponding estimated electric field strengths of the investigated Ti(C,N) specimens as a function of the applied LPE.

5. Conclusions

Within the scope of this work, comprehensive atom probe tomography investigations were carried out using a series of specimens within the Ti(C,N) coating system to gain a better understanding about the evaporation behavior of nitrides and carbides in the atom probe and thus to improve elemental analysis in a sustainable manner for future investigations. Insights into the various compositional biases that occur were illuminated by laser pulse energy variations, allowing the influence of the electric field to be studied directly. In addition to the standard parameters, modern atom probe instruments also offer advanced acquisition parameters, which are based on more profound target values. Using TiN, these were studied in detail and showed promising results, therefore it is strongly recommended to establish these advanced acquisition parameters in daily operation. With sufficient prior knowledge of the material, their use offers numerous advantages and possibilities: More efficient measurements (auto pulse rate control), moderate stress on the specimen at the beginning of the measurement, accompanied by higher survivability (constant field control) and the targeted setting of electric field strengths (auto pulse energy control). Several compositional biases could be observed. Their influence on the elemental composition depends on both, the C/(C+N) content and the laser pulse energy applied. The existence ranges of the different compositional biases are illustrated in Fig. 47. At low laser pulse energies, preferential retention of C and N predominates, as these have a higher evaporation field than Ti. In addition, out-of-synch events lead to a higher background level, which is also due to the high standing voltage near the evaporation limit. As studied in detail on TiC, carbides tend to evaporate in the form of adjacent groups or as large molecules (e.g. C₇). This effect is more pronounced, the higher the C content and the higher the laser pulse energy. The latter is probably mainly due to the insufficient electric field strength, as C is the higher field component in TiC(N). At very high laser pulse energy, dissociation effects occur. This is manifested on the one hand, by the occurrence of complex molecular ions and on the other hand, by the decreasing proportion of multiple detection events, as the fragments of a dissociated molecule are more often detected as a single detection event. This is due to less likely re-ionization of neutrals caused by the severely reduced electric field and also due to the information loss in the form of detector pile-ups, since the daughter ions often show hardly temporal or spatial differences. The dissociation processes become more pronounced with increasing C content and are already observed at lower laser pulse energies, which is mainly due to the above mentioned large metastable C-containing molecules which dissociate in flight.

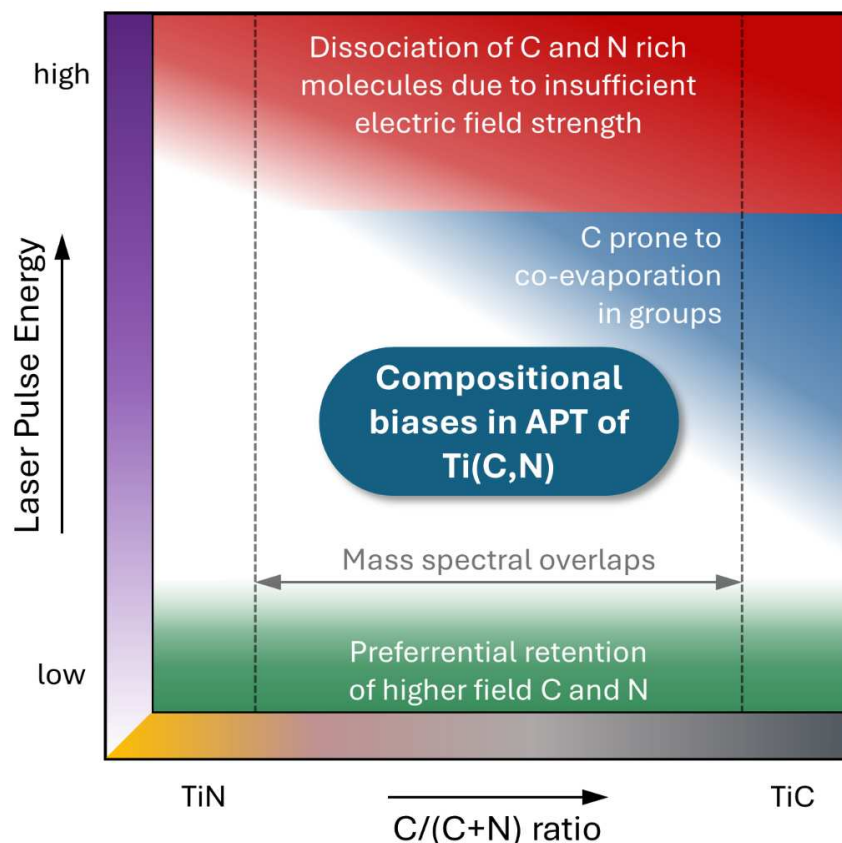


Fig. 47: Summary of observed compositional biases and their trends across the $Ti(C,N)$ coating system.

Spatially resolved analyses of the electric field showed for the specimens with a low $C/(C+N)$ ratio that shadow effects occur on the apex at higher laser pulse energies due to the laser incidence. These lead to an asymmetrical distribution of the electric field, which in turn results in poorer evaporation conditions on the shadow site. The reason for the absence of shadow effects in the specimens with a high C content could be reconciled with the decreasing thermal conductivity. The inhomogeneities in the electric field also provided insights into crystallography and grain boundaries. Based on these findings, it can be concluded that the electric field strength is the key metric to minimize compositional biases and thus achieve high elemental accuracy. If the atom probe is operated at a constant detection rate, the electric field can be controlled directly via the laser pulse energy.

The emerging technological possibilities in data evaluation, for example by machine learning-based algorithms, could significantly simplify complex analyses of compositional biases in APT in the near future. This could involve the automatic detection of ion pile-ups, statistical corrections thereof or the automatic identification of dissociation phenomena, including the adjustment of acquisition parameters to minimize them.

6. References

- [1] D. Blavette, A. Bostel, J.M. Sarrau, B. Deconihout, A. Menand, An atom probe for three-dimensional tomography, *Nature* 363 (1993) 432–435. <https://doi.org/10.1038/363432a0>.
- [2] B. Gault, M.P. Moody, J.M. Cairney, S.P. Ringer, *Atom Probe Microscopy*, Springer New York, New York, NY, 2012. <https://doi.org/10.1007/978-1-4614-3436-8>.
- [3] B. Gault, F. Vurpillot, A. Vella, M. Gilbert, A. Menand, D. Blavette, B. Deconihout, Design of a femtosecond laser assisted tomographic atom probe, *Review of Scientific Instruments* 77 (2006). <https://doi.org/10.1063/1.2194089>.
- [4] M. Hans, J.M. Schneider, On the chemical composition of TiAlN thin films - Comparison of ion beam analysis and laser-assisted atom probe tomography with varying laser pulse energy, *Thin Solid Films* 688 (2019) 137251. <https://doi.org/10.1016/j.tsf.2019.04.026>.
- [5] A. Devaraj, D.E. Perea, J. Liu, L.M. Gordon, T.J. Prosa, P. Parikh, D.R. Diercks, S. Meher, R.P. Kolli, Y.S. Meng, S. Thevuthasan, Three-dimensional nanoscale characterisation of materials by atom probe tomography, *International Materials Reviews* 63 (2018) 68–101. <https://doi.org/10.1080/09506608.2016.1270728>.
- [6] H.S. Kitaguchi, S. Lozano-Perez, M.P. Moody, Quantitative analysis of carbon in cementite using pulsed laser atom probe, *Ultramicroscopy* 147 (2014) 51–60. <https://doi.org/10.1016/j.ultramic.2014.06.004>.
- [7] T.L. Martin, A.J. London, B. Jenkins, S.E. Hopkin, J.O. Douglas, P.D. Styman, P.A.J. Bagot, M.P. Moody, Comparing the Consistency of Atom Probe Tomography Measurements of Small-Scale Segregation and Clustering between the LEAP 3000 and LEAP 5000 Instruments, *Microscopy and Microanalysis* 23 (2017) 227–237. <https://doi.org/10.1017/S1431927617000356>.
- [8] M. Tkadletz, N. Schalk, R. Daniel, J. Keckes, C. Czettl, C. Mitterer, Advanced characterization methods for wear resistant hard coatings: A review on recent progress, *Surf Coat Technol* 285 (2016) 31–46. <https://doi.org/10.1016/j.surfcoat.2015.11.016>.
- [9] Richard.J.H. Morris, R. Cuduvally, D. Melkonyan, C. Fleischmann, M. Zhao, L. Arnoldi, P. van der Heide, W. Vandervorst, Toward accurate composition analysis of GaN and AlGaN using atom probe tomography, *Journal of Vacuum Science & Technology B, Nanotechnology and Microelectronics: Materials, Processing, Measurement, and Phenomena* 36 (2018). <https://doi.org/10.1116/1.5019693>.
- [10] R. Cuduvally, R.J.H. Morris, P. Ferrari, J. Bogdanowicz, C. Fleischmann, D. Melkonyan, W. Vandervorst, Potential sources of compositional inaccuracy in the atom probe tomography of In_xGa_{1-x}As, *Ultramicroscopy* 210 (2020) 112918. <https://doi.org/10.1016/j.ultramic.2019.112918>.

- [11] H. Waldl, M. Hans, M. Schiester, D. Primetzhofer, M. Burtscher, N. Schalk, M. Tkadletz, Decomposition of CrN induced by laser-assisted atom probe tomography, *Ultramicroscopy* 246 (2023). <https://doi.org/10.1016/j.ultramic.2022.113673>.
- [12] M. Hans, M. Tkadletz, D. Primetzhofer, H. Waldl, M. Schiester, M. Bartosik, C. Czettel, N. Schalk, C. Mitterer, J.M. Schneider, Is it meaningful to quantify vacancy concentrations of nanolamellar (Ti,Al)N thin films based on laser-assisted atom probe data?, *Surf Coat Technol* 473 (2023). <https://doi.org/10.1016/j.surfcoat.2023.130020>.
- [13] E. Di Russo, I. Blum, J. Houard, M. Gilbert, G. Da Costa, D. Blavette, L. Rigutti, Compositional accuracy of atom probe tomography measurements in GaN: Impact of experimental parameters and multiple evaporation events, *Ultramicroscopy* 187 (2018) 126–134. <https://doi.org/10.1016/j.ultramic.2018.02.001>.
- [14] M. Thuvander, G. Östberg, M. Ahlgren, L.K.L. Falk, Atom probe tomography of a Ti-Si-Al-C-N coating grown on a cemented carbide substrate, *Ultramicroscopy* 159 (2015) 308–313. <https://doi.org/10.1016/j.ultramic.2015.04.008>.
- [15] M. Thuvander, D. Shinde, A. Rehan, S. Ejnermark, K. Stiller, Improving Compositional Accuracy in APT Analysis of Carbides Using a Decreased Detection Efficiency, *Microscopy and Microanalysis* 25 (2019) 454–461. <https://doi.org/10.1017/S1431927619000424>.
- [16] M. Thuvander, A. Kvist, L.J.S. Johnson, J. Weidow, H.O. Andréén, Reduction of multiple hits in atom probe tomography, *Ultramicroscopy* 132 (2013) 81–85. <https://doi.org/10.1016/j.ultramic.2012.12.005>.
- [17] E.A. Marquis, N.A. Yahya, D.J. Larson, M.K. Miller, R.I. Todd, Probing the improbable: Imaging C atoms in alumina, *Materials Today* 13 (2010) 34–36. [https://doi.org/10.1016/S1369-7021\(10\)70184-X](https://doi.org/10.1016/S1369-7021(10)70184-X).
- [18] M. Hans, J.M. Schneider, Electric field strength-dependent accuracy of TiAlN thin film composition measurements by laser-assisted atom probe tomography, *New J Phys* 22 (2020). <https://doi.org/10.1088/1367-2630/ab7770>.
- [19] F. Tang, B. Gault, S.P. Ringer, J.M. Cairney, Optimization of pulsed laser atom probe (PLAP) for the analysis of nanocomposite Ti-Si-N films, *Ultramicroscopy* 110 (2010) 836–843. <https://doi.org/10.1016/j.ultramic.2010.03.003>.
- [20] D. Santhanagopalan, D.K. Schreiber, D.E. Perea, R.L. Martens, Y. Janssen, P. Khalifah, Y.S. Meng, Effects of laser energy and wavelength on the analysis of LiFePO₄ using laser assisted atom probe tomography, *Ultramicroscopy* 148 (2015) 57–66. <https://doi.org/10.1016/j.ultramic.2014.09.004>.
- [21] E. Di Russo, I. Blum, J. Houard, G. Da Costa, D. Blavette, L. Rigutti, Field-Dependent Measurement of GaAs Composition by Atom Probe Tomography, *Microscopy and Microanalysis* 23 (2017) 1067–1075. <https://doi.org/10.1017/S1431927617012582>.

- [22] G. Sha, A. Cerezo, G.D.W. Smith, Field evaporation behavior during irradiation with picosecond laser pulses, *Appl Phys Lett* 92 (2008) 2006–2009. <https://doi.org/10.1063/1.2837626>.
- [23] B. Gault, D.W. Saxey, M.W. Ashton, S.B. Sinnott, A.N. Chiamonti, M.P. Moody, D.K. Schreiber, Behavior of molecules and molecular ions near a field emitter, *New J Phys* 18 (2016). <https://doi.org/10.1088/1367-2630/18/3/033031>.
- [24] M. Schiester, H. Waldl, M. Hans, M. Thuvander, D. Primetzhofer, N. Schalk, M. Tkadletz, Influence of multiple detection events on compositional accuracy of TiN coatings in atom probe tomography, *Surf Coat Technol* 477 (2024) 130318. <https://doi.org/10.1016/j.surfcoat.2023.130318>.
- [25] M. Thuvander, J. J. Weidow, J. Angseryd, L.K.L. Falk, F. Liu, M. Sonestedt, K. Stiller, H.O. Andrén, Quantitative atom probe analysis of carbides, *Ultramicroscopy* 111 (2011) 604–608. <https://doi.org/10.1016/j.ultramic.2010.12.024>.
- [26] J. Angseryd, F. Liu, H.O. Andrén, S.S.A. Gerstl, M. Thuvander, Quantitative APT analysis of Ti(C,N), *Ultramicroscopy* 111 (2011) 609–614. <https://doi.org/10.1016/j.ultramic.2011.01.031>.
- [27] F. Liu, H.O. Andrén, Effects of laser pulsing on analysis of steels by atom probe tomography, *Ultramicroscopy* 111 (2011) 633–641. <https://doi.org/10.1016/j.ultramic.2010.12.012>.
- [28] E. Di Russo, I. Blum, I. Rivalta, J. Houard, G. Da Costa, F. Vurpillot, D. Blavette, L. Rigutti, Detecting Dissociation Dynamics of Phosphorus Molecular Ions by Atom Probe Tomography, *Journal of Physical Chemistry A* 124 (2020) 10977–10988. <https://doi.org/10.1021/acs.jpca.0c09259>.
- [29] Z. Peng, D. Zanuttini, B. Gervais, E. Jacquet, I. Blum, P.P. Choi, D. Raabe, F. Vurpillot, B. Gault, Unraveling the Metastability of C_n^{2+} ($n = 2-4$) Clusters, *Journal of Physical Chemistry Letters* 10 (2019) 581–588. <https://doi.org/10.1021/acs.jpcllett.8b03449>.
- [30] Z. Peng, F. Vurpillot, P.P. Choi, Y. Li, D. Raabe, B. Gault, On the detection of multiple events in atom probe tomography, *Ultramicroscopy* 189 (2018) 54–60. <https://doi.org/10.1016/j.ultramic.2018.03.018>.
- [31] R.J.H. Morris, R. Cuduvally, J.R. Lin, M. Zhao, W. Vandervorst, M. Thuvander, C. Fleischmann, Field dependent study on the impact of co-evaporated multihits and ion pile-up for the apparent stoichiometric quantification of GaN and AlN, *Ultramicroscopy* 241 (2022) 113592. <https://doi.org/10.1016/j.ultramic.2022.113592>.
- [32] D. Zanuttini, I. Blum, L. Rigutti, F. Vurpillot, J. Douady, E. Jacquet, P.M. Anglade, B. Gervais, Simulation of field-induced molecular dissociation in atom-probe tomography: Identification of a neutral emission channel, *Phys Rev A (Coll Park)* 95 (2017) 1–6. <https://doi.org/10.1103/PhysRevA.95.061401>.
- [33] D.J. Larson, T.J. Prosa, R.M. Ulfing, B.P. Geiser, T.F. Kelly, *Local Electrode Atom Probe Tomography*, 3rd ed., 2013.

- [34] M.K. Miller, R.G. Forbes, Atom probe tomography, *Mater Charact* 60 (2009) 461–469. <https://doi.org/10.1016/j.matchar.2009.02.007>.
- [35] M.K. Miller, R.G. Forbes, *Atom-Probe Tomography*, Springer US, Boston, MA, 2014. <https://doi.org/10.1007/978-1-4899-7430-3>.
- [36] W.P. Poschenrieder, MULTIPLE-FOCUSING TIME OF FLIGHT MASS SPECTROMETERS* PART I. TOFMS WITH EQUAL MOMENTUM ACCELERATION*, n.d.
- [37] W.P. Poschenrieder, *International Journal. of Mass Spectrometry-and Ion Physics* MULTIPLE-FOCUSING TIME-OF-FLIGHT MASS SPECTROMETERS PART II. TOFMS WITH EQUAL ENERGY ACCELERATION, n.d.
- [38] D.J. Griffiths, *Introduction to Electrodynamics*, Cambridge University Press, 2017. <https://doi.org/10.1017/9781108333511>.
- [39] R.P. Feynman, R.B. Leighton, M. Sands, S.B. Treiman, *The Feynman Lectures on Physics*, *Phys Today* 17 (1964) 45–46. <https://doi.org/10.1063/1.3051743>.
- [40] J.R. Oppenheimer, Three Notes on the Quantum Theory of Aperiodic Effects, *Physical Review* 31 (1928) 66–81. <https://doi.org/10.1103/PhysRev.31.66>.
- [41] R.H. Fowler, L. Nordheim, Electron emission in intense electric fields, *Proceedings of the Royal Society of London. Series A, Containing Papers of a Mathematical and Physical Character* 119 (1928) 173–181. <https://doi.org/10.1098/rspa.1928.0091>.
- [42] E.W. Müller, Die Abhängigkeit der Feldelektronenemission von der Austrittsarbeit, *Zeitschrift Für Physik* 102 (1936) 734–761. <https://doi.org/10.1007/BF01338540>.
- [43] E.W. Müller, Field Desorption, *Physical Review* 102 (1956) 618–624. <https://doi.org/10.1103/PhysRev.102.618>.
- [44] J.A. Panitz, My Life with Erwin: The Beginning of an Atom-Probe Legacy, *Microscopy and Microanalysis* 25 (2019) 274–279. <https://doi.org/10.1017/S1431927618015313>.
- [45] E.W. Müller, J.A. Panitz, S.B. McLane, The atom-probe field ion microscope, *Review of Scientific Instruments* 39 (1968) 83–86. <https://doi.org/10.1063/1.1683116>.
- [46] R. Gomer, Field emission, field ionization, and field desorption, *Surf Sci* 299–300 (1994) 129–152. [https://doi.org/10.1016/0039-6028\(94\)90651-3](https://doi.org/10.1016/0039-6028(94)90651-3).
- [47] C.G. Sánchez, A.Y. Lozovoi, A. Alavi, Field-evaporation from first-principles, *Mol Phys* 102 (2004) 1045–1055. <https://doi.org/10.1080/00268970410001727673>.
- [48] K. Hono, S.S. Babu, *Atom-Probe Field Ion Microscopy*, in: *Physical Metallurgy: Fifth Edition*, Elsevier Inc., 2014: pp. 1453–1589. <https://doi.org/10.1016/B978-0-444-53770-6.00015-0>.
- [49] R. Gomer, Field desorption, *J Chem Phys* 31 (1959) 341–345. <https://doi.org/10.1063/1.1730354>.

- [50] L. Rousseau, A. Normand, F.F. Morgado, H.S. Marie Scisly Søreide, L.T. Stephenson, C. Hatzoglou, G. Da Costa, K. Tehrani, C. Freysoldt, B. Gault, F. Vurpillot, Introducing field evaporation energy loss spectroscopy, *Commun Phys* 6 (2023). <https://doi.org/10.1038/s42005-023-01203-2>.
- [51] G.L. Kellogg, T.T. Tsong, Pulsed-laser atom-probe field-ion microscopy, *J Appl Phys* 51 (1980) 1184–1193. <https://doi.org/10.1063/1.327686>.
- [52] D.G. Brandon, The structure of field-evaporated surfaces, *Surf Sci* 3 (1965) 1–18. [https://doi.org/10.1016/0039-6028\(65\)90014-2](https://doi.org/10.1016/0039-6028(65)90014-2).
- [53] R. Haydock, D.R. Kingham, Post-ionization of Field-Evaporated Ions, *Phys Rev Lett* 44 (1980) 1520–1523. <https://doi.org/10.1103/PhysRevLett.44.1520>.
- [54] R. Haydock, D.R. Kingham, Some predictions of a theory of post-ionization of field-evaporated ions, *Surface Science Letters* 104 (1981) L194–L198. [https://doi.org/10.1016/0167-2584\(81\)90176-6](https://doi.org/10.1016/0167-2584(81)90176-6).
- [55] D.R. Kingham, The post-ionization of field evaporated ions: A theoretical explanation of multiple charge states, *Surf Sci* 116 (1982) 273–301. [https://doi.org/10.1016/0039-6028\(82\)90434-4](https://doi.org/10.1016/0039-6028(82)90434-4).
- [56] E. Oltman, R. Ulfig, D. Larson, Background Removal Methods Applied to Atom Probe Data, *Microscopy and Microanalysis* 15 (2009) 256–257. <https://doi.org/10.1017/S1431927609095488>.
- [57] D.J. Larson, B. Gault, B.P. Geiser, F. De Geuser, F. Vurpillot, Atom probe tomography spatial reconstruction: Status and directions, *Curr Opin Solid State Mater Sci* 17 (2013) 236–247. <https://doi.org/10.1016/j.cossms.2013.09.002>.
- [58] D. Haley, P. Choi, D. Raabe, Guided mass spectrum labelling in atom probe tomography, *Ultramicroscopy* 159 (2015) 338–345. <https://doi.org/10.1016/j.ultramic.2015.03.005>.
- [59] T.F. Kelly, Kinetic-energy discrimination for atom probe tomography, *Microscopy and Microanalysis* 17 (2011) 1–14. <https://doi.org/10.1017/S1431927610094468>.
- [60] N.E. Holden, T.B. Coplen, J.K. Böhlke, L. V. Tarbox, J. Benefield, J.R. De Laeter, P.G. Mahaffy, G. O'Connor, E. Roth, D.H. Tepper, T. Walczyk, M.E. Wieser, S. Yoneda, IUPAC Periodic Table of the Elements and Isotopes (IPTEI) for the Education Community (IUPAC Technical Report), *Pure and Applied Chemistry* 90 (2018) 1833–2092. <https://doi.org/10.1515/pac-2015-0703>.
- [61] F. Meisenkothen, E.B. Steel, T.J. Prosa, K.T. Henry, R. Prakash Kolli, Effects of detector dead-time on quantitative analyses involving boron and multi-hit detection events in atom probe tomography, *Ultramicroscopy* 159 (2015) 101–111. <https://doi.org/10.1016/j.ultramic.2015.07.009>.
- [62] U. ROLANDER, H.-O. ANDRÉN, STATISTICAL CORRECTION FOR PILE-UP IN THE ATOM-PROBE DETECTOR SYSTEM, *Le Journal de Physique Colloques* 50 (1989) C8-529-C8-534. <https://doi.org/10.1051/jphyscol:1989891>.

- [63] T.T. Tsong, Formation of multiatomic cluster ions of silicon in pulsed-laser stimulated field desorption, *Appl Phys Lett* 45 (1984) 1149–1151. <https://doi.org/10.1063/1.95018>.
- [64] M. Müller, D.W. Saxey, G.D.W. Smith, B. Gault, Some aspects of the field evaporation behaviour of GaSb, *Ultramicroscopy* 111 (2011) 487–492. <https://doi.org/10.1016/j.ultramic.2010.11.019>.
- [65] D.W. Saxey, Correlated ion analysis and the interpretation of atom probe mass spectra, *Ultramicroscopy* 111 (2011) 473–479. <https://doi.org/10.1016/J.ULTRAMIC.2010.11.021>.
- [66] CAMECA Instruments Inc., LEAP 5000 Platform User Manual, 2021.
- [67] H. Holzschuh, Chemical-vapor deposition of wear resistant hard coatings in the Ti–B–C–N system: properties and metal-cutting tests, *Int J Refract Metals Hard Mater* 20 (2002) 143–149. [https://doi.org/10.1016/S0263-4368\(02\)00013-6](https://doi.org/10.1016/S0263-4368(02)00013-6).
- [68] L. von Fieandt, K. Johansson, T. Larsson, M. Boman, E. Lindahl, On the growth, orientation and hardness of chemical vapor deposited Ti(C,N), *Thin Solid Films* 645 (2018) 19–26. <https://doi.org/10.1016/j.tsf.2017.10.037>.
- [69] C. Czettel, C. Mitterer, U. Mühle, D. Rafaja, S. Puchner, H. Hutter, M. Penoy, C. Michotte, M. Kathrein, CO addition in low-pressure chemical vapour deposition of medium-temperature TiC_xN_{1-x} based hard coatings, *Surf Coat Technol* 206 (2011) 1691–1697. <https://doi.org/10.1016/j.surfcoat.2011.07.086>.
- [70] A. Larsson, S. Rupp, Microstructure and properties of Ti(C,N) coatings produced by moderate temperature chemical vapour deposition, 2002.
- [71] C. Czettel, C. Mitterer, M. Penoy, C. Michotte, M. Kathrein, C₂H₆ as precursor for low pressure chemical vapor deposition of TiCN hard coatings, *Surf Coat Technol* 215 (2013) 127–132. <https://doi.org/10.1016/j.surfcoat.2012.08.081>.
- [72] C. Kainz, N. Schalk, M. Tkadletz, M. Winkler, C. Czettel, Microstructure, mechanical and thermo-physical properties of CVD TiC_xN_{1-x} coatings on cemented carbide substrates grown with C₂H₆ as C feeding precursor, *Surf Coat Technol* 394 (2020). <https://doi.org/10.1016/j.surfcoat.2020.125868>.
- [73] C. Kainz, N. Schalk, C. Saringer, C. Czettel, In-situ investigation of the oxidation behavior of powdered TiN, Ti(C,N) and TiC coatings grown by chemical vapor deposition, *Surf Coat Technol* 406 (2021). <https://doi.org/10.1016/j.surfcoat.2020.126633>.
- [74] P. Ström, D. Primetzhofer, Ion beam tools for nondestructive in-situ and in-operando composition analysis and modification of materials at the Tandem Laboratory in Uppsala, *Journal of Instrumentation* 17 (2022). <https://doi.org/10.1088/1748-0221/17/04/P04011>.
- [75] M. V. Moro, R. Holeňák, L. Zendejas Medina, U. Jansson, D. Primetzhofer, Accurate high-resolution depth profiling of magnetron sputtered transition metal alloy films containing light species: A multi-method approach, *Thin Solid Films* 686 (2019). <https://doi.org/10.1016/j.tsf.2019.137416>.

- [76] M. Tkadletz, H. Waldl, M. Schiester, A. Lechner, G. Schusser, M. Krause, N. Schalk, Efficient preparation of microtip arrays for atom probe tomography using fs-laser processing, *Ultramicroscopy* 246 (2023). <https://doi.org/10.1016/j.ultramic.2022.113672>.
- [77] M.K. Miller, K.F. Russell, Atom probe specimen preparation with a dual beam SEM/FIB miller, *Ultramicroscopy* 107 (2007) 761–766. <https://doi.org/10.1016/j.ultramic.2007.02.023>.
- [78] Ankit Rohatgi, WebPlotDigitizer, (2022). <https://automeris.io/WebPlotDigitizer> (accessed February 5, 2022).
- [79] I. El Azhari, J. Barrirero, N. Valle, J. García, L. von Fieandt, M. Engstler, F. Soldera, L. Llanes, F. Mücklich, Impact of temperature on chlorine contamination and segregation for Ti(C,N) CVD thin hard coating studied by nano-SIMS and atom probe tomography, *Scr Mater* 208 (2022) 114321. <https://doi.org/10.1016/j.scriptamat.2021.114321>.
- [80] H. Zschiesche, A. Charai, C. Alfonso, D. Mangelinck, Methods for Gibbs triple junction excess determination: Ti segregation in CoSi₂ thin film, *J Mater Sci* 55 (2020) 13177–13192. <https://doi.org/10.1007/s10853-020-04856-4>.

7. Appendix

Table 7: Overview of all ion species ranged within this work including the observed charge states and m/n ratios. Note: Each mass spectrum was individually ranged, the lower and upper limits of all peaks were adjusted according to symmetrical ranging.

Ion species	Charge state	m/n [Da]
<i>Elemental ions</i>		
	+++	15.33 - 15.67 - 16 - 16.33 - 16.67
Ti	++	23 - 23.5 - 24 - 24.5 - 25
	+	46 - 47 - 48 - 49 - 50
C	++	6 - 6.5
	+	12 - 13
N	++	7 - 7.5
	+	14 - 15
Cl	++	17.5 - 18.5
	+	35 - 37
Co	++	29,5
Ga	++	34,5
	+	69
<i>Titanium-rich molecular ions</i>		
TiC	++	29 - 29.5 - 30 - 30.5 - 31
	+	59 - 60 - 61
TiN	++	30 - 30.5 - 31 - 31.5 - 32
	+	60 - 61 - 62 - 63 - 64
Ti ₂ N	+++	36 - 36.33 - 36.67 - 37 - 37.33
TiH	+++	17
	++	25.5
TiO	++	31 - 31.5 - 32 - 32.5 - 33
	+	62 - 63 - 64 - 65 - 66
TiON	+++	26
TiCl	++	41.5

Carbon-rich molecular ions

C_2N	++	19 - 19.5
	+	38 - 39
C_2N_2	+	52 - 53
C_3	++	18 - 18.5
	+	36 - 37
C_5	+	60 - 61
C_7	+	84
C_3N	+	50 - 51
CCl	+	47 - 49
CN	+	26 - 27

Nitrogen-rich molecular ions

N_2	+	28 - 29
N_3H	+++	14.33
N_2C	+	40
